MAX PLANCK INSTITUTE FOR POLYMER RESEARCH

Photophysical Investigation of Organic Chromophores for Optoelectronic Applications

DISSERTATION

Zur Erlangung des Grades

„Doktor der Naturwissenschaften“ im Promotionsfach Chemie

am Fachbereich Chemie, Pharmazie und Geowissenschaften

der Johannes Gutenberg-Universität

in Mainz

Kalyani Thakur

geboren in New Delhi, India

Mainz, 2023

1 Gutachter: Prof. Dr. Paul W. M. Blom

2 Gutachter: Prof. Dr. Thomas Basché

Tag der mundliche Prüfung :

I hereby declare that I wrote the dissertation submitted without any unauthorized external assistance and used only sources acknowledged in the work. All textual passages, which are appropriated verbatim or paraphrased from published and unpublished texts, as well as all information obtained from oral sources, are duly indicated and listed in accordance with bibliographical rules. In carrying out this research, I complied with the rules of standard scientific practice as formulated in the statutes of Johannes Gutenberg-University Mainz to insure standard scientific practice.

Kalyani

Table of Contents

Scope and Motivation

Organic chromophores have gained significant popularity in the scientific community due to their immense potential as alternative materials for organic optoelectronic devices. These devices include organic field effect transistors (OFETs), organic light-emitting diodes (OLEDs), organic photovoltaics (OPVs), sensors, and biohybrid electronics. With their unique optical and electronic properties, organic chromophores fall in the category of organic semiconductors. These organic semiconductor-based devices offer remarkable advantages such as flexibility, transparency, robustness, and low power consumption, distinguishing them from conventional inorganic electronics. To fully explore the potential of newly synthesized organic chromophores, it is crucial to comprehensively characterize their photophysical properties. The photophysics of chromophores plays a pivotal role in determining their suitability for various optoelectronic applications. In this thesis, the focus is on studying the energy and electron transfer mechanisms in covalently linked organic chromophores, which comprise electron donor (molecules or entity capable of transferring energy or electrons) and acceptor (molecules or entity capable of accepting energy or electrons) dyads, triads, and supramolecular structures. The objective is to explore their potential applications in optoelectronic devices, especially OLEDs, OPVs and biohybrid devices.

Chapter 1 focuses on the theoretical background essential for understanding the basic concepts in organic chromophore photophysics. First, I will present a general introduction of organic chromophores, discussing their electronic and optical properties. It is followed by the general principle of radiative and non-radiative processes, focusing on energy and electron transfer in organic chromophores.

Chapter 2 describes the techniques used to characterize the energy and electron transfer processes, namely transient absorption and time-resolved photoluminescence spectroscopy. The first half of the chapter discusses the basic principles of ultrafast spectroscopy, followed by the experimental set-up and theoretical explanation of ultrafast techniques.

Chapter 3 focuses on the characterization of photophysical properties of a conformationally flexible acceptor-donor-acceptor triad molecular system. An electron-donating diethyl aniline unit is covalently linked between two electron-accepting perylene diimide (PDI)

chromophores which can adopt *open* (two PDI apart) *and folded* (two PDI within π-stacking distance) configurations in various solvents. We investigate solvent-dependent changes in photophysical properties of the *open* and *folded* conformation. The *open* form undergoes photoinduced electron transfer based on solvent polarity, while the *folded* form undergoes a symmetry breaking charge transfer mechanism.

Chapter 4 explores the photophysical characterization of thermally activated delayed fluorescence (TADF) based organic chromophores. This study demonstrates for the first time that the decay of photoluminescence in TADF materials is significantly influenced by the initial density of photoexcited populations due to annihilation processes. To explore this phenomenon, a model TADF system called CzDBA is employed, consisting of a carbazole donor attached to a diboron anthracene acceptor. Upon excitation, singlet excitons are generated, which undergo intersystem crossing (ISC) to form triplet excitons. These triplet excitons are subsequently converted back to singlet excitons through reverse intersystem crossing (rISC), leading to delayed fluorescence emission. This unique process holds immense potential for organic light-emitting diodes (OLEDs) based on TADF materials, as it offers the prospect of achieving 100% internal quantum efficiency. Within this chapter, the experimentally obtained transient kinetic curves of CzDBA are subjected to modeling using a kinetic decay model. This modeling approach enables the extraction of vital photophysical parameters such as ISC/rISC rates, as well as exciton annihilation rates. Importantly, unlike the conventional bi-exponential approach, this methodology can be universally applied to all TADF materials, offering a more reliable and accurate means of characterizing their photophysical rate constants.

Chapter 5 addresses the challenge of obtaining solution processable TADF materials. TADF materials generally consist of small molecules that are less soluble in most organic solvents, making them unsuitable for solution processing and device fabrication. To make TADF materials more amenable to solution processing, the chemical structure is modified by the addition of tert-butyl groups. This not only makes the material more soluble in organic solvents but also improves the photophysical properties such as reverse intersystem crossing rate and reduces the non-radiative decay rate of the material. This chapter discusses the influence of tert-butylation on the photophysics of TADF materials.

Chapter 6 demonstrates the example of a flexible biohybrid-based photoelectrode based on a photosynthetic protein. A nanostructured photoelectrode is fabricated using silver nanowires on a flexible transparent plastic substrate, which is used to bind the reaction center light-harvesting complex (RCLH1) to its surface. This biohybrid photoelectrode is used as a photocathode in a photoelectrochemical cell. External electron donor and acceptor molecules called ubiquinone and cytochrome C are used in the electrolyte solution. Upon photoexcitation, the RCLH1 protein becomes redox-active, triggers a series of electron transfer reactions and finally reduces the ubiquinone. While the electron vacancy generated in the RCLH1 is refilled by cytochrome C and completes the electron cycle to generate the current, peak photocurrents of 177µA/cm^2 are observed, demonstrating the successful fabrication of the biohybrid device using a flexible electrode.

Finally, the general conclusion of all the works is summarized, and an outlook and future scope is given.

Chapter 1 : Theoretical Background

This chapter focuses on the theoretical foundation relevant to this thesis, particularly on the electronic and optical properties of organic chromophores and the mechanisms of energy and charge transfer.

1.1 Organic chromophore

An organic chromophore is a part or moiety of an organic molecule responsible for imparting its color. Chromophores primarily consist of carbon and hydrogen atoms and always have π-conjugation, i.e., their chemical structure possesses alternating double and single carbon bonds. The π-conjugation creates an energy gap within the molecules that leads to their semiconducting properties and since chromophores are organic molecules, they are also classified as organic semiconductors. The energy gap plays a crucial role in determining the optical and electrical properties of the molecules [1]. When an organic chromophore is exposed to light with an energy equivalent to its optical energy gap, the light will be absorbed, and an electron will be promoted from the ground state to the excited state. The ground and the first excited state hold special names in organic chromophores; they are generally referred to as the highest occupied molecular orbital (HOMO) and lowest unoccupied molecular orbital (LUMO) respectively [2].

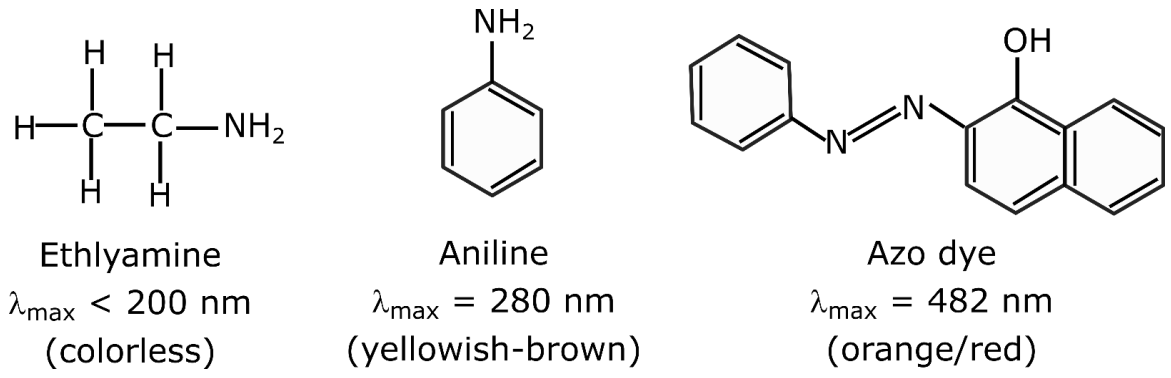

Figure 1.1: Chemical structure of Ethylamine, Aniline and Azo dye. The Ethylamine does not consist of alternating single-double bonds and is colorless. Aniline and Azo dye possessing conjugation absorb in the UV/visible region and are classified as organic chromophores.

As the highest orbital filled with electrons ends at HOMO, and the lowest unfilled orbital starts at LUMO, the HOMO and LUMO are also referred to as frontier orbitals. The HOMO-LUMO gap represents the energy of transition during either excitation or relaxation of an electron,

which mostly lies in the ultraviolet (UV) to the visible region. Let's consider an example, namely the following three molecules: ethylamine, aniline and azo-dye, as shown in Figure 1.1. Both aniline and azo-dye absorb in either the UV or visible region, while ethylamine is colorless [3]. Aniline and azo-dye are classified as chromophores, while ethylamine, despite having the same functional group as aniline, is not a chromophore since it does not emit in the visible region.

1.1.1 Electronic structure

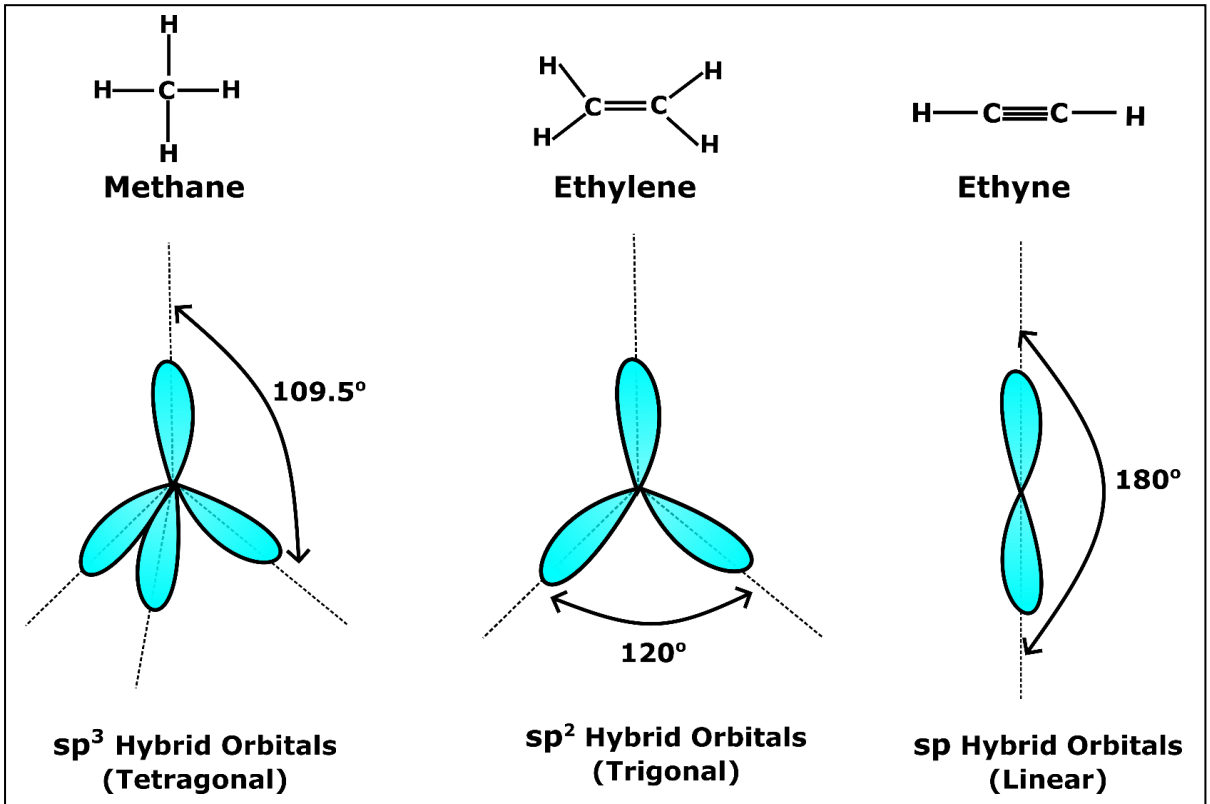

Figure 1.2: Example of sp^3, sp^2 and sp hybridization in methane, ethylene and ethyne. The carbon atoms in methane have sp^3 hybridization with tetragonal geometry, ethylene has sp^2 hybridization with trigonal geometry and ethyne has sp hybridization in a linear geometry.

Organic semiconductors are primarily carbon-based compounds. The electronic configuration of the carbon atom in its ground state is written as $1s^2\ 2s^2\ 2p^2$. It has four electrons in its valence shell and needs four more electrons to achieve an inert atomic configuration. This is done by covalent bond formation, where a carbon atom forms a bond with its neighboring atom and equally shares its electron between the two bonding atoms [4]. When two carbon atoms come together to form a covalent bond, their atoms undergo the process of

hybridization. This is the intermixing of s and p orbital to form new hybrid orbitals having different energy, shape and spatial orientation than the initial orbitals. These newly formed hybrid orbitals are degenerate.

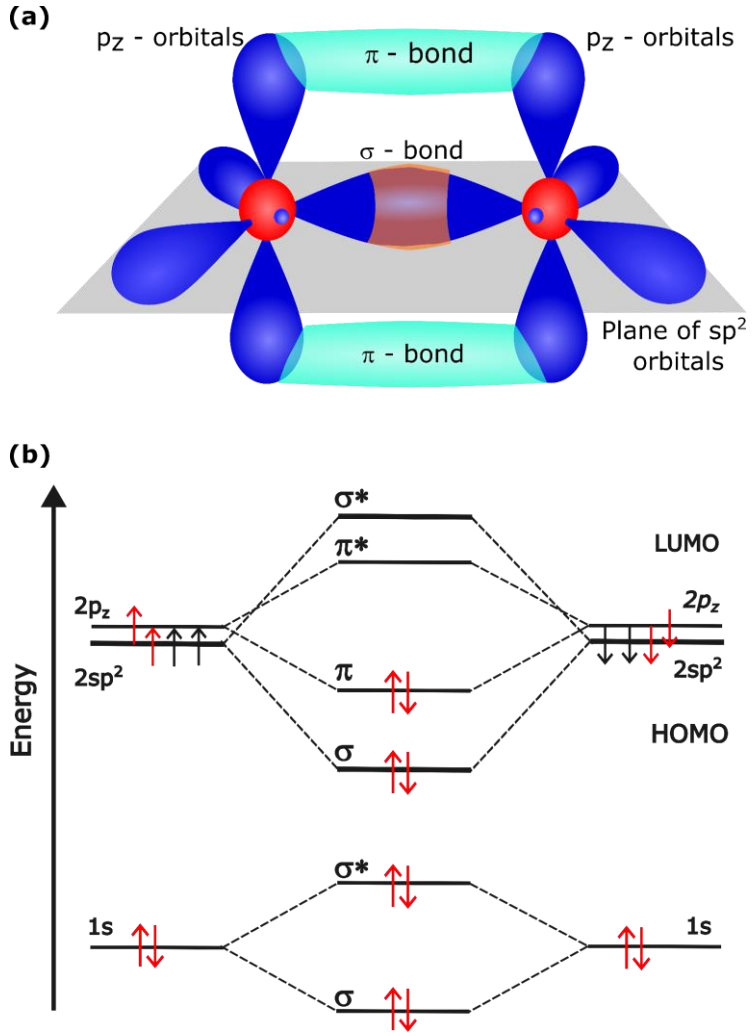

Figure 1.3: (a) Molecular orbital structure and (b) energy band diagram illustrating formation of σ-bond and π-bond from atomic orbitals in ethylene molecules. In sp^2 hybrid orbitals, the arrows in the red are for the electron participating in carbon-carbon bond formation, while the black arrow indicates the electron forming sigma bonds with other hydrogen atoms.

For example, as shown in Figure 1.2, in the simplest carbon compound methane, the carbon atom has sp^3-hybridization. One 2s and three 2p (p_x, p_y, and p_z) orbitals of methane combine to give four equivalent orbitals located at 109.5° from each other in a tetrahedron. In the case of ethylene, one 2s orbital is combined with two 2p orbitals to form three sp^2 hybrid orbitals leaving one unhybridized p_z orbital which lies orthogonal to the plane. These three sp^2 orbitals point at the corner of an equivalent trigonal in the XY-plane at a 120° angle. Finally, when one

2s orbital hybridizes only with one 2p orbital, it forms two sp-hybrid orbitals at 180° apart, leaving behind two unhybridized p orbitals, as observed in ethyne. These unhybridized orbitals can overlap with neighboring unhybridized orbitals to form the π-bond, described in the next section.

1.1.2 Molecular orbital theory

The molecular orbital theory describes the covalent bonding in the formation of molecule [5]. When two atomic orbitals of the same wave function combine in phase, they form a bonding molecular orbital, while an out-of-phase combination results in the less stable anti-bonding molecular orbital, usually denoted with a '*'. Thus, the electrons in a molecular orbital are no longer associated with individual atomic orbitals but now belong to the shared molecular orbitals. As an approximation, a molecular orbital can be described as a linear combination of their atomic orbitals. This process gives rise to splitting in energy between bonding-antibonding molecular orbitals. The energy of these newly formed orbitals depends on the energy and overlap of original orbitals, the stronger the overlap, the larger is the splitting between the orbitals.

The number of bonds a carbon atom can make is determined by the number of hybrid orbitals and the remaining unhybridized p-orbitals available. Consider the ethylene molecule, C_2H_4, as an example, which is shown in Figure 1.3. Each carbon atom has three sp^2 hybrid orbitals and one p_z (unhybridized) orbital perpendicular to the XY-plane. The three sp^2 hybrid orbitals are coplanar, located at 120° from each other, which forms so-called σ-bonds when combined with neighboring atoms. The remaining two unhybridized p_z orbitals have spatial density above and below the molecular axis. The overlap between p_z orbitals with the adjacent carbon atoms results in the formation of a π-bonding molecular orbital. The combination of a sp^2 – sp^2 σ-bond and a 2p – 2p π-bond is called a double bond. Electrons are filled in these molecular orbitals following the Pauli Exclusion Principle: not more than two electrons can occupy the same orbitals and these two electrons should have opposite spins. The electrons first fill the more stable bonding orbitals (Aufbau principle), with each orbital having two electrons of opposite spin; the remaining electrons are then filled into higher energetic anti-bonding orbitals. In the case of ethylene, four electrons in the 1s-orbital of each carbon are

occupied in σ and σ*- orbital. Similarly, the three out of four electrons of $2sp^2$ of each carbon atom form σ-bonds, two with the 1s-orbital of hydrogen and one with adjacent carbon atom to form molecules as shown by the red arrow. The remaining two electrons of p_z – orbitals are occupied in π-bonding orbitals, leaving the σ* and π* orbitals empty [5], as shown in Figure 1.3. When the number of carbon atoms having sp^2 hybridization increases in the molecules, it forms alternating double and single bonds, leading to conjugation. This means that an electron in the π-bond is not limited to a specific carbon atom but it is delocalized over the conjugated length in the molecules [6].

1.1.3 Energy of molecular states

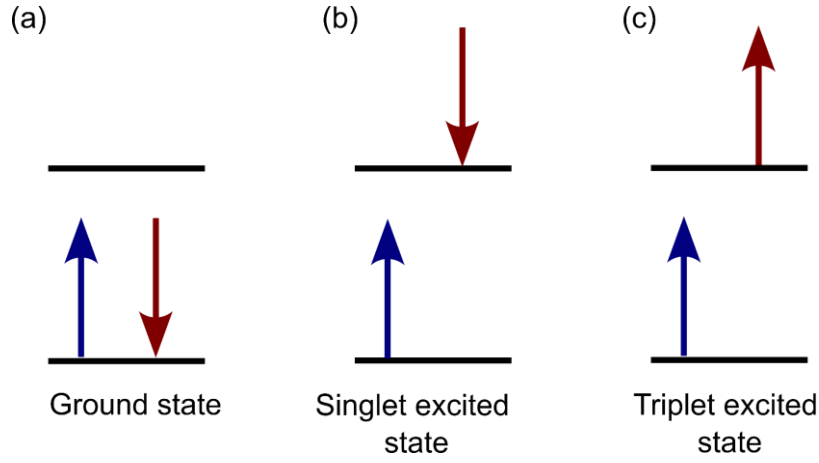

Figure 1.4: Schematic representation of a singlet and triplet state.

The energy of a molecular state is given by the superposition of the wave function of all the electrons present in a specific configuration in the orbitals and it is given by electronic wavefunction Φ_e. In the ground state of molecules electrons are filled till the HOMO orbitals, which is the most stable configuration, while an excited state is formed when an electron transitions to occupy the orbitals in the LUMO, described further in section 1.3. While calculating the energy of molecular states, the electron spin also plays a very significant role. In the case of organic chromophores, all the orbitals are occupied with electron pairs with opposite spins, and their overall spin is zero. Only the orbitals having unpaired electrons become significant to the spin contribution of the molecule. A singlet state is created when the electron in an excited state is paired with the remaining electron in the ground with the opposite spin (anti-parallel configuration). In contrast, a triplet state forms when the electron

in the excited state has the same spin as the electron in the ground state, as shown in Figure 1.4. The contribution of the spin wave function is described by Φ_S which takes account of the spin angular momentum of an electron. At the same time, nuclei of molecules are also not stationary but oscillate around their equilibrium position with a particular vibrational frequency. The vibrational wavefunction Φ_{vib} describes the vibrational motion of nuclei. The total wavefunction of a molecule is given by the product of all wavefunctions as $\Phi_{tot} = \Phi_e\Phi_S\Phi_{vib}$. [4]

1.2 Optical transitions in organic chromophores

An optical transition occurs when an electron in the ground state gains energy from the absorption of a photon and jumps to an excited state. In organic molecules, it is generally observed between the π-π* transition. However, with more complex molecules containing atoms having lone pair of electrons, a transition from n- π* is also possible [7].

Fermi's Golden Rule, derived from time-dependent perturbation theory, gives a more accurate description of the optical transition [8]. Fermi's Golden rule computes the transition rate induced between stationary states (i.e., between the ground state and excited states) caused by a small perturbation to an otherwise unperturbed system. If H is the Hamiltonian of an unperturbed system and H° is the perturbation-inducing transition of an electron from an occupied state to an unoccupied higher energy state. The probability of a transition is given by equation 1:

$$T_{i\to f} = \frac{2\pi}{\hbar}| < \Phi_i|H^{0}_{if}|\Phi_f > |^2\rho_f \qquad (1)$$

Where, Φ_i and Φ_f are the initial and final state which depends on the perturbation $H^{0,}$ and ρ is the density of the final state. Replacing the total wavefunction of molecules $\Phi_{tot} = \Phi_e\Phi_S\Phi_{vib}$, the rate of transition becomes:

$$T_{i\to f} = \frac{2\pi}{\hbar}| < \Phi_e\Phi_S\Phi_{vib_i}|H^0_{if}|\Phi_e\Phi_S\Phi_{vib_f} > |^2\rho_f \qquad (2)$$

During the electron transitions of absorption and emission, only electrons are perturbed from the incoming transition dipole operator of electromagnetic radiation. The nuclei's motion is

too slow to respond to this electromagnetic oscillation as the mass of the nucleus is almost 1000 times more than the mass of an electron. Thus, the kinetic energy of nuclei is very small compared to that of the electron and can be neglected, hence allowing the decoupling of the electron's motion from the nuclear motion. This is also known as the Born-Oppenheimer approximation.

As light is an electromagnetic wave, the interaction of electrons in an atom or molecules with the light can be described by the electric dipole operator $\mathbf{e\hat{R}}$ for light absorption or emission. Since only electrons respond to the changing electromagnetic field while spin and nuclear motion remains unaffected, the dipole operator only changes the electronic wavefunction of the molecules as given by equation 3:

$$T_{i\to f} = \frac{2\pi}{\hbar} | < \Phi_{e_i} | e\hat{R} | \Phi_{e_f} > |^2 | < \Phi_{vib_i} | \Phi_{vib_f} > |^2 | < \Phi_{s_i} | s_f > |^2 \rho_f \qquad (3)$$

If any of these integrals becomes zero, the transition will be forbidden. This means that during the electronic transition from the initial state to the final state, the parity of state should change in order to keep the integral non-vanishing [9]. This is also known as a selection rule. These rules are based conservation of energy, angular momentum, linear momentum, spin, and parity and represents the set of criteria that determine whether a particular transition is allowed or forbidden. For example, a transition is "allowed" when it satisfies the selection rules and is therefore permitted according to the laws of quantum mechanics. On the other hand, a transition is "forbidden" when it violates one or more of the selection rules and is thus prohibited or significantly less likely to occur.

1.2.1 Frank-Condon principle

The electronic wave function depends on the position of nuclei, even though their motion is ignored. Generally, the nuclear motion is described by a harmonic Morse potential, with the horizontal lines representing the vibrational energy levels of the electron. The Frank-Condon principle is a consequence of the Born-Oppenheimer approximation [10]. This principle depends on the overlap integral of the wave function of initial and final state of vibronic

motion of nuclei, also known as the Frank Condon overlap integral and the square of it is called the Frank Condon factor [11]. It predicts the probability of transition from the 0th vibration level of the ground state to the nth vibrational level (n>1) from the first electronic state to higher electronic states for absorption and vice versa for emission. In the limit of harmonic oscillation of normal modes with the angular frequency ω_n and reduced mass M, the Frank-Condon factor can be described by the change in equilibrium coordinate Δq as given in equation 4:

$$I_{0\to n} = \langle \Phi_{vib_f} | \Phi_{vib_i} \rangle^2 = \frac{1}{2} M \omega_n \frac{\Delta q^2}{\hbar} \tag{4}$$

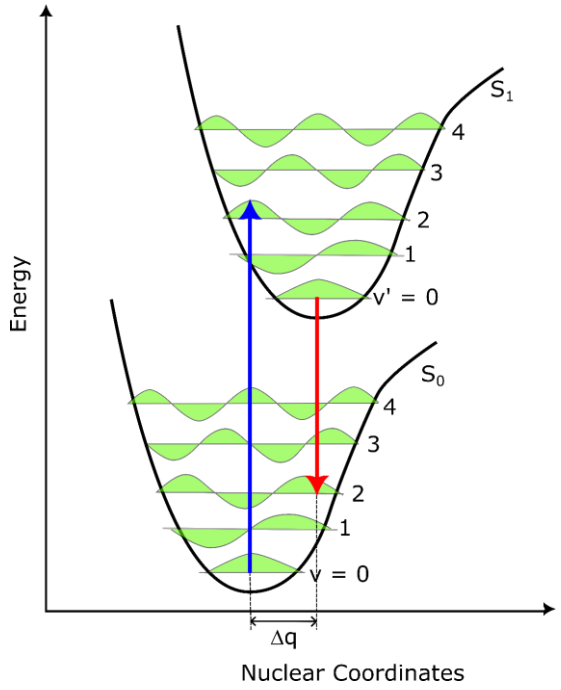

Figure 1.5: Franck-Condon principle in an energy diagram, depicting electronic transitions using vertical lines.

According to this principle, electronic transitions always occur vertically at a constant nuclear coordinate in the potential energy diagram shown in Figure 1.5. The Franck Condon principle is responsible for the different spectral shapes of absorption and emission. In the case of stiff organic chromophores molecules with rigid bonds, the displacement in the ground state and excited state potential energy curve is minimal, and consequently, the 0-0 transition is dominant. But for the flexible chromophores, a higher vibrational transition may form the peak of transition. For example, in Figure 1.5, the transition from 0-2 is dominant in the case

of absorption, as indicated by the blue arrow. Due to same spacing between vibrational levels, 0-2 is also the dominant transition peak in the emission as depicted by red arrow [12].

1.2.2 Jablonski diagram depicts optical transitions in organic Chromophores

Jablonski diagram (JD) is a tool to visualize all types of transitions after the excitation of molecules [13]. As shown in Figure 1.6, electronic energy levels denoted by S_0, S_1 and S_2 represent the ground state, first excited state and second excited state respectively. All the energy levels are arranged in increasing order of the energy in a vertical direction by bold horizontal lines followed by vibrational level with lighter horizontal lines. The gap between vibrational levels decreases as energies increase and they will finally form a continuum [14,15].

In the ground state of organic chromophores, electrons are in the lowest energy state with zero net spins. When a photon has the energy equivalent to the difference in energy between two electronic states, that photon is absorbed and an electron is promoted from the low-lying energy state to the electronically excited singlet states S_n with $n \geq 1$, denoted by the vertical arrows in blue. The photon absorption occurs at a very fast time scale on the order of 10^{-15} s. Once the electron is excited, the energy is dissipated through radiative and non-radiative relaxations. The excited electron in the higher vibrational levels relaxes via a non-radiative process to the lower vibrational level via the process called vibrational relaxation (VR), indicated by the wavy arrow in yellow. This process occurs immediately after the absorption, on the time scale 10^{-14}-10^{-11} s. This relaxation occurs within the vibrational levels and the electron stays in the same electronic state. Another type of non-radiative transition called internal conversion (IC) occurs when electrons from the vibrational level of higher electronic states relax to electronic states of lower energy in the time range of 10^{-13}-10^{-9} s, keeping the same multiplicity of the electronic state, which can be seen by the dashed arrow in pink. Intersystem crossing (ISC) occurs when multiplicity of electronic state is changed during electron relaxation from a higher singlet excited state to a lower excited triplet state, as depicted by the sky-blue arrow, which occurs at a slower time scale of 10^{-10}-10^{-7} s, compared to IC. This transition is generally forbidden and only becomes weakly allowed when there

exists a vibronic coupling via spin-orbit interaction in the organic molecule [14].

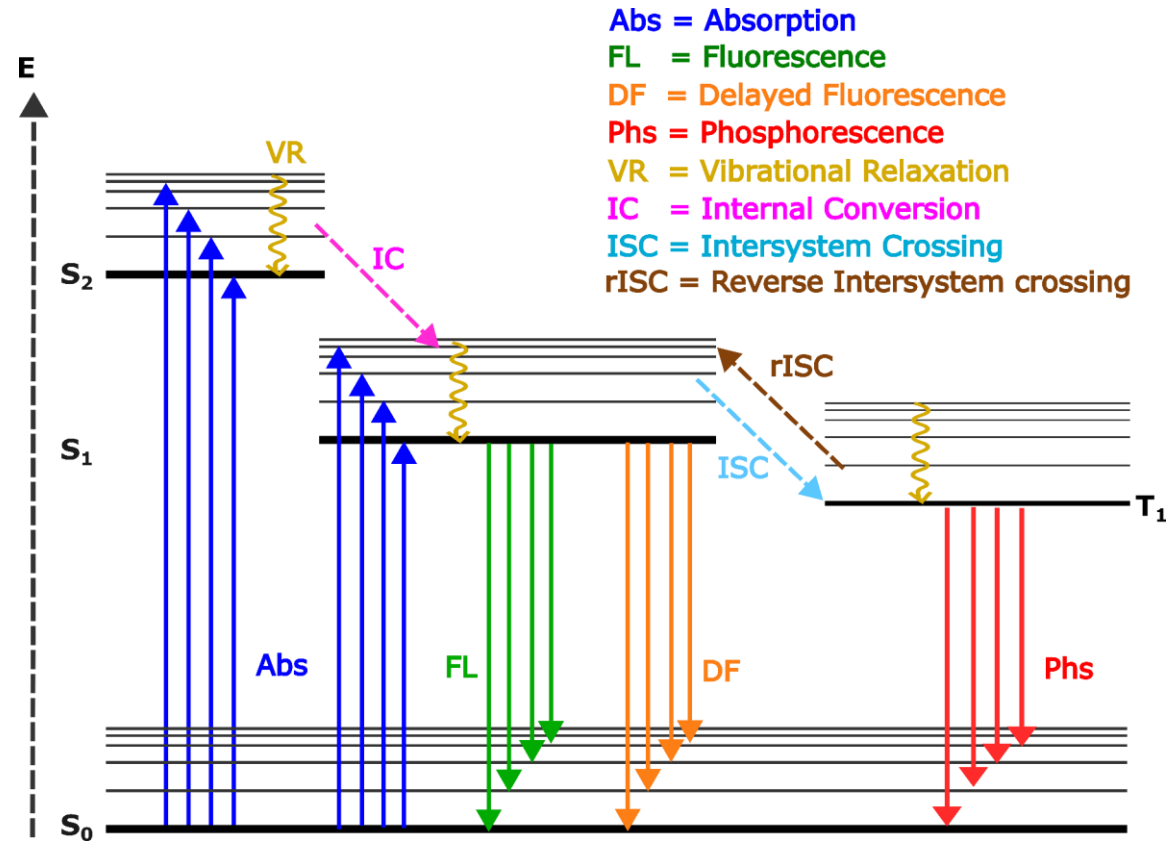

Figure 1.6: Jablonski diagram depicting radiative and non-radiative processes followed after the optical excitation of the organic chromophores.

From the first electronic singlet and triplet state, the electrons can relax radiatively to the ground state and these processes are called fluorescence and phosphorescence respectively. Fluorescence is represented by the downward arrow in green from the first singlet state to the ground state and occurs at 10^{-10}-10^{-7} s, while phosphorescence occurs at the time range of 10^{-7}-1 s, represented by the downward arrow in red from the first triplet state to the ground state [15]. In general phosphorescence is slower compared to other processes, since during phosphorescence the transition occurs from the triplet state to the singlet ground state, which is spin forbidden by Fermi's Golden rule, but is still weakly allowed. In some organic chromophores, the difference in the energy of the first singlet and triplet states is small enough that the electrons in the triplet state acquire enough energy at room temperature that they transition back to singlet states through the reverse intersystem crossing (rISC), as shown with the dashed brown arrow. This process typically occurs at 10^{-5}-10^{-7} s, and afterwards the electron then relaxes radiatively to the ground state. This mechanism results

in light emission spectrally identical to FL, but due to the slower time scale resulting from the ISC/rISC process, is called delayed fluorescence (DF) [16], as indicated by the downward orange arrow. There are other possibilities for photophysical processes like energy and charge transfer, which will be discussed in the next section.

1.3 Exciton formation in organic chromophores

Frenkel first introduced the concept of the exciton in 1931 into physics [17]. Excitons can be seen as the quantum of electronic excitation energy, just as a photon is considered a quantum of light. When organic chromophores absorb the photon, the electron jumps to the higher energy state and forms a stable bound state. The absence of an electron in ground state is called a hole, which has all the properties of the electron (e.g., mass, spin etc.), with the exception of having a positive charge. Exciton formation in organic semiconductors is different to what is found in their inorganic counterparts. Inorganic semiconductors have very large dielectric constants (for example $\epsilon_r = 11.68$ for silicon) in contrast to the low dielectric constant ($\epsilon_r = 3$) in organic chromophores. As a result, coulomb screening becomes significant and the electron-hole pair generated by optical excitation is bound strongly by coulomb forces. The potential energy which binds the excited state electron to the positive hole in the ground state is called the exciton binding energy. Typical values for exciton binding energies in organic molecules range from 0.1 to 1.0 eV [18,19]. External energy is required to ionize the exciton into free charge carriers, which is an important process for charge generation in organic photovoltaic cells. Excitons in organic molecules are almost exclusively of the Frenkel type. In contrast, excitons created in inorganic semiconductors, also known as Mott-Wannier excitons [20], are easily broken apart into free charge carriers. Thus, the exciton binding energy is crucial in determining the optoelectronic properties of the material.

1.4 Energy transfer in organic chromophores

Excitation energy transfer is a photophysical process in which an electronically excited chromophore or donor molecule transfers its excitation energy to the ground state

chromophore or acceptor molecule. Excitation energy transfer is a crucial process for both natural and artificial systems. For example, photosynthetic proteins in plants and bacteria use their antenna complexes (consisting of densely packed chromophores called chlorophyll) to capture the sun's energy and then transfer this energy to a reaction-center (a different chromophore complex, also comprising chlorophyll pigments) where the light energy is converted into chemical energy. Similarly, in the case of both OLEDs and OPVs, excitation energy transport plays a crucial role in the performance of the devices.

In energy transfer, the initial state can be described by the donor in the excited state (D*) and the acceptor in the ground state (A). After the energy transfer, the donor relaxes to the ground state (D), and the acceptor is promoted to the excited state (A*). The transition matrix element describing the coupling between the initial and the final state in energy transfer is given by equation 5

$$V_{ET} = \langle \Psi_i | V | \Psi_f \rangle \tag{5}$$

Where, Ψ_i and Ψ_f are initial and final wavefunction of the donor-acceptor system before and after energy transfer, respectively and can be described by the two electrons' antisymmetric wavefunction having interchanging electron particles 1 and 2:

$$\Psi_i = \frac{1}{\sqrt{2}}\left(\Psi_{D*}(1)\Psi_A(2) - \Psi_{D*}(2)\Psi_A(1)\right) \tag{6}$$

$$\Psi_f = \frac{1}{\sqrt{2}}\left(\Psi_D(1)\Psi_{A*}(2) - \Psi_D(2)\Psi_{A*}(1)\right) \tag{7}$$

Excitation energy transfer can be classified into weak or strong electronic coupling cases depending on the excitation energy transfer coupling element V_{ET} between the donor and acceptor chromophores. In the weak coupling limit, excitation energy is localized entirely at the donor, and localized excitation energy can jump irreversibly from the donor to the acceptor. On the other hand, in the limit of strong coupling, excitation energy is delocalized over both the donor and acceptor chromophores and creates the coherent motion of excitons [21]. This example is relevant in aggregated systems, discussed further in section 1.6.

1.5 Weak coupling limit

In the weak coupling limit, excitation energy transfer is completed by a resonance mechanism, also known as the Förster mechanism, which is named after the famous German scientist Theodor Förster. Förster used Fermi's Golden rule and expressed the coupling by a radiation-less dipole-dipole transition of the donor and the acceptor, which is only applicable for chromophores capable of optically allowed transitions. During the so called Förster resonance energy transfer (FRET), the spin of an exciton remains unchanged. Dexter further extended the Förster mechanism to the system of chromophores which undergo spin change during the energy transfer and are optically forbidden within the framework of Fermi's Golden rule. This process is called Dexter Energy Transfer (DET) and is also referred to as electron exchange.

In the limit of weak coupling, the energy transfer is treated as a small perturbation in the system given by $V = \frac{e^2}{r_{12}}$, where r_{12} is the distance between the electrons. Using the equations (5,6, and 7) the coupling transition element is given by

$$V_{ET} = \left\langle \Psi_{D*}(1)\Psi_A(2) \left| \frac{e^2}{r_{12}} \right| \Psi_D(1)\Psi_{A*}(2) \right\rangle - \left\langle \Psi_{D*}(1)\Psi_A(2) \left| \frac{e^2}{r_{12}} \right| \Psi_D(2)\Psi_{A*}(1) \right\rangle \quad (8)$$

$$V_{ET} = \text{Coulombic interaction} + \text{Electron exchange interaction}$$

The first term on the right-hand side of the equation 8 describes the Coulombic interaction when the excited donor relaxes by exciting the acceptor through transferring its energy, which is possible only for spin-allowed transitions (FRET). The second term in equation 8 demonstrates that two electrons were exchanged during the energy transfer and describes the electron exchange interaction (DET). The schematic of FRET and DET is shown in the Figure 1.7. We will now discuss both processes in a bit more detail.

1.5.1 Förster resonance energy transfer

FRET occurs for a donor-acceptor system having large intermolecular distances. It is also referred to as a long-range interaction. Consequently, the exchange term becomes negligible due to a lack of orbital overlap and equation 8 becomes:

$$V_{ET}{}^{Coul} = \left\langle \Psi_{D*}(1)\Psi_A(2) \left| \frac{e^2}{r_{12}} \right| \Psi_D(1)\Psi_{A*}(2) \right\rangle \quad (9)$$

In the Born-Oppenheimer approximation, the total wavefunction can be separated into electronic and vibronic parts $\Psi = \Phi_e\Phi_{vib}$ and therefore the Coulomb interaction can be approximated by a dipole-dipole transition which is given by equation 10:

$$V_{ET}{}^{Coul} = \frac{\mu_D\mu_A}{r^3}\kappa \quad (10)$$

Where, μ_D and μ_A are the transition dipoles for the individual donor and acceptor

The rate of energy transfer is derived using Fermi's Golden rule and is expressed as:

$$K_{ET}{}^{Coul} = \frac{1900\ \ln(10)\ Q_D\kappa^2}{128\pi^5 n^4 N_A \tau_D r^6} \int_{-\infty}^{\infty} I_{Fl,D}(\tilde{\nu})\varepsilon(\tilde{\nu})\frac{\partial(\tilde{\nu})}{\tilde{\nu}^4} \quad (11)$$

Where Q_D and τ_D is quantum yield and fluorescence lifetime of the donor chromophore, respectively; n is the refractive index and N_A is Avagadro's constant. The part that belongs to the integral includes the normalized fluorescence intensity area and extinction coefficient $\varepsilon(\tilde{\nu})$, which constitute the overlap integral J, implying that efficient energy transfer requires the overlap between the acceptor's emission spectrum and the donor's absorption. With the exception of τ_D and r, the entire expression is combined and assigned to R_0, called the Forster critical radius. Förster radius constitutes an essential parameter and is defined as the distance between donor and acceptor at which the rate of energy transfer becomes equal to the fluorescence rate of the donor. It simplifies the rate energy transfer equation to

$$K_{ET}{}^{Coul} = \frac{1}{\tau_D}\left(\frac{R_0}{r}\right)^6 \quad (12)$$

Forster energy transfer induced by Coulombic coupling depends on the distance between the donor and acceptor and decreases with the inverse sixth power of distance. However, the

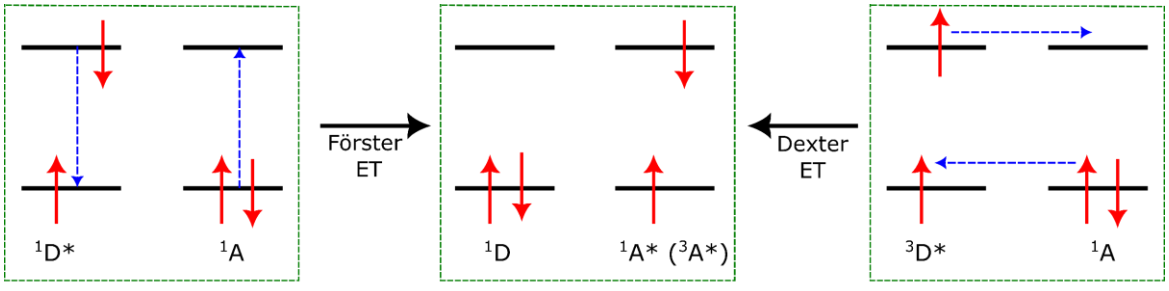

Figure 1.7: Schematic representation of the Förster and Dexter energy transfer mechanism between a donor and an acceptor molecule.

equation is strictly valid for the donor-acceptor distances greater than the size of chromophores and can proceed up to 10 nm. With small interchromophoric distances, the exchange interaction becomes significant and can no longer be neglected, rendering the dipole-dipole interaction invalid [22].

1.5.2 Dexter energy Transfer:

As shown in Figure 1.7, when the energy transfer involves a spin flip, i.e., when donor and acceptor physically exchange electrons, the Columbic interaction becomes zero, and the transition matrix element can be expressed by and electron exchange interaction given by:

$$V_{ET}{}^{Exc} = \left\langle \Psi_{D*}(1)\Psi_{A}(2) \left| \frac{e^2}{r_{12}} \right| \Psi_{D}(2)\Psi_{A*}(1) \right\rangle \quad (13)$$

Dexter [23] described the exchange interaction as an electrostatic interaction between the two electron clouds where the electron density decreases with the increase in distance from the centre of the charged cloud in an exponential way. Using Fermi's Golden rule with the assumption of hydrogen-like orbitals (In hydrogen-like atoms, the eigenvalues are proportional to $1/n^2$) , the rate of Dexter energy transfer is given by

$$V_{ET}{}^{Exc} = \frac{2\pi}{\hbar} K J \exp\left(\frac{-2r}{L}\right) \quad (14)$$

Where J is the normalized overlap integral between donor's emission and acceptor's absorption, K is the experimental factor, r is the distance between the donor and acceptor and L is the van der Waals radius of the D*- A and the D-A* molecular orbital.

Besides the overlap integral, the exchange energy interaction requires the overlap of the wavefunction of the donor and acceptor, which implies that the donor and acceptor should be in close proximity to each other so that the exchange can happen. Due to this reason, it is also referred to as a short-range interaction, and the efficiency of Dexter energy transfer decreases exponentially with the interchromophore distance [24].

In the weak coupling limit, where the interaction between the donor and acceptor molecules is relatively weak, the formation of CT (Charge Transfer) excitons is more likely. In this regime, the electronic states of the donor and acceptor molecules remain relatively separate, and the exciton formation occurs primarily through charge transfer between the two entities. The

energy level offset between the donor and acceptor creates an energetic driving force for charge transfer, leading to the formation of CT excitons. CT excitons in the weak coupling limit involve a spatially separated electron and hole, with the electron localized on the acceptor and the hole on the donor. This charge transfer process results in an exciton state where the electron and hole are delocalized across the donor-acceptor interface. The weak coupling limit is particularly favorable for CT exciton formation because the weak interaction allows for efficient charge transfer and delocalization of the exciton across the donor-acceptor interface. These CT excitons often exhibit unique optical and electronic properties compared to purely localized excitons. In the context of organic donor-acceptor systems and organic semiconductors, the weak coupling is frequently employed to achieve efficient charge transfer and TADF (Thermally Activated Delayed Fluorescence) processes. By carefully designing the molecular structure and energy level alignment, weak coupling can be tailored to facilitate CT exciton formation and subsequent TADF emission, leading to highly efficient organic light-emitting diodes (OLEDs) and other optoelectronic devices [25].

1.6 Strong coupling limit:

The strong coupling limit refers to a situation when an excited monomer chromophore (donor) interacts via strong Columbic coupling with the neighboring identical chromophore (acceptor). In this case, the excitation energy transfer occurs such that the excitation energy is no longer localized on a single monomer, but it is delocalized over the entire chromophoric system (dimer). It occurs when the energy exchange between the chromophores is rapid and results in a new set of eigenstates known as exciton states and the excitation energy is exclusively treated as excitons.

In the case of the strong coupling limit, the exchange interaction is negligible compared to Columbic coupling. Due to strong Columbic coupling, the excited state energy level is split into two excitonic state levels, E' (lower) and E'' (higher) separated by the twice the coupling term $\mathrm{V_{ex}}$. The energy splitting between the lower and upper exciton states is larger than the decay rates or dephasing rates associated with the individual chromophores. This means that the energy levels of the system are no longer defined solely by the individual chromophores

but rather by the collective behavior of the coupled system. The chromophores become entangled, and their properties and behaviors are no longer independent.

The exciton state energy is given by the linear combination of the zero-order excited state of monomers M_1 and M_2, with excited energy localized on one of the monomers ($M_1{}^* - M_2$) and ($M_1 - M_2{}^*$). In this case, the coupling term is approximated in the same way as in Förster energy transfer using dipole-dipole multipole expansion.

$$V_{ex} = \frac{\mu_{M_1}\mu_{M_2}}{r^3}\kappa \tag{15}$$

This implies that the exciton splitting V_{ex} depends on the magnitude and orientation of the absorption transition dipole moment of the individual chromophores. The aggregate system is divided into two categories depending upon the relative orientation between the chromophores. The value of the orientation factor κ becomes zero when the angle between the two chromophores is at $54.7°$ with each other and as a result, the coupling element vanishes at this angle called the magic angle. When the relative angle between the two chromophores $\varphi < 54.7\,°$, the coupling element becomes negative, leading to the formation of J-aggregates. It implies that two chromophores are stacked offset or more popularly referred to as having a head-to-tail arrangement. On the other hand, when the angle between the chromophore exceeds the magic angle $\varphi > 54.7\,°$, the system forms H-aggregates and the chromophores stack in the side-by-side orientation of the transition dipole, as shown in Figure 1.8. The stacking of the chromophores has a very strong influence on the absorption and emission properties of the aggregates and this provides a way to distinguish them with optical experiments.

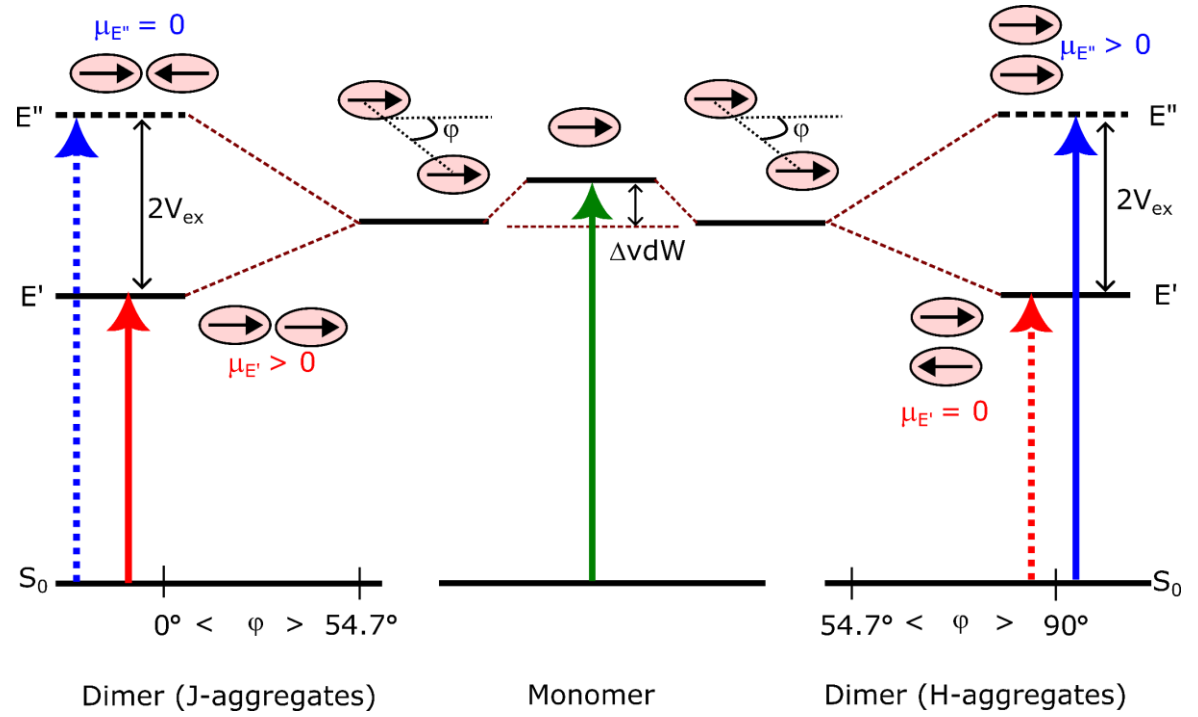

Figure 1.8: Schematic of an energy band diagram for the H- aggregate and J-aggregate resulting from the coupling of two organic chromophores.

The optical transition to the newly created excitonic states can be regarded as an induced oscillatory dipole and the magnitude of the transition moment depends on the dipole oscillator strength and the vector orientation of the dipole oscillation. For example, in an optical transition to/from the excitonic states E' and E'', the transition moment is given by the vector superposition of monomer transition moments. In the case of H-aggregates, the transition dipole moments μ_{M} are aligned parallel, with $\mu_{\mathrm{E}''} = \sqrt{2}\mu_{\mathrm{M}}$, having an in-phase oscillation of dipoles. The parallel orientation makes them electrostatically unstable and raises the energy of E'' with respect to the monomer. While the anti-parallel orientation (out-of-phase oscillation) lowers the energy of E' with $\mu_{\mathrm{E}'} = 0$, implying that in H-aggregates, the absorption of the dimer is shifted towards the higher energy compared to the monomer and the fluorescence from the lowest excited energy is quenched. In contrast, in J-aggregates, the dipole oscillation is oriented in-line, where diploes point towards each other in the case of E'', making the transition moment zero $\mu_{\mathrm{E}''} = 0$ to this state, while the excitonic state E' has a head to tail orientation with $\mu_{\mathrm{E}''} = \sqrt{2}\mu_{\mathrm{M}}$, making the transition possible for this state. Due to this, the absorption is shifted towards the lower energy compared to the monomer and fluorescence from this state is $\sqrt{2}$ greater in magnitude to the monomer. Thus, H-aggregates and J-aggregates can be characterized, respectively, by a blue or red shift in their absorption

spectrum compared to the monomer. Furthermore, the excitation coupling can be extended for several interacting chromophores.

1.7 Exciton annihilation in chromophores:

When two or more excitons come in close proximity of each other, they can also interact, resulting in non-radiative decay and quenching of the exciton. The process is called exciton-exciton annihilation (EEA) and it occurs via the same mechanism of FRET and Dexter. EEA is very crucial in determining the efficiency of various optoelectronic devices, like OLEDs. In OLEDs the efficiency decreases for high voltages, which is often attributed to bimolecular quenching processes due to EEA. There exist various annihilation processes such as singlet-singlet, singlet-triplet and triplet- triplet annihilation mechanisms which will be discussed in detail here.

In singlet-singlet annihilation (SSA), two excited singlet excitons interact resulting in the non-radiative relaxation of one singlet exciton to the ground state. The SSA process can be described by equation 16, where k_{SSA} is the rate constant:

$$S_1 + S_1 \xrightarrow{k_{SSA}} S_n + S_0 \tag{16}$$

During SSA, the spin of the exciton remains the same and there is no possibility of triplet formation.

Singlet-triplet annihilation can take place when an excited singlet exciton and triplet exciton interact with each other. This occurs when an excited donor transfers its energy to an acceptor which is already in an excited triplet state, resulting in the creation of higher excited triplet states. After relaxation back to the T_1 state, a singlet exciton has been lost, as shown in equation 17, where k_{STA} is the rate constant describing the STA process.

$$S_1 + T_1 \xrightarrow{k_{STA}} S_0 + T_n \longrightarrow S_0 + T_1 \tag{17}$$

Both STA and SSA processes were first discovered in an anthracene crystal and described by a long range dipole-dipole interaction via Förster resonance energy transfer [26].

In triplet-triplet annihilation (TTA), two excited triplet excitons interact with each other to form an intermediate state, which can further be converted into a singlet, triplet or quintet according to spin statistics rules. Since the quintet state lies higher in energy than the two initial triplet excitons the probability of their formation can usually be neglected [27], this leads to two possible pathways as shown below:

$$T_1 + T_1 \xrightarrow[75\%]{k_{TTA}} T_n + S_0 \longrightarrow T_1 + S_0 \quad (18)$$

$$T_1 + T_1 \xrightarrow[25\%]{k_{TTA}} S_n + S_0 \longrightarrow S_1 + S_0 \quad (19)$$

Where k_{TTA} is the kinetic rate constant of TTA. Thus, during this process, triplet excitons are quenched, but at the same time one singlet exciton can be created in the process.

1.8 Photoinduced electron transfer in organic chromophores

Photoinduced electron transfer as shown in equation 20, occurs when an excited state donor relaxes to the ground state via the transfer of an electron to the acceptor molecule, leaving behind a positively charged hole in the donor [28]. This hole remains Coulombically bound to the donor, however this binding is weakened compared to the excitation energy transfer exciton. This means that while the electron is transferred to the acceptor molecule, the hole remains associated with the donor molecule, forming a charged species. The weakened Coulombic binding allows for the eventual separation of the charges and the generation of free charges

$$DA \xrightarrow{h\nu} D^*A \xrightarrow{ET} D^+A^- \quad (20)$$

A photoinduced electron transfer in chromophores is considered a non-radiative process which is accompanied by the quenching of the fluorescence emission. It is one of the most critical processes in physics, chemistry and biology. In nature, photoinduced ET occurs in the photosynthesis process, where the sun's energy is utilized by a series of electron transfer steps to produce Adenosine Triphosphate. In the field of organic electronic devices such as OPVs, OLEDs or OFETs, ET plays a crucial role in charge separation, transport and device

performance. Electron transfer facilitates the separation of the exciton into free charges, which creates mobile charges that can be transported and collected as electrical current. The movement of the generated electron from the donor to the acceptor contribute to the efficient transport of charges within the device which is crucial for the overall performance of organic electronic devices. It influences parameters such as the power conversion efficiency of organic solar cells, the on/off current ratio in organic transistors, and the efficiency of charge collection in photodetectors.

1.8.1 Semi-classical Marcus theory

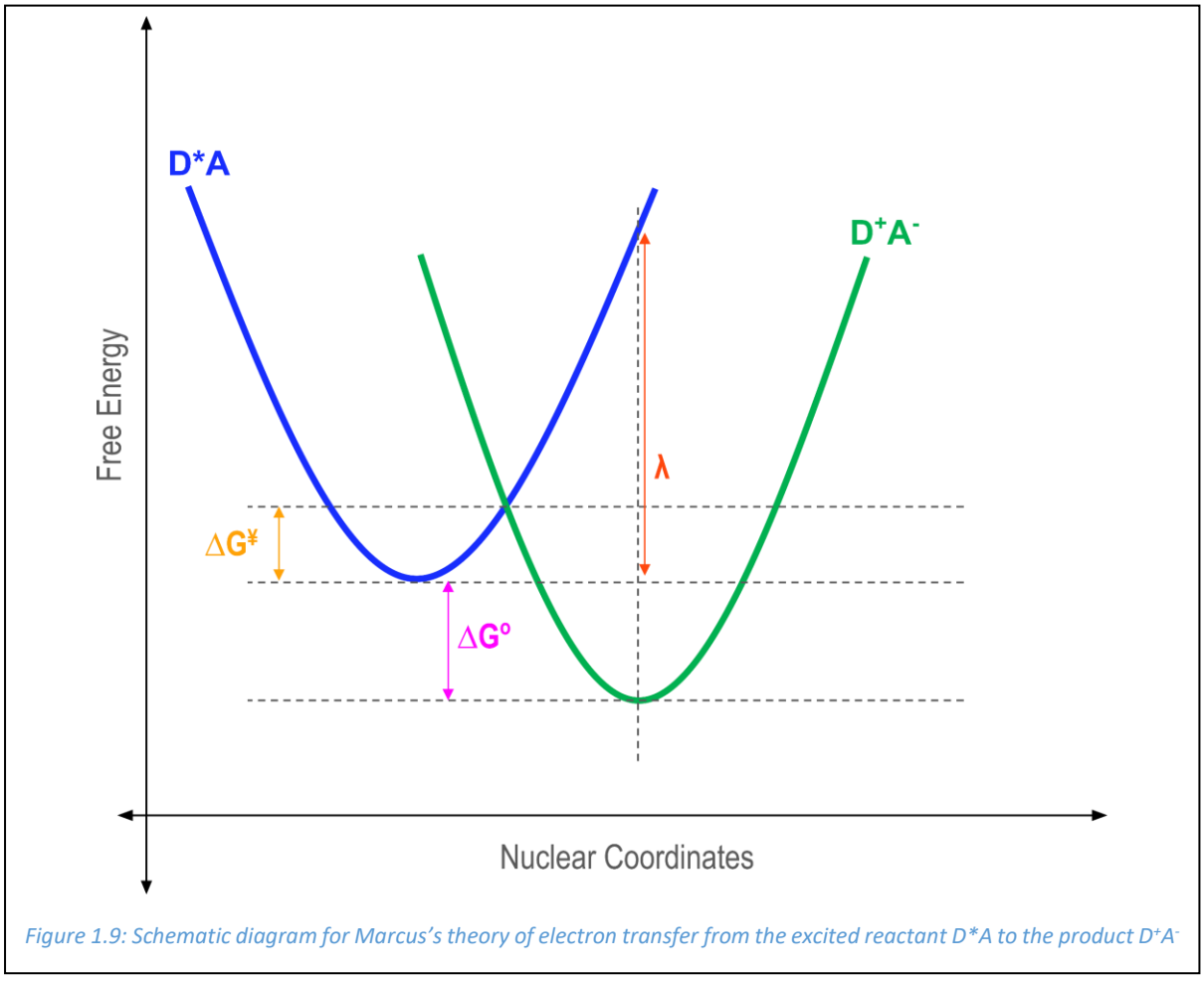

*Figure 1.9: Schematic diagram for Marcus's theory of electron transfer from the excited reactant D*A to the product D⁺A⁻*

Marcus theory [29] successfully describes the electron transfer reaction in the donor-acceptor system. The semi-classical approach is based on Boltzmann's distribution of energies and Fermi's golden rule to determine the rate of ET of the system in equilibrium. According

to Marcus, the ET transfer step satisfies the (i) Frank-Condon principle and (ii) conservation of energy, i.e. there should be no change in the configuration of nuclear coordinates of reactant and product during ET and the process should be isoenergetic. These conditions are satisfied at the intersection of the potential energy curve of reactant and product, as shown in Figure 1.9. The harmonic potential energy curve describes the energy of the donor and acceptor as a function of the nuclear coordinate. The rate of electron transfer within the non-adiabatic process is given by

$$k_{ET} = \frac{|V_{el}|^2}{\hbar}\sqrt{\frac{\pi}{K_B T\lambda}}\exp\left(-\frac{\Delta G^{¥}}{K_B T}\right) \quad (21)$$

Where $|V_{el}|^2$ is the electronic coupling between reactant and product and its value is small in the adiabatic process, $\hbar$ is the Planck constant, λ is the reorganization energy, defined as the energy required to make vertical electron transfer without changing the nuclear frame, and $\Delta G^{¥}$ is the energy barrier during the ET process, also called the activation energy. Solving the parabolic equation for the point of interaction, which is equivalent to the activation barrier, $\Delta G^{¥}$ gives:

$$\Delta G^{¥} = \frac{\lambda}{4}\left(1 + \frac{\Delta G^{o}}{\lambda}\right)^2 \quad (22)$$

Where, ΔG^{o} is the standard Gibbs free energy of the reaction and the reorganization energy λ is also composed of two terms, that is solvation energy term λ_o and vibrational energy term λ_i:

$$\lambda = \lambda_o + \lambda_i \quad (23)$$

While λ_i is estimated by calculating the force constant of all the molecular vibrations in both reactant and product, λ_o is determined by using the dielectric continuum model. According to this model, both donor and acceptor are assumed to be a sphere of radii r_D and r_A respectively. With the centre-to-centre distance r_{DA} between donor and acceptor and ε_{op} and ε_s the optical and static dielectric constant of the medium, λ_o is estimated to be:

$$\lambda_o = \Delta e^2\left[\frac{1}{2r_D} + \frac{1}{2r_A} - \frac{1}{r_{DA}}\right]\left[\frac{1}{\varepsilon_{op}} - \frac{1}{\varepsilon_s}\right] \quad (24)$$

The above equation shows that reorganization energy depends on the distance between donor and acceptor and the dielectric properties of the medium.

For photoinduced electron transfer, the change in the free energy of reaction can be calculated theoretically and experimentally using the Rehm-Weller equation [30,31]as given by:

$$\Delta G_{ET} = E^{red}(D^+/D) - E^{ox}(A/A^-) - \Delta G_{00} - \frac{e^2}{\varepsilon\, r_{DA}} \qquad (25)$$

Here, the $E^{red}(D^+/D)$ describes the reduction of the donor by loss of an electron and $E^{ox}(A/A^-)$ is the oxidation of the acceptor by a gain of an electron. ΔG_{00} denotes the energy of the donor in an excited state after the transition ($S_0 \xrightarrow{hv} S_1$) and the term $\frac{e^2}{\varepsilon\, r_{DA}}$ describes the Coulomb force experienced by the cation and anion of donor and acceptor after the electron transfer.

Thus, the rate of ET varies as a function of change in activation energy, Gibbs free energy and reorganization energy. Depending on these values, Marcus plotted the log of the ET rate as a function of Gibbs free energy, which is referred to as the Marcus parabola. The major consequence of the Marcus parabola is that it divides the ET rate into three regions viz, *Normal*, *Optimal* and *Inverted*. As shown in Figure 1.10 in the *Normal regime,* $0 < -\Delta G^o < \lambda$, the potential energy curves intersect between the equilibrium nuclear coordinates of reactant and products. It introduces a small activation barrier and the electron transfer process is somewhat favoured. The rate of ET increases and becomes maximum at $-\Delta G^o = \lambda$, called the *Optimal regime,* where the potential energy curves intersect at the equilibrium of the reactant and the reaction occurs barrier-less. When the potential energy curves cross outside the equilibrium coordinate interval defined by the reactant and product, the reaction occurs in the Marcus *Inverted regime*, $-\Delta G^o > \lambda$, as a consequence, the energy barrier is reintroduced into the system, and the rate of ET starts to decrease again as shown in the Figure 1.10. The inverted region effect on electron transfer was experimentally confirmed [32] thirty years after its prediction by Marcus.

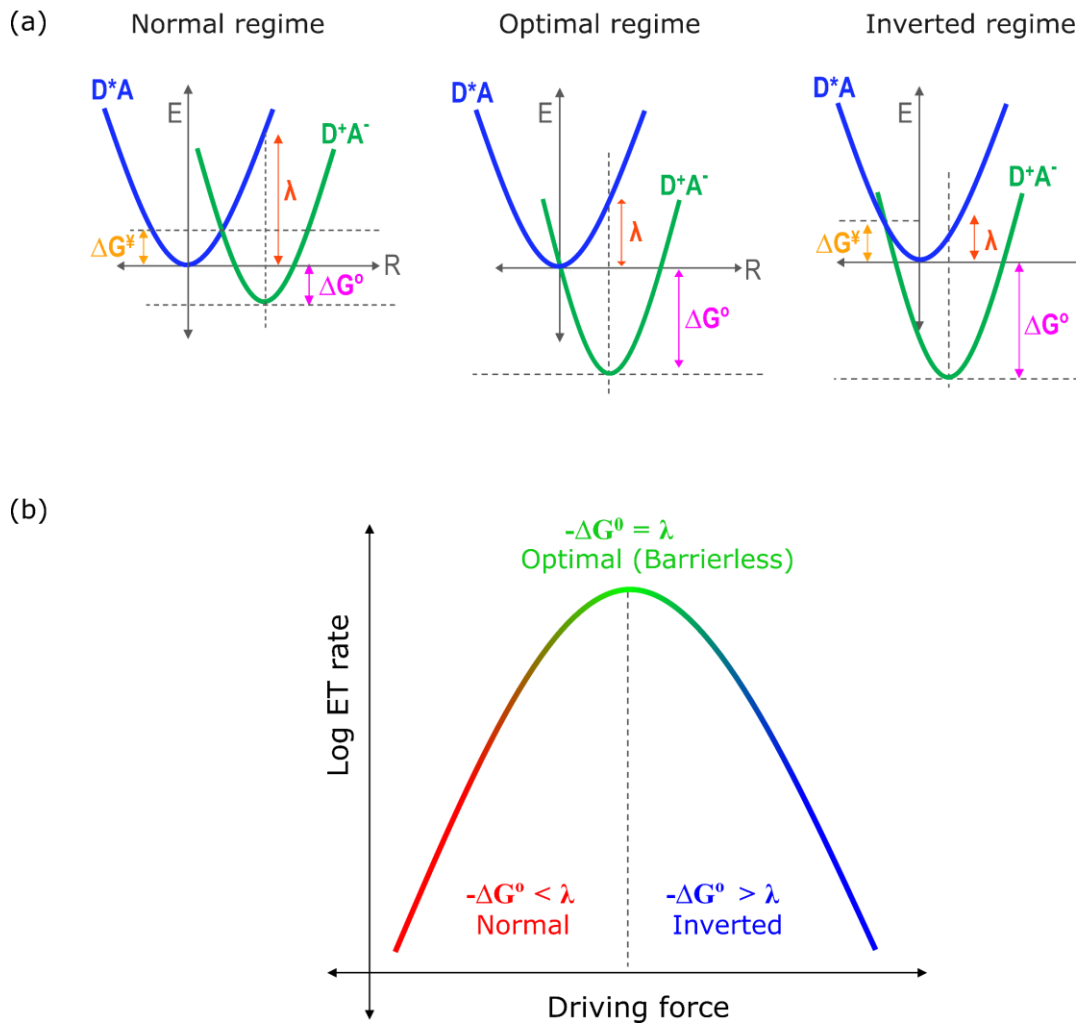

*Figure 1.10: (a) Schematic diagram for reactant D*A and product D+A- potential well of Marcus theory of electron transfer in three different regimes. (b) Dependence of rate of electron transfer on the free energy of reaction.*

1.9 Device applications of chromophores

In this thesis, the chromophores studied are mainly used in organic light-emitting diodes for TADF emitters and photo-electrochemical devices used in bio-hybrid photovoltaic applications, which will be discussed in the following section.

1.9.1 Organic light emitting diode

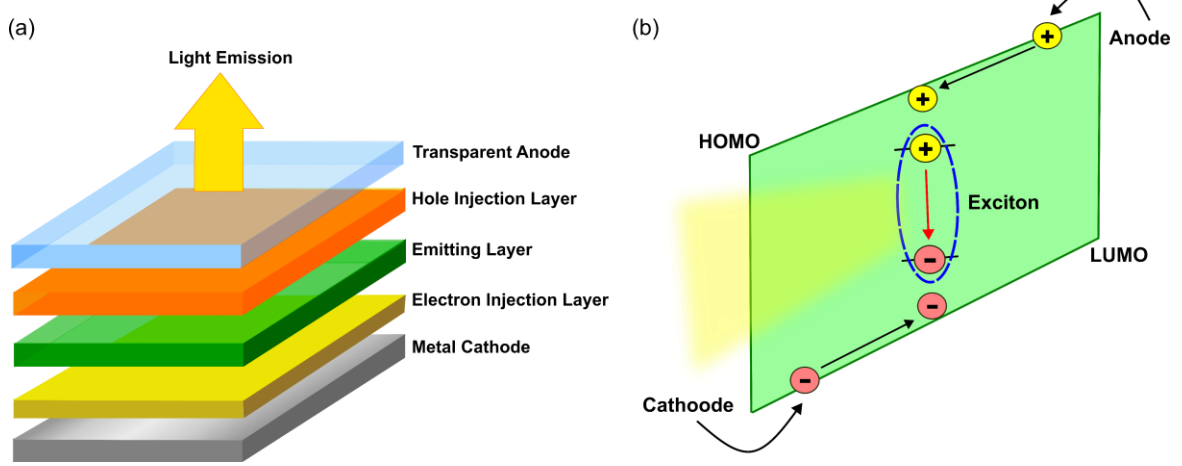

Figure 1.11: (a) Typical OLED device design. The organic emitter is sandwiched between a metal cathode and a transparent anode along with an electron injection and a hole injection layer. (b) Schematic of the OLED working principle. Electrons and holes are injected from anode and cathode into the HOMO and LUMO of the organic emitter. These electrons and holes drift towards each other and ultimately form an exciton. When these excitons recombine, it results in light emission from the OLED.

Organic light-emitting diodes (OLEDs) are commercially the most successful product based on organic materials. In an OLED, injected charges recombine to produce light. A simple OLED device design consists of an organic chromophore (emitter) acting as an emitting layer which is sandwiched between cathode and anode electrodes. One of these electrodes is transparent such that light can pass through it. Additional layers are often inserted between the emitting layer and the metal electrodes to enhance charge injection. These layers are called the electron injection layer (EIL) and hole injection layer (HIL). The typical device architecture of an OLED is shown in Figure 1.11 (a).

The working principle of an OLED device [33] is schematically shown in Figure 1.11 (b). Upon applying a suitable positive voltage to the device, electrons from the cathode and holes from the anode are injected into the LUMO and HOMO of the organic chromophore. The injected electrons and holes drift towards each other under the influence of the electric field over the device. When the distance between an electron and a hole becomes small, they form an exciton due to the Coulomb interaction between them (since organic materials have low dielectric constants, as discussed in section 1.2). Subsequently, when these excitons decay to their ground state, the recombination results in the emission of photon. The performance of OLEDs is usually measured by the external quantum efficiency (EQE). The EQE is defined as

the ratio of number of photons emitted to the number of charges injected into the device. One big problem for OLEDs is that they are operated at high currents, which leads to an efficiency decrease in TADF based OLED devices, something that is furthered studied and explained in chapter 3.

1.9.2 Biophotovoltaic device

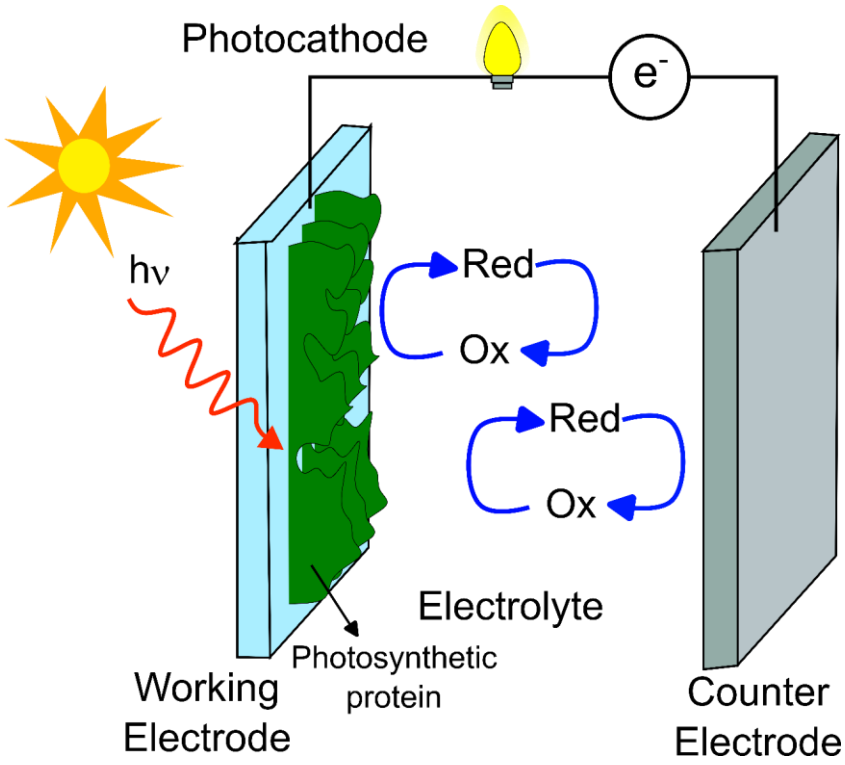

Figure 1.12: Working principle of the biophotovoltaic device, fabricated using a photosynthetic protein as an active material in the photoelectrochemical cell.

The third generation of solar cells utilizes plant/bacteria-based photosynthetic proteins as an active material for capturing the sun's energy and this field is called biophotovoltaics (BPV). Photosynthesis is the process of converting solar energy to chemical energy. The photosynthetic protein-pigment complexes are capable of 100% charge separation efficiency which inspired researchers to use these complexes in photovoltaic devices [34]. It is similar to a photoelectrochemical cell. A full device consists of protein immobilized electrodes called the photocathode immersed in an electrolytic solution containing external electron donor and acceptor molecules and a counter electrode. The basic principle of the device operation is shown in Figure 1.12. When incident light shines on the photocathode, the photosynthetic

protein absorbs the photons and generates electron-hole pairs. The photogenerated electrons are transferred through the electrolytic solution through a mediator to the counter electrode. At the counter electrode, the electron is accepted and travels through the external circuit to the photocathode, where it reduces the oxidized photosynthetic protein, resulting in the steady flow of current [35].

Chapter 2 : Experimental Methods

2.1 Ultrafast spectroscopy

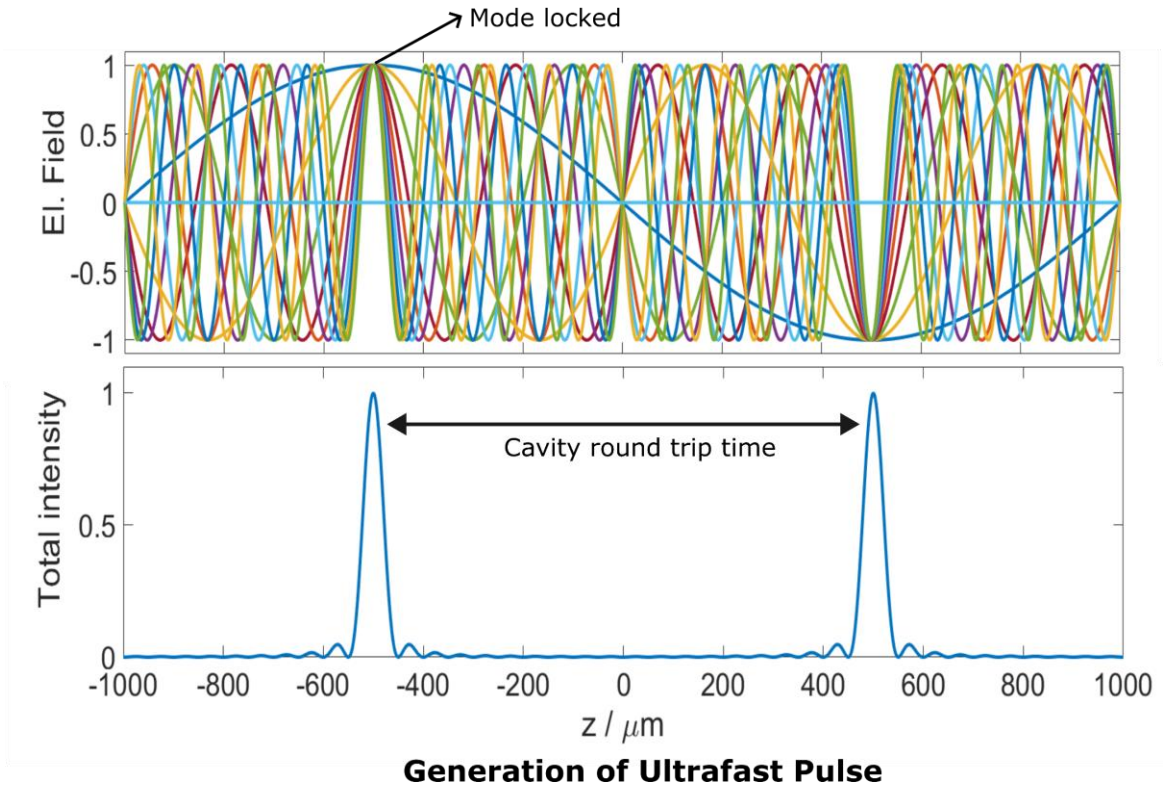

Figure 2.1: Ultrafast generation of laser pulse using the Mode-locking technique. The above picture depicts the mode-locking in a resonator of a cavity length of 1000 μm with 50 different longitudinal modes interacting. The ultrashort pulse is only generated at the point in space where all the 50 modes are in same phase due to constructive interference, whereas destructive interference take place everywhere else.

Ultrafast spectroscopic techniques use short laser pulses to study the dynamics of events on extremely fast timescales, usually on the order of a few femtoseconds (fs) to milliseconds [36]. The ultrafast spectroscopic field has grown tremendously since the invention of the laser in 1960, due to technical advancements in the generation and control of ultrafast pulses and the development of different spectroscopic techniques in general [37]. This thesis mainly focuses on studying electron and energy transfer dynamics on an ultrashort time scale; therefore, a basic understanding of the fundamentals of the ultrafast laser is essential. This chapter describes the fundamentals of fs laser pulses, their generation via mode-locking, amplification via chirped pulse amplification (CPA) and tunability via optical parametric amplification (OPA). The techniques of femtosecond transient absorption (TA)

spectroscopy and time-resolved photoluminescence spectroscopy (TRPL) are introduced and their application in understanding the photophysics of organic chromophores is described.

2.2 Generation of ultrafast laser pulse

A femtosecond laser pulse of tunable wavelength is employed to study the molecular dynamics in ultrafast spectroscopy. The principle of *mode-locking* is used to generate a train of light pulses, which are further amplified to be utilized in the experiments, this is done via *chirp-pulse amplification*. Finally, to study the system dynamics of the material, it must be excited with specific wavelengths resonant with the optical absorption of the material. The laser pulse must be tuned to variable excitation energies, which is accomplished through *optical parametric amplification*. We will now look into these three fundamental principles in a bit more detail.

2.2.1 Mode-locking technique

A laser generally consists of an amplifier as a gain medium with a pump and a feedback system as an optical cavity. A laser typically consists of several sets of frequencies and the standing waves constituting the discrete frequencies are called longitudinal modes, oscillating independently in the laser cavity. The mode-locking technique is used to generate fs/ps ultrafast laser pulses. The mode-locking technique principle relies on establishing a fixed phase relationship between different longitudinal modes traveling in a laser cavity. Discrete standing waves or longitudinal modes are formed depending on the wavelength of the light and length of the resonator cavity, which interferes constructively or destructively depending on the phase difference between the modes. These modes are separated by frequency $\Delta\nu = \frac{C}{2L}$ where c is the speed of light and L is the length of the resonator. When the phase relationship between different modes is fixed the modes are synchronized. All the modes of different frequencies interfere constructively at a particular time and destructive interference occurs at all other points in time. This phenomenon creates a very short burst of light called an ultrafast laser pulse. The repetition rate of the laser pulse train depends on the dimension of the laser cavity. For a typical Ti: Sapphire laser, the

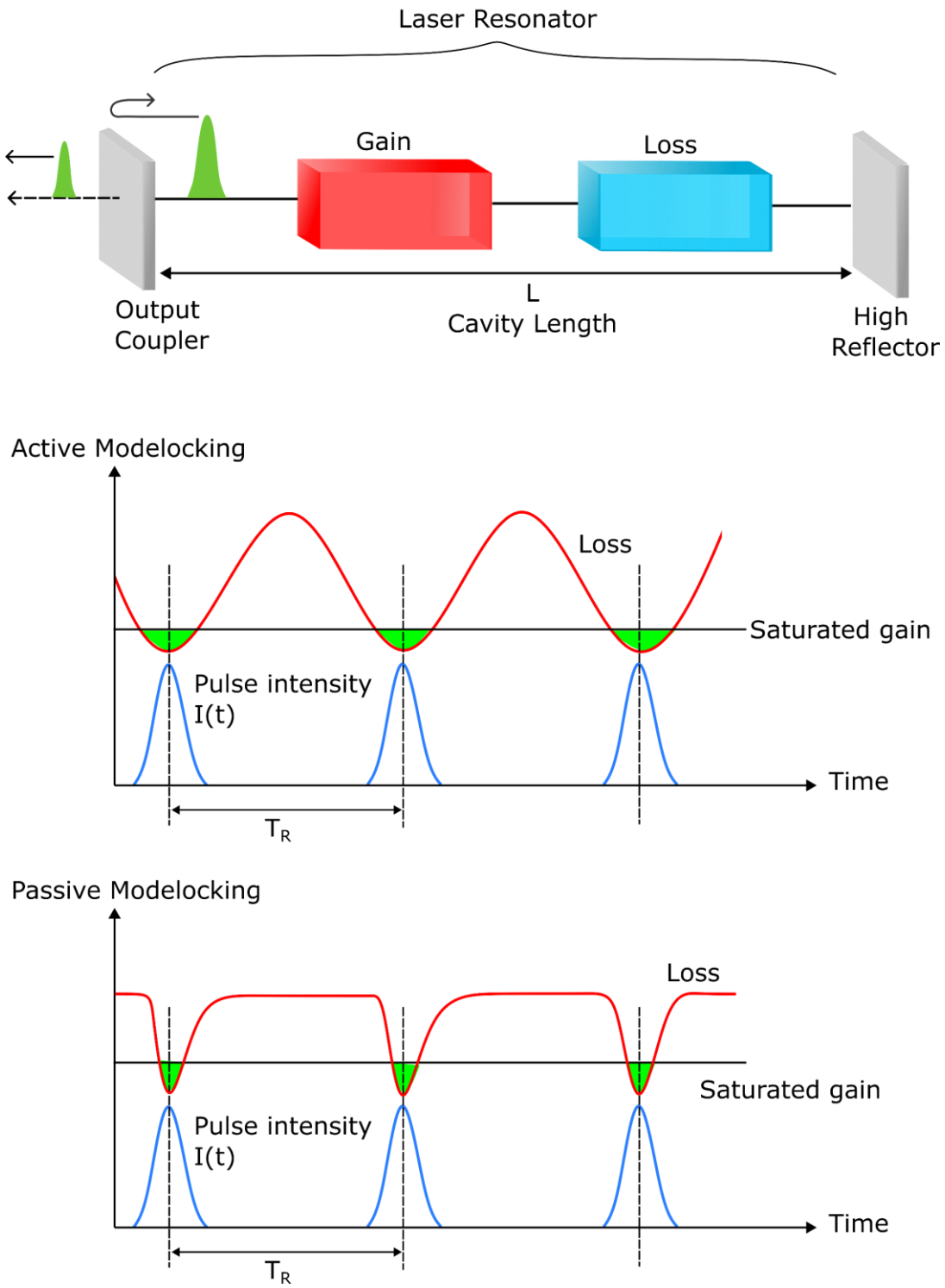

Figure 2.2: Realization of active and passive Mode-locking principle in a laser resonator

repetition rate is around 80 MHz, but a repetition rate in GHz is also possible. There are several different mechanisms to achieve mode-locking, and they can be classified either as active mode-locking and passive mode-locking. Active mode-locking works on the principle of

modulation of the resonator loss or phase change during the round trip. An acousto-optic or electro-optic modulator used in this process is synchronized with the round-trip time of the cavity resonator. This way, the laser pulse with zero round trip gain passes through the modulator when the resonator loss is minimal, while the radiation with negative round-trip time attenuates, leading to a higher gain for the modelocked pulses [38]. In addition, the pulse duration is shortened during each round trip in active mode-locking. It happens because the pulse vibration passing through the modulator has a slightly negative round-trip gain at the edges as compared to the pulse's center. After thousands of pulse circulations, a steady state is reached. At this stage, pulse shortening is balanced by other pulse broadening effects. Passive mode-locking is done by introducing a saturable absorber to modulate the loss of the laser resonator. The saturable absorber saturates by high-intensity pulses, allowing the pulse to pass, but attenuating the long low-intensity pulses. Passive mode-locking produces a shorter pulse and modulates the saturator loss faster than active mode-locking. However, active mode-locking is preferred when synchronization is required with an external electrical signal. Nowadays, Kerr lens mode-locking is used to generate an ultrafast pulse. It is a passive mode-locking method that relies on the non-linear optical Kerr effect. Due to the Kerr effect, the refractive index of the medium becomes intensity-dependent, due to which high-intensity pulse experiences self-focusing. Using Kerr lens mode-locking, a shortest pulse of 5 fs has been achieved in a Ti: Sapphire laser [39].

Depending on the application of the laser, specific experiments might require a very temporally narrow laser pulse. The width of the pulse generated by the laser depends on the number of modes available for mode-locking. This implies that the laser gain medium should have a large bandwidth to support many modes in order to generate a narrow laser pulse. For example, the commercially available Ti: Sapphire crystal can support thousands of such modes and pulse width as short as 5 fs can be achieved [40] . However, the bandwidth and pulse duration of the laser is fundamentally connected by the uncertainty principle. The bandwidth $\Delta\nu$ of the Gaussian-shaped pulse and the time duration Δt are given by

$$\Delta\nu\Delta t = \frac{2\ln 2}{\pi} \cong 0.44$$

It is commonly referred to as the time-bandwidth product. In experiment design, a trade-off between the spectral bandwidth and pulse duration needs to be considered. According to this

relation, both the bandwidth and pulse duration can't be infinitesimally small. For example, for ytterbium-doped YAG (Yttrium Aluminum Garnet), emitting at 1030 nm with a 200 fs pulse duration results in a bandwidth of 7.8 nm, which can be further increased to higher values if the pulse duration is shortened.

2.2.2 Chirp pulse amplification

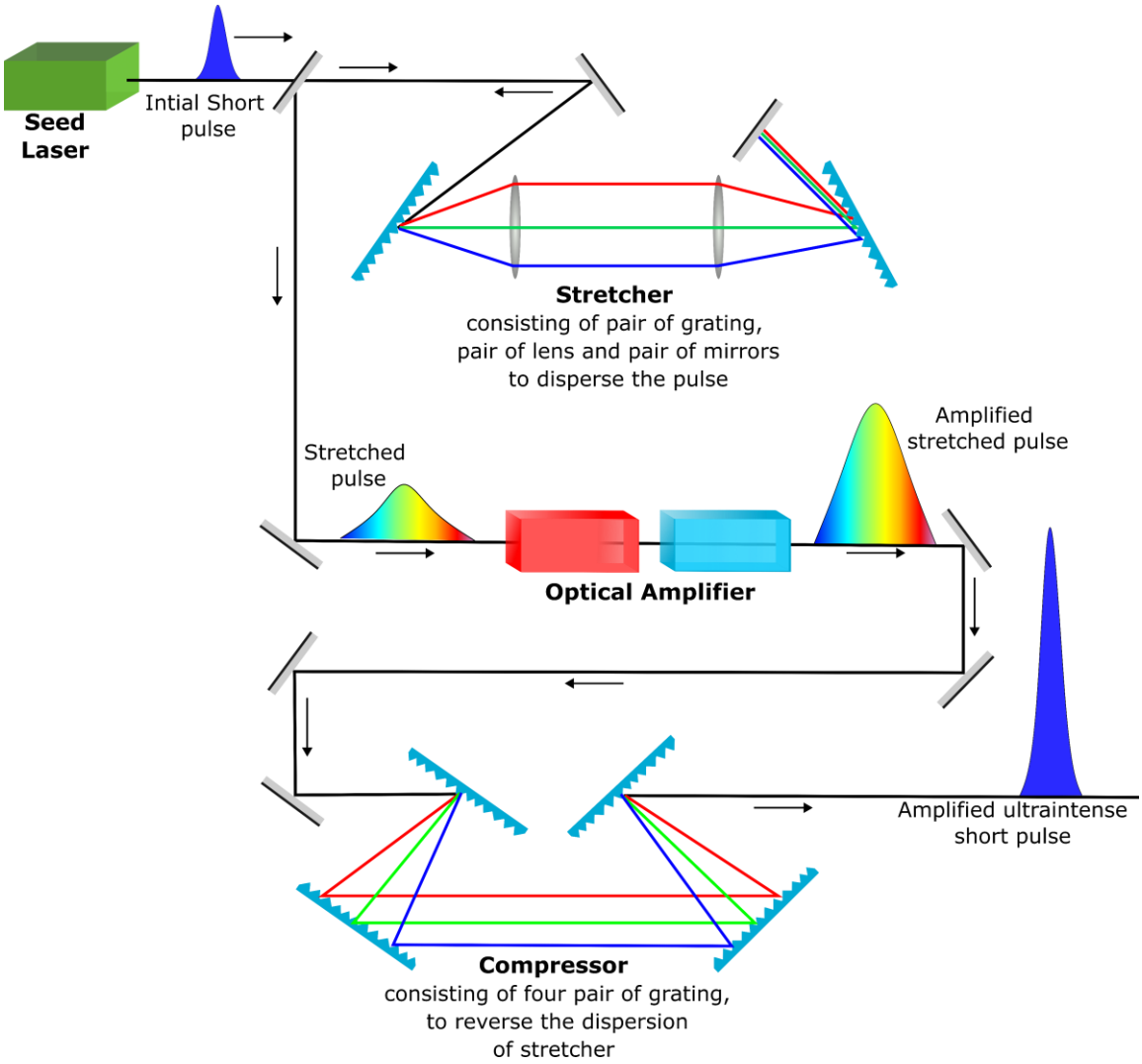

Figure 2.3: Schematic of chirp pulse amplification laser. The diagram shows the three stages of CPA, the low intensity ultrashort laser seed pulse is temporally stretched, then amplified in the gain medium and finally recompressed back to high intensity ultrashort pulse.

Several laser amplifications require high peak power of the laser pulse. However, laser pulses of a few GW cm^{-2} can invoke non-linear phenomena such as self-focusing, second harmonic generation, optical parametric amplification, etc., which play an important role in ultrafast

spectroscopy. It implies that low-energy fs mode-locked laser pulses need to be amplified to reach the intensities required for non-linear processes. However, laser pulses of these high intensities can cause severe damage to the gain medium and other laser components like mirrors and lenses due to the self-focusing Kerr effects in the medium. In 2018, the chirp pulse amplification (CPA) technique was developed to solve this limitation [41]. The CPA technique keeps the laser pulse intensity below the threshold for non-linear processes. The working principle of CPA is shown in Figure 2.3, which works in three steps.

Pulse Stretching: the initial pulse from the seed laser is stretched in time by a factor as large as 10^4 times before introducing it into the laser gain medium. This is achieved with the help of a dispersive optics element, in most cases diffraction gratings. The grating pairs are arranged to introduce the spatial separation between the pulse spectrums. The low-frequency modes, i.e., the red component of the pulse is forced to travel a shorter distance than the high-frequency blue modes, which positively chirp the laser pulse, meaning the high-frequency modes lag behind the low-frequency modes, which results in temporal stretching of the pulse with reduced peak power. The stretched pulse is then safely directed to the laser gain medium.

Pulse Amplification: The stretched pulse is amplified in an energized solid-state gain medium such as a Ti: Saphire crystal, neodymium-doped YAG crystal, or even glass. The optical crystal is excited before the arrival of the stretched pulse to achieve population inversion, using a separate high-powered pump laser. The stretched pulse laser is introduced at this point and causes the stimulated emission in the crystal. The laser pulses travel in the cavity several times until the stimulated emission removes the population inversion and ceases the amplification and only then the pulse is ejected from the cavity. The temporal synchronization between the pump, the laser pulse, and the input stretched pulse is achieved using an electronic device.

Pulse compression: In this step, the amplified stretched laser pulse is re-compressed to the original initial pulse duration. It is the reverse process of the pulse stretching step, usually achieved by employing four pairs of gratings to reverse the dispersion of the stretcher. During the process, the low-frequency red mode of the pulse is forced to travel a shorter distance than the high-frequency blue part, which negatively chirps the pulse and temporally compresses the pulse to a duration similar to the original input width. Thus, an ultrashort

laser pulse with several orders of magnitude more intensity is achieved than the optical amplifier could generate without CPA.

Following this procedure, a high-powered laser pulse with an intensity suitable for the non-linear optical parametric amplification process is possible. Optical parametric amplification is needed to tune the laser pulse to the desired wavelength.

2.2.3 Optical parametric amplifier

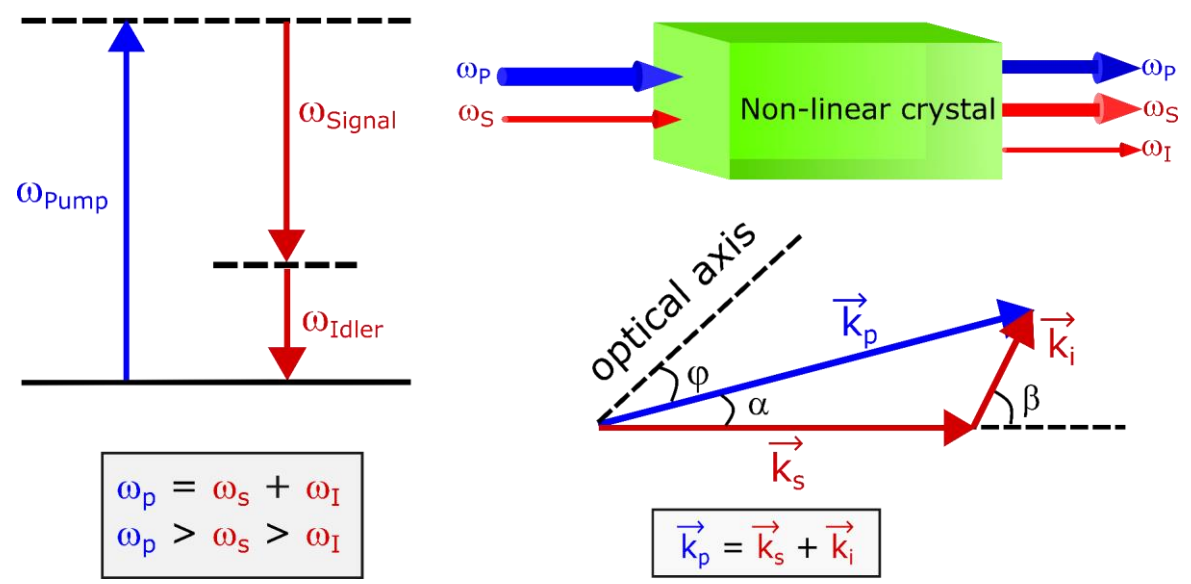

Figure 2.4: Principle of optical parametric amplification in a non-linear medium. When a second order non-linearity material is excited with a pump beam to higher excited level, it relaxes back to ground state by emitting two photons called signal and idler such that total energy is conserved. The Optical parametric amplification occurs when it also satisfies the phase matching condition.

Depending on the optical transition of the material under study, a different wavelength is required to excite the sample during an ultrafast spectroscopic measurement, which requires a broadband tunable light source from UV to near IR spectrum. OPA is the name of the technique that is usually used when tuning in the wide wavelength range that is needed for the ultrashort laser pulse [42]. OPA employs the second-order nonlinearity of a certain crystal to transfer the energy from a high-intensity, narrowband pump pulse of fixed frequency to a variable frequency signal pulse. When a second-order non-linear crystal is excited with the pump frequency $\omega_{P,}$ electrons in the crystal molecules leave their ground state to populate the higher excited state energy and when these excited molecules return to their ground state, two-photon with frequencies $\omega_{S,}$ called the signal and ω_I called the idler, are emitted.

During this transition, a fraction of the pump beam's energy is transferred to the signal beam resulting in the amplification of the signal beam. The process is analogous to stimulated emission, as the amplified signal retains the coherent properties of the pump beam. Thus, three beams are obtained at the output of the non-linear crystal: an amplified signal beam, a newly formed idler beam and a residual pump beam.

A light source from an external laser amplifier is used to pump the OPA. The laser pulse is split into two parts: a high-intensity beam is used as a pump pulse and the other low intensity beam is used to generate a broadband signal, also called a seed pulse. The seed broadband pulse is generated using the white light generation (WLG) process using a transparent dielectric medium, such as a sapphire crystal having third-order nonlinearity, which results in the broadening of the pulse. The pump and seed pulse are then focused on an OPA crystal, such as beta barium borate, or BBO, crystal. Efficient parametric amplification occurs when photon energy conservation and wave-vector phase matching conditions are satisfied.

$$\omega_P = \omega_S + \omega_I$$

$$\overrightarrow{\Delta \mathrm{k}} = \overrightarrow{\mathrm{k}_P} - \overrightarrow{\mathrm{k}_S} - \overrightarrow{\mathrm{k}_I} = 0$$

Where $\overrightarrow{\mathrm{k}_P}$, $\overrightarrow{\mathrm{k}_S}$ and $\overrightarrow{\mathrm{k}_I}$ are the wave vector of the interacting beam of the pump, seed and idler. The narrow pulse of desired frequency is achieved by changing the angle between the interacting wave vector and the optical axis of the OPA crystal. This is done by rotating the crystal and in this way a different ratio of $\overrightarrow{\mathrm{k}_S}$ to $\overrightarrow{\mathrm{k}_I}$ is created, which corresponds to a different color of the generated light [43].

2.3 Transient absorption spectroscopy

Transient absorption(TA) spectroscopy is a non-linear optical technique used to study the evolution of photogenerated excited chromophore dynamics occurring at ultrafast time scales, i.e., from a few femtoseconds to millisecond time scales [36]. TA spectroscopy is a suitable method to study and characterize the lifetime related to excited state singlet and triplet dynamics, photoinduced energy or electron transfer, fluorescence, intersystem crossing, photochemical reaction products, and other various photophysical mechanisms [44,45]. TA spectroscopy is based on the pump-probe method, where a small fraction of molecules is excited to a higher electronic state with the very intense laser pulse

called the pump and a weak white light continuum called the probe pulse is sent through the sample with a small-time delay (Δt) to probe the pump induced changes in the sample as shown in Figure 2.5. A difference in absorption is measured by subtracting the unexcited sample's absorption from the excited sample's absorption. By measuring difference in absorption (ΔA) at different delay times with respect to pump and probe, TA spectra are obtained, which contain information regarding the dynamic response of the system under study. The TA spectra generally have a contribution from various processes such as ground state bleach (GSA), excited state absorption (EAS), stimulated emission (SE) and absorption of photochemical products in case a photoinduced reaction takes place in the sample.

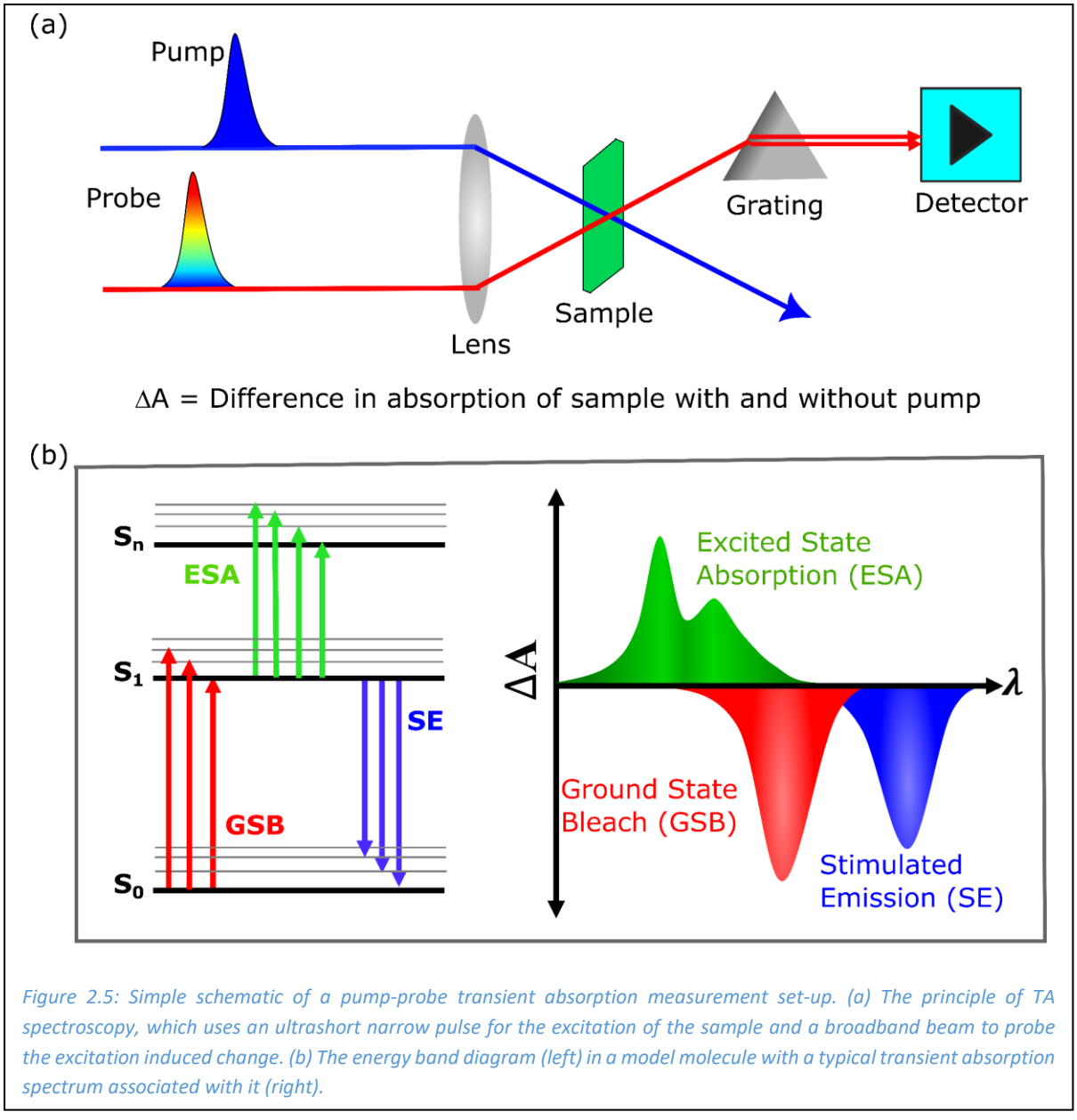

Figure 2.5: Simple schematic of a pump-probe transient absorption measurement set-up. (a) The principle of TA spectroscopy, which uses an ultrashort narrow pulse for the excitation of the sample and a broadband beam to probe the excitation induced change. (b) The energy band diagram (left) in a model molecule with a typical transient absorption spectrum associated with it (right).

Ground state bleach: Ground state bleach occurs as a negative contribution in the TA

spectrum as the fraction of molecules that is excited by the pump pulse decreases the number of molecules present in the ground state of the sample. Due to this, the ground state absorption of an excited sample measured by probe pulse is less than from the unexcited sample, which gives a negative value in the ΔA spectrum [46].

Excited state absorption: After the pump excitation of the sample, some of the molecules present in an electronic excited state can gain enough energy and undergo an optical transition to a higher excited state of the chromophore. Absorption of the probe pulse takes place at that wavelength which contributes as a positive absorption signal in the ΔA spectrum. Moreover, the excited state population remains unaffected due to the weak intensity of the probe signal.

Stimulated emission: Stimulated emission can be described using a two-level system. For a two-level system, Einstein's absorption coefficient from the ground state to excited state B_{12} is identical to Einstein's emission coefficient from the excited state to ground B_{21}. When the probe pulse passes through the excited volume having energy equivalent to the emission energy, it induces another photon from the excited state to the ground state in the form of stimulated emission. The emitted photon has the same energy and direction as the probe, increasing the intensity of probe light; consequently, it contributes as a negative signal to the ΔA absorption. Stimulated emission occurs only for optically allowed transitions and is physically equivalent to the fluorescence spectrum of the chromophore, thus it is Stoke shifted relative to the ground state bleach.

Photochemical product absorption: After the excitation of the sample with the pump pulse, the excited molecules can become redox-active and trigger photochemical reactions, resulting in the formation of transient states such as charge-separated states and isomerized states. These transient species absorb the probe light and contribute positively to the TA spectrum.

2.3.1 Transient absorption setup

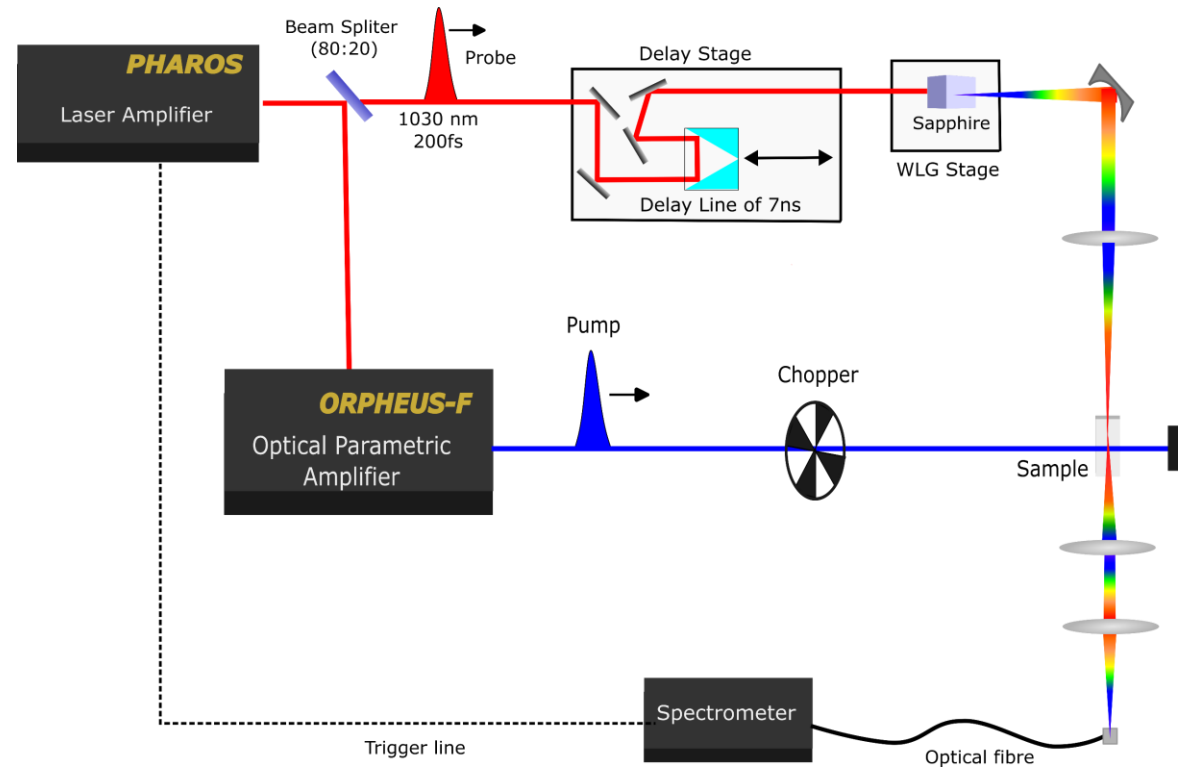

Figure 2.6: Transient Absorption setup used in a fs-TA measurement. The output of the Nd:YAG laser (1030 nm, 200 fs) amplifier is spilt into pump and probe. The different pump wavelength is tuned using an optical parametric amplifier. A delay stage is used to introduce the time delay between pump and probe. The probe beam is converted into a white light continuum using a sapphire crystal.

The laser setup used to perform the fs-TA measurement is depicted in Figure 2.6 The laser pulse generated by a regenerative amplifier (Pharos, Light Conversion) has a fundamental wavelength of 1030 nm, 1 kHz repetition rate and the 200-fs pulse is split into two pathways with an 80:20 beam splitter. The majority of the fundamental (80%) is directed to the optical parametric amplifier (Orpheus-F, Light Conversion) where the beam is spectrally broadened and tuned to desired monochromatic wavelength to generate the pump beam, which will used to photoexcite the sample. The remaining 20% of the fundamental is directed to an optical delay stage consisting of several sets of mirrors mounted on a computer-controlled motorized translational stage to generate the probe beam. The function of an optical delay stage is to introduce a controlled time delay between the pump and probe pulses. Depending upon the translation movement of the delay line, a time delay of up to 7 ns is generated between the pump and probe beams. Furthermore, the probe beam path is sent through a white-light generation stage (WLG stage), where the beam is focused onto a non-linear crystal

such as sapphire, calcium fluoride or quartz to create spectrally broad white light continuum. The intensity of the white light continuum is kept very small to avoid excitation from the probe beam. It is then focused on the sample, which is generally a cuvette or transparent film sample on a quartz substrate. The pump excitation beam generated by OPA is also sent through several neutral density filters to control the pulse's intensity. Moreover, the pump's polarization is set at 54.7^{o} with respect to the probe to eliminate polarization-related effects. Both the pump and probe beam are collimated and spectrally overlap with each other at the sample. After both beams have passed through the sample, the pump is blocked and the probe beam is directed towards the spectrograph, where it is dispersed spectrally on the detector array customized to measure the absorption spectrum with each pulse train.

2.3.2 Data analysis:

Collection of TA data: During the TA experiment, the time delay between pump and probe is kept fixed while the pump beam is sent through a mechanical chopper rotating at a 500 Hz repetition rate before focusing on the sample. Due to this, every second pump excitation is blocked with respect to probe rep rate. Thus, the probe pulse alternatively observes excited and non-excited samples; consequently, the detector measures the intensity of "pumped" and "unpumped" signals. Several numbers of shots are measured until the signal-to-noise ratio reaches an acceptable value. The ΔA spectrum is constructed using the average intensity of "pumped" and "unpumped" signals as

$$\Delta A = -\frac{\log(I(\lambda)_{Pumped})}{\log(I(\lambda)_{Unpumped})}$$

After this step, the delay line is moved to create different time delays between the pump and probe and the entire procedure is repeated. The absorption difference is also measured before the time zero (the moment of time at which the sample experiences the first perturbation which initiates the transient response) to account for the baseline and several spectra are measured at zero-time delay to account for the instrument response function. For the data presented in this thesis, approximately 300-500 time points are collected between -

5 ps to 8 ns and the measurement is averaged over 2-3 procedures to produce a reliable data set [47].

Analysis of TA data: TA experimental data collection techniques induce several coherent artifacts, which should be corrected before any data analysis. The broadband probe pulse consists of several wavelengths and when it passes through the cuvette or quartz sample, the wavelength is separated due to group velocity dispersion. The blue wavelength reaches the detector earlier than the red, which creates the wavelength-dependent time zero shift between the coherent signals in the raw TA data. To do the time-zero correction, coherent artifacts between the pump and probe are measured using the solvent without any contribution from the signal sample. These artifacts occur within the sub-picosecond time scale between 0-10 ps. The coherent artifact is fitted for each detected wavelength to extract the corresponding time zero and finally, time zero for each wavelength is plotted verse wavelength and fitted with the fourth order of polynomial function, which is used to correct the shift of time in the raw data from the signal. Similarly, baseline correction eliminates the background noise from the raw TA data signal. The average value of all the data points is calculated for the time before the time zero and subtracted from the TA absorption matrix.

In a typical transient absorption experiment, thousands of data points are collected, and a 2D contour of $\Delta(\lambda,\tau)$ as a function of wavelength and time is obtained. The initial analysis can be done by tracing the evolution of a single wavelength in time or by plotting the signal at a different wavelength of a fixed time. This process gives the first glimpse of the TA data at different wavelengths and times. Global and target analysis is employed to fit the entire dataset simultaneously at different times and wavelengths to extract useful components and spectra.

2.4 Global analysis

Global analysis of the TA data is in this thesis done using the R-package TIMP software with the graphical interface Glotaran 1.5.1 [48,49]. Global analysis is a method where all the wavelengths are analyzed simultaneously to a set of common time constants representing a sum of exponential decays. We interpreted our results using both sequentially interconverting and parallel decaying sum-of-exponential models. The sequential model leads to the generation of multiple evolution-associated difference spectra (EADS), which

transform into subsequent EADS characterized by mono-exponential decay rates. Each EADS represents the spectral changes associated with each kinetic component as it decays over time. This method quantitatively describes the system's evolution of excited and intermediate states involved. The spectral lineshape of EADS does not always reflect the pure electronic state of the species involved and can be the mixture of spectra arising from the ground state, excited state, or photoinduced intermediate species involved. It can also give information regarding the intermediate photophysical species. The parallel sum-of-exponential model produces decay-associated difference spectra (DADS). The DADS represents the spectral changes related to the specific time constant and is equivalent to spectral change occurring during the evolution of one EADS to another. This model is useful when several photophysical processes compete and proceed simultaneously. The global analysis scheme evaluates EADS and DADS simultaneously. Since both methods are mathematically equal, the same time constant applies to both EADS and DADS.

2.5 Time-resolved photoluminescence spectroscopy

Time-resolved photoluminescence (TRPL) measurement is a powerful technique used to study time-dependent behavior photoluminescence emission of emissive materials, including organic chromophores. It provides valuable information about the lifetime of excited states and the dynamics of energy transfer processes in materials. Fluorescence (or phosphorescence) emission is one of the pathways in which excited molecules lose their energy and relax to the ground state. In steady-state fluorescence emission, the sample is continuously illuminated thereby resulting in a condition where the excitation and emission processes reaches equilibrium, and the observed signals remain constant over time. The steady-state measurement doesn't provide any information regarding the dynamics of molecules in the excited state and how exactly the excited molecules relax to the ground state [50]. Time-resolved photoluminescence spectroscopic techniques are used to extract the rate of light emission from transient signals relaxing from the excited state of chromophores, thus provides information regarding the relaxation dynamics of the emissive state. These processes may involve radiative relaxation of fluorescence, phosphorescence, intersystem crossing, non-radiative relaxation, excitation energy transfer and photoinduced

charge transfer reactions. All these processes can affect the excited state of molecules and hence they can be probed by measuring the fluorescence in time.

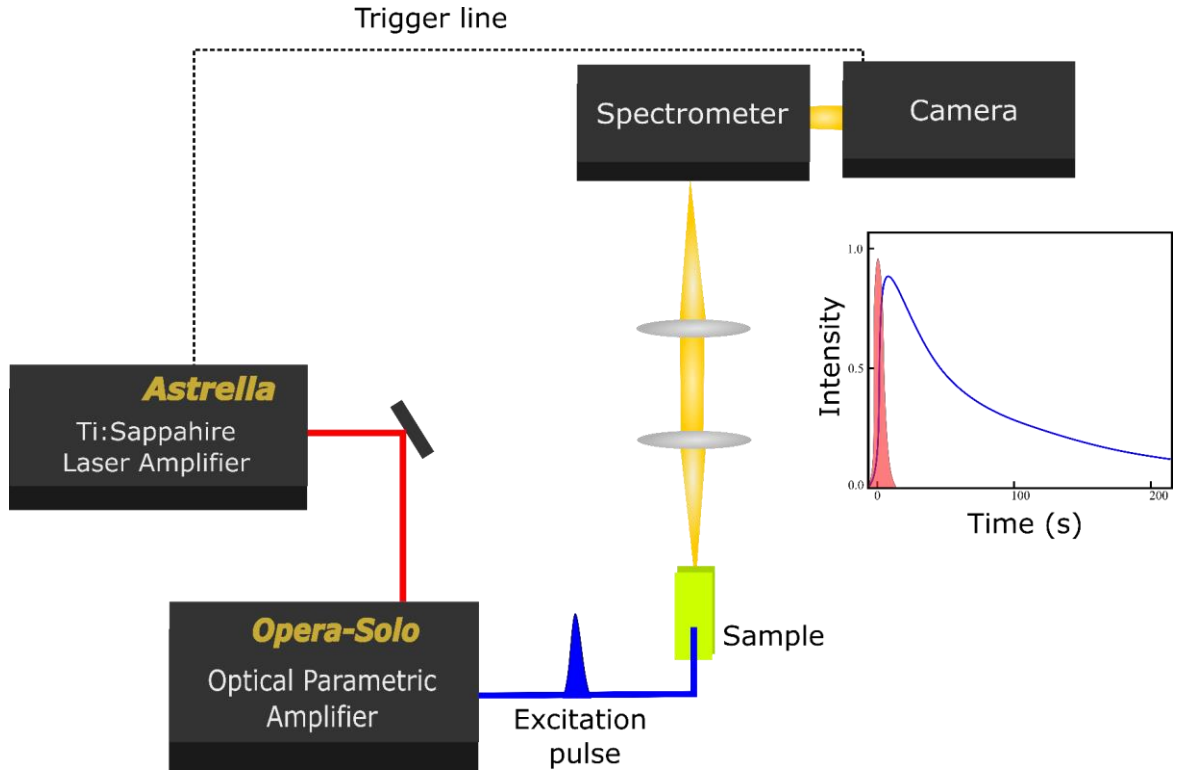

Figure 2.7: Time resolved fluorescence experimental setup consists of a Ti: Sapphire laser amplifier with an output at 800 nm with a 35 fs pulse width, which is fed to the optical parametric amplifier to tune the wavelength of the excitation pulse. The excitation light is focused to the sample and the emitted light is then collected using a pair of lenses after which it is focused into a spectrometer coupled with the camera to image the fluorescence of the sample.

2.5.1 Experimental setup

The experimental setup to measure time-resolved fluorescence can be divided into an excitation part and a detection part. The laser pulse generated by a Ti:Sapphire regenerative amplifier (Coherent, Astrella) was used for the excitation part. The laser output has a fundamental wavelength of 800 nm, 1 kHz repetition rate and a 35 fs pulse width with 3.5 mJ pulse energy. The laser output is fed into an optical parametric amplifier (Coherent, Opera solo). In the OPA, a different color wavelength is generated depending on the excitation energy required by the sample. The pump excitation beam generated by the OPA is then focused to excite the sample. The light emitted by the sample is collected using a pair of lenses and directed to the detection camera via a spectrograph. For the TRPL measurement, two different kinds of cameras are used: streak camera and gated-iCCD camera, based on the nature of measurement required.

2.5.2 Streak camera

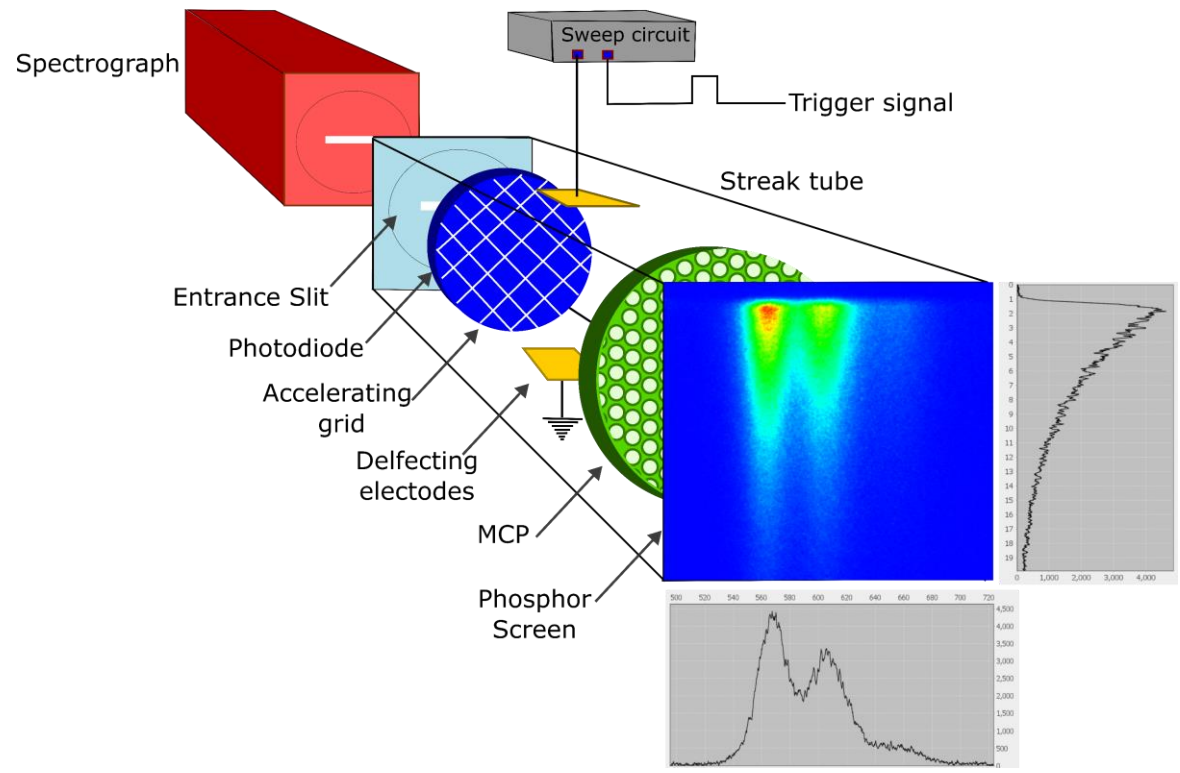

Figure 2.8: Schematic of the working principle of the Streak camera.

The streak camera is one of the ultrahigh-speed detectors used in TRPL to capture the transient fluorescence image over an ultrashort interval. The working principle of the streak camera [51] can be divided into three stages, as shown in Figure 2.8. In the first stage, the spectrally-dispersed emitted photons from the spectrograph enters the streak tube and hits the photodiode, which converts the photons into a number of electrons proportional to the intensity of the incident light. These electrons are then accelerated in an electric field in the second stage and lead through the deflecting electrode. When the electrons are focused through the deflecting plates, a high-speed varying voltage ramp is applied, which sweeps the electron from top to bottom depending on their arrival time. Electrons that arrive earlier in time experience deflection at the top of the phosphor screen, while electrons arriving later hit the bottom of the screen, their position depending on the voltage ramp they encounter. At this stage, the arrival time of the electron is converted into the position of the electron beam in space. At the final stage, the electrons are passed through the microchannel plate, which multiplies the number of electrons to increase the intensity and finally, they hit the phosphor screen at the end of the streak tube, where it is converted back to an optical image.

The main advantage of the steak camera over other conventional methods like TCSPC (Time-Correlated Single Photon Counting) is that it employs deflection plates which only deflect electrons in vertical direction while leaving the other coordinates available for measurement. This unique configuration allows for the spectral analysis of light using a spectrograph. The vertical axis provides information about the timing of electron emission from the photodiode. By measuring the vertical position, the exact time when the electron left the photodiode can be determined. On the other hand, the horizontal position of the electron on the streak camera depends on its wavelength. This is achieved by employing a spectrograph before the light is focused onto the streak camera. Thus, the entire 2-dimensional spectro-temporal dynamics can be captured in a single experiment and a 2D image of the streak camera provides information on the time and wavelength of the emitted photon. The time resolution that a typical synchro-scan streak camera can reach is 1 ps and the speed of data collection is very fast, exceeding that of conventional fluorescence methods by a substantial margin. The combination of deflection plates and a spectrograph enables the streak camera to simultaneously capture temporal and spectral information which sets it apart from conventional methods like TCSPC.

2.5.3 Gated-iCCD 4picos camera

In certain materials such as TADF emitters, where the emission intensities vary significantly over time, it can be challenging to achieve a good signal-to-noise ratio, especially for the lower intensity or slower signals. Gated intensified charge-coupled device (iCCD) cameras are popularly used for measuring time-resolved fluorescence signals from materials exhibiting the TADF mechanism (see chapter 4-5 for more details on TADF). TADF materials have a very strong prompt emission over a few nanoseconds and a very weak delayed emission afterwards, depending on the lifetime of the material. To accurately measure the fluorescence lifetime of these materials, a time-gated measure is needed, which is done using an intensified charge-coupled camera (iCCD) [52]. After excitation of the sample, the emitted photon is focused into a spectrograph with 300 grooves/mm grating and the spectra are imaged using the iCCD detector, with a 200-picosecond gating pulse. The camera is synchronized with a Ti: Sapphire laser excitation pulse to ensure that camera captures the light emission at the exact desired time after the excitation of the sample which is crucial in

accurate determination of time zero. Time zero is when the optical pulse arrives to excite the sample. The acquisition of the image is done using computer-controlled software called 4Spec, where important parameters like time zero, time delay (time at which photon collection starts), gate width (time interval up to which photons are counted) and integration time (length in time till photon collection takes place) are set [53,54]. After accurate determination of the time-zero, the individual spectra are collected by setting the specific time delays and integration time. A kinetic decay curve is obtained by logarithmically increasing the time delay over the time window of the measurement. The main advantage of a gated iCCD camera over a streak camera is that it can independently measure the bright photons from the dark photons with high resolution.

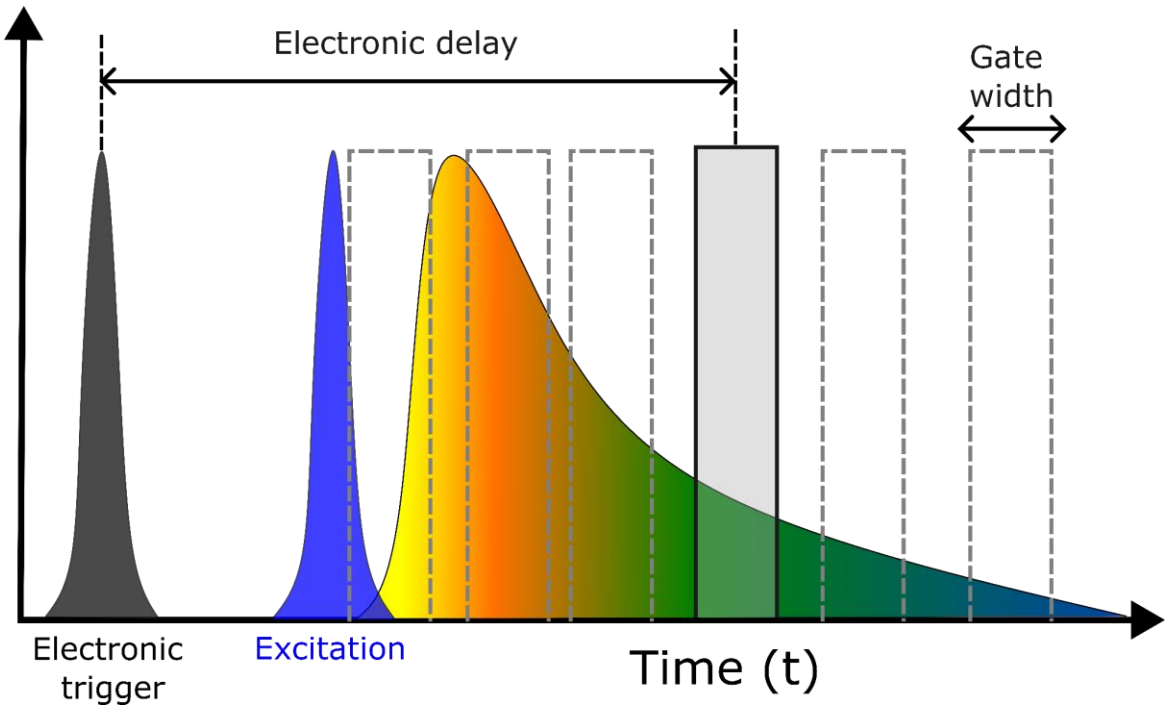

Figure 2.9: Working principle of gated-iCCD camera measurement. The fluorescence of the sample is collected in the gated time window which synchronized with laser trigger with the electronic pulse. The kinetic spectra is obtained by measuring the fluorescence with logarithmically increasing time delays and plotting intensity of fluorescence spectra with time.

Chapter 3 : Photoexcited charge separation dynamics in a conformationally flexible acceptor donor acceptor molecular foldamer.

We report the photophysical properties of a molecular foldamer system **PDI-AnEt$_2$-PDI**, where the electron-donating N,N-diethyl aniline unit is covalently linked between two electron-accepting perylene diimide (PDI) chromophores. **PDI-AnEt$_2$-PDI** is conformationally flexible, adopting either an *open* (two PDIs far apart) or *folded* (two PDIs within π-stacking distance) conformation, depending on the solvent. We characterized the photoinduced electron transfer dynamics of both *open* and *folded* forms in solvents of varying polarity. *Open* **PDI-AnEt$_2$-PDI** undergoes charge separation to **PDI$^{\bullet-}$-AnEt$_2^{\bullet+}$-PDI** in polar and non-polar solvents. However, the efficiency of charge transfer in the non-polar solvent is higher compared to the polar solvent in the open conformation. In the *folded* form, two different charge-separated species are observed. In addition to **PDI$^{\bullet-}$-AnEt$_2^{\bullet+}$-PDI**, the dominant product in the *folded* form is **PDI$^{\bullet-}$-AnEt$_2$-PDI$^{\bullet+}$** via symmetry-breaking charge transfer. The presence of both charge-separated products indicates varying degrees of interchromophoric coupling in the *folded* form. This work provides insight into how the competitive balance of photophysical pathways in structurally dynamic organic multichromophoric systems can be mediated by molecular design.

Kalyani Thakur, Saptarshi Datta, Debangshu Chaudhuri, Paul W.M Blom and Charusheela Ramanan, Competitive Charge Separation Pathways in a Flexible Folda-dimer (Manuscript Submitted)

3.1 Introduction

Molecular chromophores with efficient photoinduced energy and electron transfer processes have gained considerable interest due to their application as light harvesting systems [55] [56], in optoelectronic devices [57] [58], photonics [59], and sensing [60]. Covalently linked molecular chromophores comprising electron donor and acceptor dyads, triads, and supramolecular structures have been synthesized in order to study electron and energy transfer rates based on donor-acceptor distance, electronic coupling [61], orientation, and free energy of the reaction [62].

Perylened diimide (PDI) chromophores offer an attractive model system to study the correlation between molecular design and photophysical mechanisms. The molecular architecture of PDI based systems can be easily engineered by covalent substitution at the ortho, para, or imide position and by controlling the π-stacking between the chromophores [63–66]. These chromophores tend stack face-to-face, forming an H-type aggregate [67,68] or head-to-tail with J-type aggregation [69], depending on the sidegroup substitution on the perylene core. The strength of electronic coupling within the donor-acceptor structure can also be influenced by solvent polarity and dielectric constant of the local environment [70–72]. Thus, understanding the influence of interchromophoric electronic coupling on the photophysics of the molecular chromophores system is crucial for fabrication of photonic and electronic devices [73,74]. In the last few years, many studies have been done on the PDI based dimer systems elucidating the ultrafast relaxation of exciton into excimers [75], singlet fission [9] and triplet generation [78], charge separation [79,80], and symmetry breaking charge separation [81–83] . These studies illuminate the importance of inter-chromophoric couplings and the influence of bridging spacers on the photophysical properties.

In this study, we synthesized and characterized an acceptor-donor-acceptor triad molecular system **PDI-AnEt$_2$-PDI**, where the electron-donating N,N-diethyl aniline (AnEt$_2$) unit is covalently linked between two electron-accepting perylene diimide (PDI) chromophores. The covalent linkage between the AnEt$_2$ bridge and PDI chromophores provides conformational flexibility, allowing PDI chromophores to freely rotate around the bridging donor. Thus, **PDI-AnEt$_2$-PDI** forms two stable conformations viz. *open* **PDI-AnEt$_2$-PDI**, where PDI chromophores

are far apart from each other and *folded* **$AnEt_2$-PDI_2**, where the PDI chromophores fold towards the bridging donor within π-stacking distance, yielding H-aggregated foldamers. These two conformations have different electronic coupling character, which strongly influences the photophysical processes. This paper reports the difference in photoinduced electron transfer pathways in the *open* and *folded* configuration as a function of electronic coupling between two conformers and how these properties depend on solvent polarity [84]. We used transient absorption and time-resolved photoluminescence spectroscopies to elucidate the ultrafast photophysical properties. We observed that the electron transfer between the PDI acceptor and $AnEt_2$ donor bridge occurs independently of solvent polarity; however, the charge transfer efficiency in *open* **PDI-$AnEt_2$-PDI** is different in solvents of varying polarity. In *folded* **$AnEt_2$-PDI_2**, two different charge-separated species are detected. In addition to the formation of **$PDI^{\bullet-}$-$AnEt_2^{\bullet+}$-PDI**, the dominant mechanism is symmetry-breaking charge transfer between the two PDI chromophores to yield **$PDI^{\bullet-}$-$AnEt_2$-$PDI^{\bullet+}$**. This contrasts with other PDI foldamers, where excimer formation is observed as the dominant product [68,72]. These results demonstrate how molecular conformation and interchromophoric coupling can mediate the balance between competitive photophysical pathways in structurally dynamic organic chromophore systems.

3.2 Results and discussion

Solvent-dependent molecular conformation

Figure 3.1 shows the steady-state absorption spectra of **PDI-$AnEt_2$-PDI** in six different solvents with varying solvent polarity and dielectric constant. The absorption spectra of PDI monomer (see Figure 3.1 for chemical structure) in grey consists of three vibronic peaks associated with 0-0, 0-1, and 0-2 transitions at 530 nm, 490 nm, and 460 nm [1]. Figure 3.1b shows the steady-state absorption of **PDI-$AnEt_2$-PDI** in chloroform, dioxane and toluene. The absorption spectra in these three solvents are similar to the reference monomer, suggesting that the system is in the *open* **PDI-$AnEt_2$-PDI** form. The foldamer adopts the *folded* **$AnEt_2$-PDI_2** in DMSO, acetone, and cyclohexane, evidenced by the steady-state absorption spectra, which show a striking difference

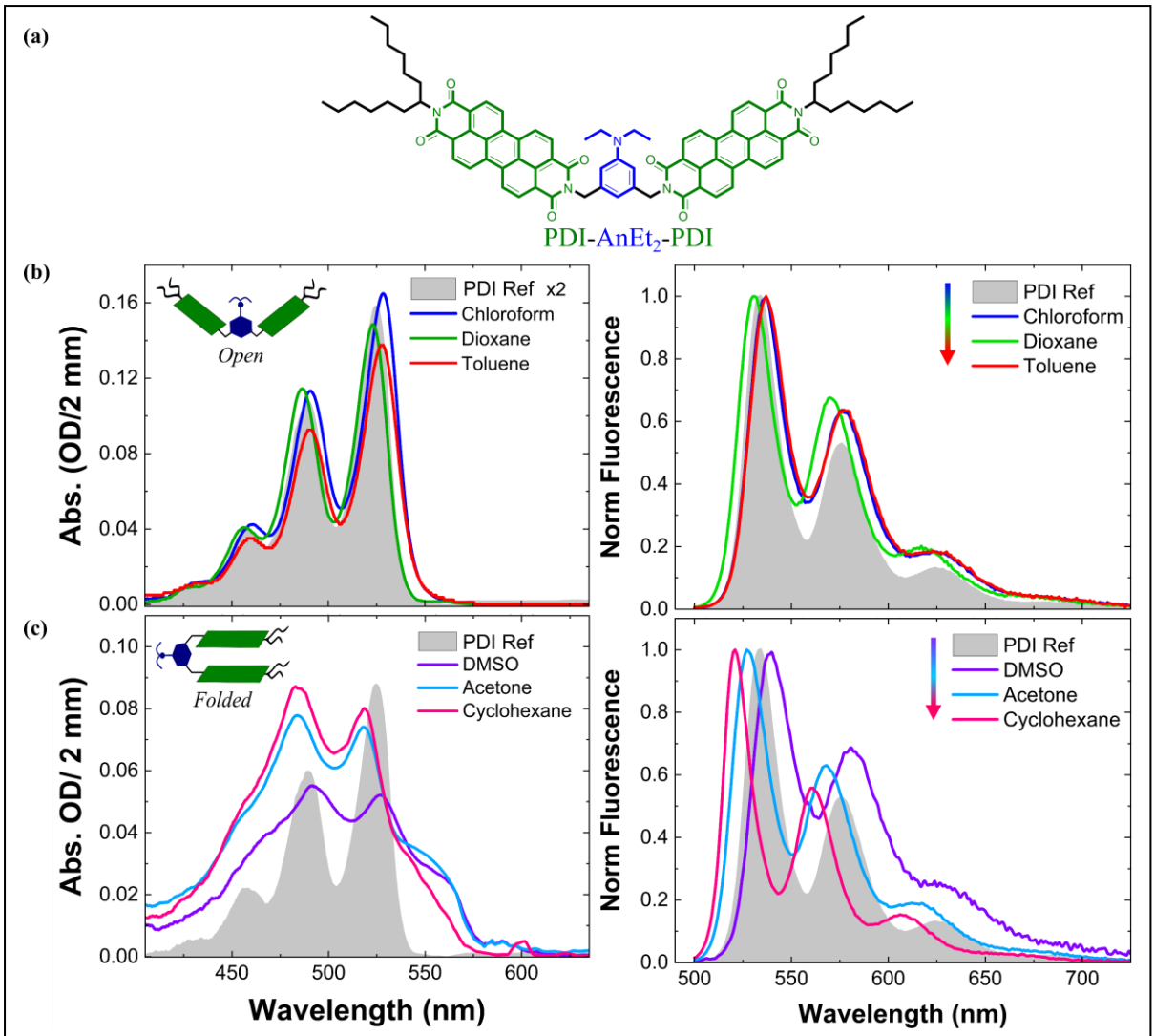

Figure 3.1: (a) Chemical structure of acceptor-donor-acceptor PDI-AnEt$_2$-PDI. (b) Steady-state absorption (left) and fluorescence (right) of PDI-AnEt$_2$-PDI in the open form in three different solvents with decreasing solvent polarity. (c). Steady-state absorption (left) and fluorescence (right) of PDI-AnEt$_2$-PDI in the folded form in three different solvents with decreasing solvent polarity. Absorbance in OD is measured at same concentration (6 uM) of all the solutions and measured in a cuvette of 2 mm path length. The arrow indicates decreasing solvent polarity, starting from blue (and violet) with highest to red (and pink) being the least polar solvent.

from the monomeric features (Figure 3.1c). The aforementioned three characteristic peaks are blue-shifted and exhibit different oscillator strengths compared to monomer spectra. There is also a pronounced increase in the 0-1/0-0 peak ratios. These changes are consistent with the presence of H-aggregated PDI, wherein the respective transition dipoles of the molecules are symmetrically aligned. [86–88]. The two PDI acceptor chromophores fold towards each other around the anchor point of the bridging donor $AnEt_2$ and equilibrate within π-stacking distance, forming the *folded* form. The trends observed are consistent with previously reported binding energies for PDI π-stacking (Table 3.1). Chloroform, dioxane, and

toluene all exhibit similar stacking association constants (~-15 kJ/mol) and all correspond to the *open* form. The stacking energies for DMSO, acetone, and cyclohexane are all more negative (-17 - -30 kJ/mol), which is consistent with the observation of a *folded* conformation in these solvents.

The steady-state fluorescence spectra exhibit mirror-image symmetry with the absorption spectra, with three characteristic peaks between 540 nm and 620 nm, as documented for monomeric PDI [89]. In the case of *open* form, the fluorescence spectra of dioxane are slightly blue-shifted to PDI monomer while chloroform and toluene lie on top of each other. In *folded* form, despite the evidence of H-aggregation in the absorption spectra of DMSO, acetone, and cyclohexane, the fluorescence spectra exhibit lineshapes similar to PDI monomer. However, H-aggregated PDI is expected to show a broad featureless excimer emission peak, red-shifted relative to the monomer [69]. The fluorescence spectra of the *folded* form suggests that it contains some degree of unfolded conformation. Furthermore, we see a relative increase in the intensity of the lower energy peaks, most strikingly for DMSO. This is consistent with the presence of an underlying excimer peak contributing to the fluorescence lineshape. The enhanced Stokes shift in the *folded* form fluorescence spectra can be explained by the stabilization of the excimer peak with the polarity of the solvent, suggesting some charge-transfer (CT) character in the H-aggregated exciton [90].

Fluorescence quantum yield increases upon protonation:

The foldamer system is designed to undergo photoinduced charge separation between the electron-donating $AnEt_2$ bridge and one of the electron-accepting PDI moieties. A protonation experiment is carried out to confirm this hypothesis by measuring the change in fluorescence quantum yield by the addition of hydrochloric acid (HCl). In the foldamer sample on its own, photoinduced charge separation would partially quench the fluorescence pathway, and therefore limiting the fluorescence quantum yield. The addition of acid protonates the $AnEt_2$ donor, blocking the charge separation pathway, thus increasing the fluorescence quantum yield. Figure 3.2b shows the steady-state fluorescence spectra of **PDI-$AnEt_2$-PDI** in dioxane with the increasing molar equivalents of HCl. Dioxane is chosen for this measurement as it has good miscibility with the aqueous HCl solution compared to chloroform or toluene. The absolute fluorescence intensity increases with each acid addition step and saturates at four times the original intensity upon the addition of 10 mol. equivalent of acid.

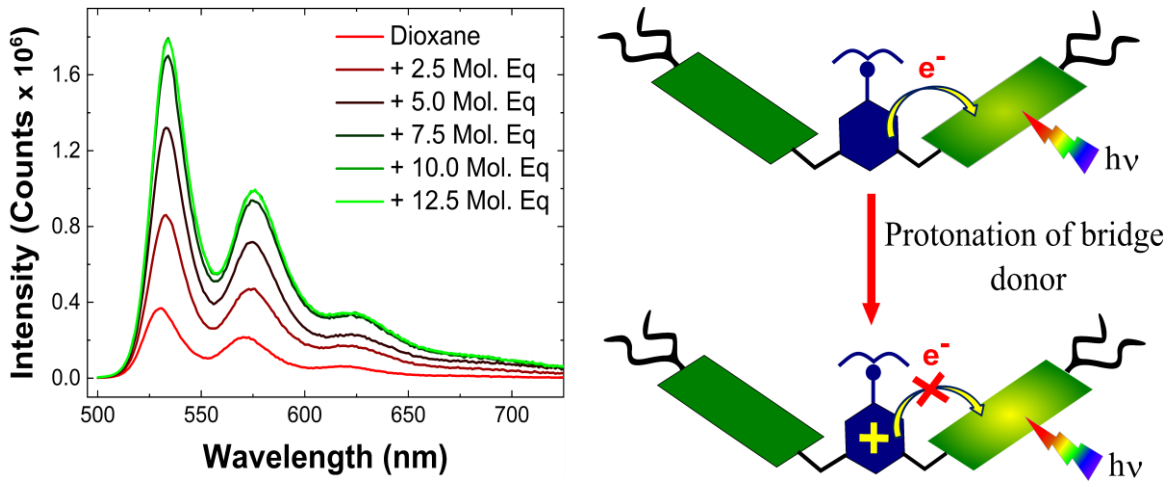

Figure 3.2: Fluorescence spectra (λ_{ex} = 480 nm) of PDI-AnEt$_2$-PDI in dioxane with increasing concentration of HCl acid, the spectra in red represents non-protonated emission spectra while the spectra in green represents the saturated emission at 10 molar equivalents of HCl acid. The cartoon in the right shows the proposed photoinduced charge transfer mechanism with the protonation of bridging donor with and without the presences of acid.

This observation is consistent with the proposed charge separation with the AnEt$_2$ bridge. Upon photoexcitation of **PDI-AnEt$_2$-PDI**, one of the PDI molecules undergoes a charge transfer reaction with the bridging donor and quenches the PDI fluorescence, as shown in the scheme in Figure 3.2. The addition of acid protonates the diethylaniline donor moeity, blocking the electron transfer pathway between the PDI acceptor and bridge donor. Consequently, the PDI acceptor chromophore relaxes via fluorescence emission, resulting in enhanced quantum yield. These results are consistent with the presence of photoinduced charge separation in the non-protonated **PDI-AnEt$_2$-PDI**. However, other relaxation processes, such as excimer formation, could also lead to fluorescence quenching, and further characterization is needed to clarify the photoexcited mechanisms.

Theoretically Favorable Energetics for Charge Separation

To confirm the feasibility of photoinduced charge transfer to form **PDI$^{\bullet-}$-AnEt$_2^{\bullet+}$-PDI**, the thermodynamic driving force is calculated using the Rehm-Weller equation [31].

$$\Delta G_{IP} = e[E_{ox}(D) - E_{red}(A)] - E_{00} \quad (26)$$

$$\Delta G_{CS} = \Delta G_{IP} + C + S \quad (27)$$

$$\Delta G_{CR} = -\Delta G_{IP} \quad (28)$$

$$C = \frac{-e^2}{4\pi\varepsilon_0 r_{DA}\varepsilon_s} \quad (29)$$

$$S = \frac{e^2}{4\pi\varepsilon_0}\left(\frac{1}{2r_D} + \frac{1}{2r_A}\right)\left(\frac{1}{\varepsilon_S} - \frac{1}{\varepsilon_{SP}}\right) \quad (30)$$

Table 3.1 Optimised distance between donor and acceptor for open and folded form.

Solvent	Energy (eV)	$r_{AnEt2-PBI}$ (Å)	$r_{PBI-PBI}$ (Å)
Chloroform (open)	-90893.378871249	9.432215	16.695905
1,4-Dioxane (open)	-90893.133424566	9.431955	16.688675
Toluene (open)	-90893.161588348	9.432025	16.689960
DMSO (folded)	-90894.848857423	9.429075	3.631780
Acetone (folded)	-90894.791332560	9.423320	3.633110
Cyclohexane (folded)	-90894.205008866	9.414075	3.687045

Where E_{ox} and E_{red} are half-wave oxidation and reduction potential of donor and acceptor, respectively, and taken from cyclic voltammetry measurements. The reduction potential of folded form taken is taken as -0.47 V [91], E_{00} is the energy of the lowest excited state of acceptor chromophore estimated by the intersection of normalized absorption and fluorescence spectra, and C and S represent the coulombic interaction and solvation energy of radical cation and anion molecules. r_{DA} is the center-to-center distance between donor and acceptor and is approximated to be 9.3 Å based on the geometry-optimized structure of PDI-AnEt$_2$-PDI obtained from DFT (Table 3.1) r_D and r_A are cationic and anionic radii. We used a literature value of 7.4 Å for the PDI anionic radius [92]. For the cationic radius of AnEt$_2$, we used 3.05 Å based on the value reported for dimethylaniline, which has a similar structure [93]. The symbols ε_S and ε_{SP} represent the dielectric permittivity of the solvent used in the photochemical and electrochemical studies. The calculated results are summarized in Table 3.2.

The change in the free energy for charge separation ΔG_{CS} is negative for all the solvents with both *open* and *folded* configurations, indicating that photoinduced charge separation between the $AnEt_2$ donor and photoexcited PDI acceptor is thermodynamically favorable. Moreover, we notice that ΔG_{CS} is more negative with increasing solvent polarity, owing to a more stabilized charge-separated state in the polar solvent. [94,95]

Table 3. 2 Driving force of charge separation and charge recombination with their respective reorganization energy for open and folded conformation.

	Solvent	Dielectric constant	Polarity	E_{00} (eV)	ΔG_{CS} (eV)	ΔG_{CR} (eV)
Open **PDI-AnEt$_2$-PDI**	Chloroform	4.81	0.259	2.33	-1.07	-1.26
	Dioxane	2.25	0.164	2.35	-0.67	-1.68
	Toluene	2.83	0.099	2.33	-0.82	-1.52
Folded **AnEt$_2$-PDI$_2$**	DMSO	46.61	0.444	2.31	-1.27	-1.04
	Acetone	20.7	0.355	2.37	-1.27	-1.09
	Cyclohexane	2.02	0.006	2.39	-0.49	-1.9

Solvent-dependent photophysical dynamics.

Transient absorption (TA) spectroscopy measurements were used to elucidate the charge transfer dynamics and pathways in both *open* and *folded* forms. For *open* **PDI-AnEt$_2$-PDI**, the samples were photoexcited at λ_{ex} = 530 nm to selectively excite one of the PDI molecules in the ADA system. In the *folded* form, λ_{ex} = 490 nm is used to maximize the signal-to-noise and minimize scattering. We note that the dynamics for the *folded* form do not change if 530 nm excitation is used.

Open form exhibits charge separation between bridging donor and PDI

The TA spectra of *open* form are compared with the reference measurement of PDI monomer in chloroform (Figure 3.3). PDI monomer shows ground state bleach (GSB) at 490 nm and 530 nm and stimulated emission (SE) at 580 nm and 620 nm, consistent with the steady-state

absorption and fluorescence spectra (Figure 3.1). The positive peak at 705 nm with a broad lineshape extending to 900 nm is assigned to the excited state absorption (ESA) of the PDI singlet (PDI^{1*}). Transient kinetics monitored at 705 nm and 580 nm are well-fitted to a mono-exponential decay with a time constant of 3.8 ns, consistent with the documented excited state lifetime for PDI monomer [96].

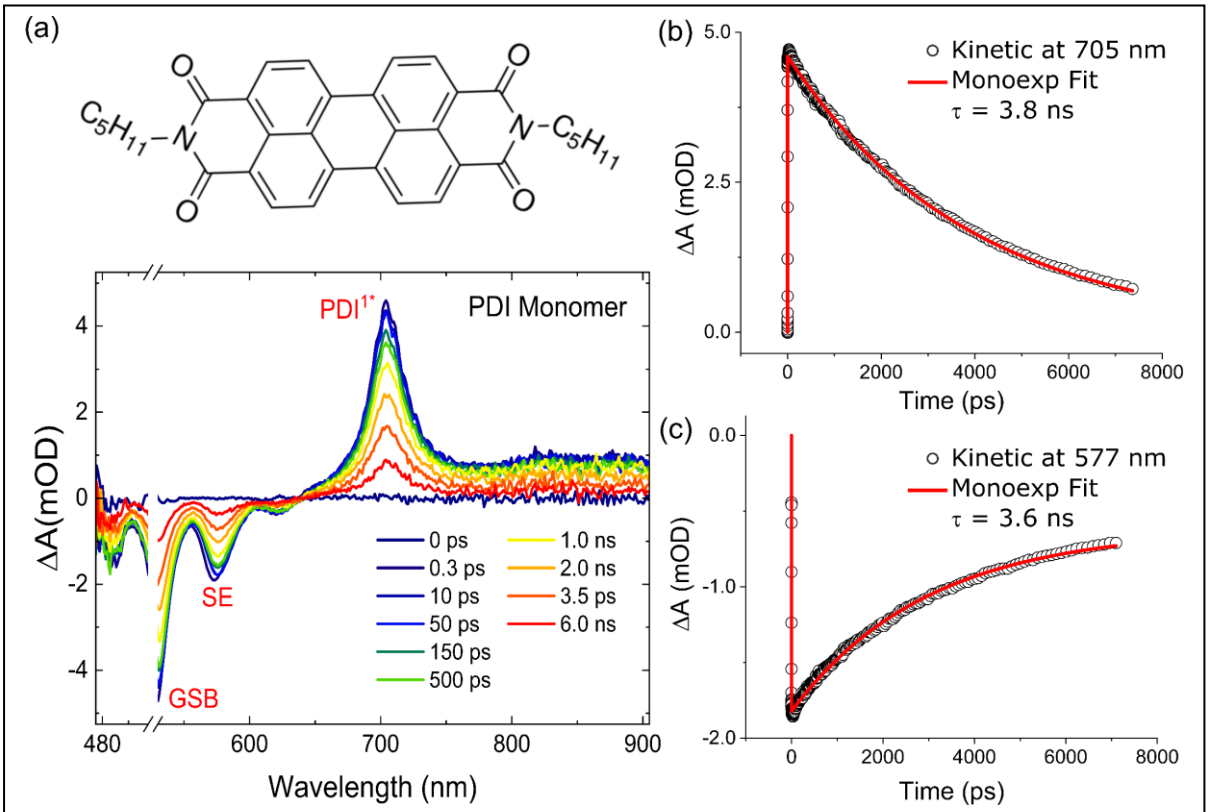

Figure 3.3: (a) TA measurement of ref PDI monomer in chloroform at 530 nm excitation in a 2mm cuvette. Top right picture shows the chemical structure of PDI monomer used as reference in this study. (b) Kinetic decay of excited state spectra at 705 nm in open black circle with its monoexponential fitting in red. (c) Kinetic decay of stimulated emission at 577 nm in open black circle with its monoexponential decay fit in red.

Figure 3.4a-c shows spectral traces at selected delay times after photoexcitation of *open* **PDI-AnEt$_2$-PDI** in toluene, dioxane, and chloroform. The TA spectra of *open* **PDI-AnEt$_2$-PDI** in toluene and dioxane (Figure 3.4a, b) show similar GSB and SE features as the monomer. Within the first 2 ps, the spectra exhibit a strong quenching of SE along with a concomitant formation of positive peaks at 702 nm and 794 nm in the case of toluene and 699 nm and 791 nm in the case of dioxane. The peak around 700 nm and 790 nm is a characteristic feature of the PDI anion absorption [97,98]. This observation confirms photoinduced charge separation in both toluene and dioxane. However, relative to toluene, the SE of **PDI-AnEt$_2$-PDI** in dioxane exhibits less quenching

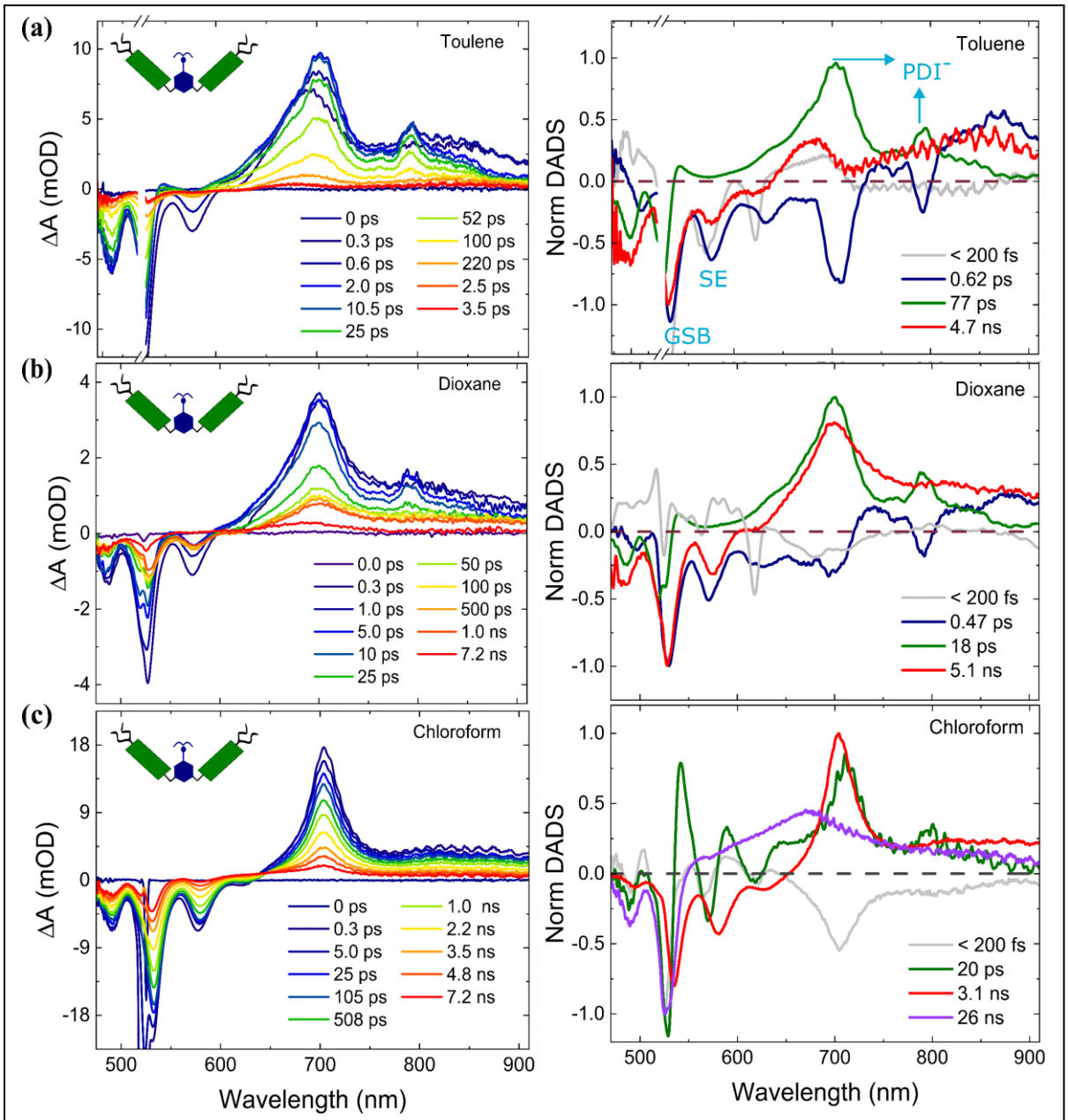

Figure 3.4: (a)-(c) TA measurement of PDI-AnEt$_2$-PDI in open form in solvent toluene, dioxane and chloroform. Corresponding figure to the right of (a)-(c) respective DADS of open form obtained by global fitting using Glotaran software using a seuenetial model. The measurement is performed at 530 nm excitation (100 nJ energy per pulse) in the 6 μM concentration of solution at room temperature in 2 mm path length cuvette.

In the case of chloroform (Figure 3.4c), there is no visible quenching of SE in the TA spectra, and the ESA appears to exhibit a similar peak as in the PDI monomer. However, the evolution of the 705 nm peak spectral lineshape in chloroform is different from the reference PDI monomer. The reference PDI monomer retains the same lineshape throughout the 7 ns experiment window. However, in *open* **PDI-AnEt$_2$-PDI** in chloroform, the ESA transforms from a narrow peak at earlier times to a broad peak at 7.2 ns. This indicates the formation of

excimer-like features [99]. Furthermore, despite the absence of SE quenching in the TA spectra, *open* **PDI-AnEt2-PDI** in chloroform does exhibit different photophysical dynamics than the reference monomer. However, we observe a counter-intuitive trend of the charge transfer process in the *open* form: we see clear evidence of the charge separation in the least polar toluene and also in the intermediately polar dioxane (though with less efficiency), whereas a long-living excimer like feature is seen in the most polar chloroform environment.

The TA measurements are further analyzed by a global fitting procedure to distinctly quantify the rate of different processes occurring in our system. The TA data for the open form in toluene, dioxane, and chloroform are all fitted with a four kinetic component model, and the associated decay-associated difference spectra (DADS) are shown to the right of the spectral traces in Figure 3.4. The global fits for toluene and dioxane exhibit similar trends. The first component, DADS1 (light grey), is required for the fit. This trace decays faster than our 200 fs instrument response (IRF) and is attributed to a coherent artifact in all cases. After the IRF, the TA spectra exhibit a lineshape described by DADS2 (blue) spectra, which has the spectral feature of ground-state bleach and stimulated emission of PDI in the spectral range 470 nm to 650 nm. This blue trace decays in 0.62 ps ($DADS2_{toluene}$) and 0.45 ps ($DADS2_{dioxane}$) to the third DADS3 (green). Here we see an ESA with peaks at 702 nm and 794 nm and no SE contribution. After 77 ps ($DADS3_{toluene}$) and 18 ps ($DADS3_{dioxane}$), this trace evolves into the last (red) DADS4, wherein the line shape features reproduce the PDI excited state decay spectra. This decays in ~5 ns in both toluene and dioxane. The similar spectral lineshape trends allow us to assign that in both toluene and dioxane, the time constant associated with DADS2 corresponds to the charge separation process, and the time constant associated with DADS3 corresponds to the charge recombination. DADS4 represents a competing PDI singlet excited state relaxation, suggesting that charge separation is competitive pathway.

In the case of chloroform, after the IRF ($DADS1_{Chloroform}$), the TA spectra lineshape described by 20 ps ($DADS2_{Chloroform}$) exhibit lineshape spectra similar to the charge separation process as observed in toluene and dioxane. After 20 ps, the trace evolves into the red ($DADS3_{Chloroform}$), where lineshape features resemble the PDI excited state decay spectra. This

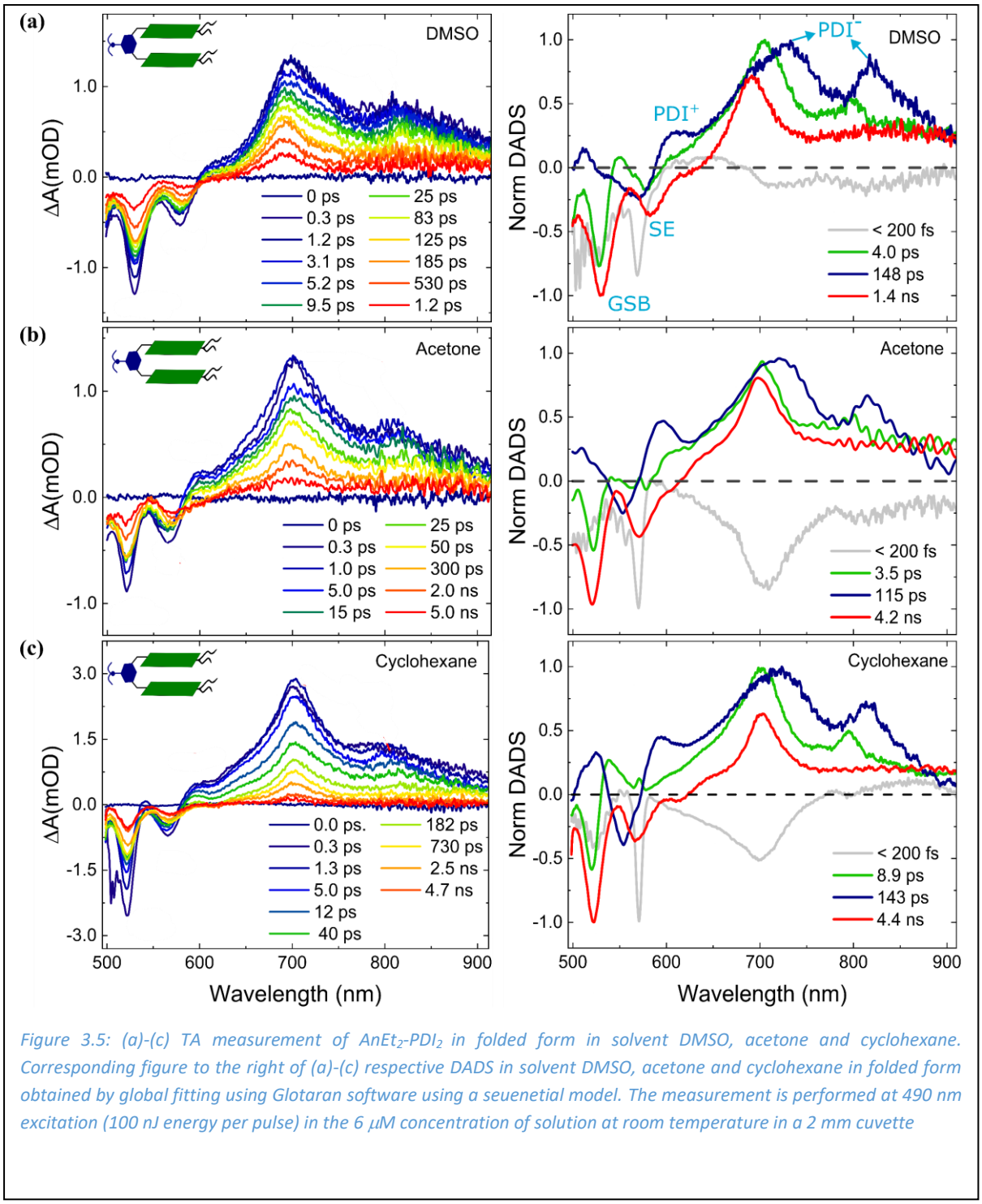

Figure 3.5: (a)-(c) TA measurement of $AnEt_2$-PDI_2 in folded form in solvent DMSO, acetone and cyclohexane. Corresponding figure to the right of (a)-(c) respective DADS in solvent DMSO, acetone and cyclohexane in folded form obtained by global fitting using Glotaran software using a seuenetial model. The measurement is performed at 490 nm excitation (100 nJ energy per pulse) in the 6 μM concentration of solution at room temperature in a 2 mm cuvette

decays in 3.1 ps and evolves into the last trace in violet ($DADS4_{Chloroform}$). This trace's lineshape feature and decay lifetime resemble the excimer formation and decay at the longer timescale of 26 ns. This suggests that **PDI-$AnEt_2$-PDI** in chloroform does undergo charge separation; however, the global fitting can't resolve the time constant of charge separation as it occurs faster than the IRF of the system. However, the charge separation process competes with the PDI relaxation and excimer formation. Due to the numerous overlapping ESA species, radical

PDI anion signature is buried underneath the TA spectra of excimer formation. However, the global analysis allows us to unambiguously identify the charge-separated photoproduct.

The observed rate constant of charge separation and recombination dynamics in the *open* **PDI-AnEt$_2$-PDI** in toluene, dioxane, and chloroform can be described in the context of Marcus's theory. With the weakly polar solvent toluene, the fluorescence of PDI is significantly quenched with a clear signature of charge separation and charge recombination. This observation is consistent with the measurement of dioxane with medium polarity, though with lower efficiency than toluene. In highly polar chloroform, photoinduced charge separation is very fast, and PDI anion buildup competes with excited-state relaxation of ^{1*}PDI and excimer formation. Furthermore, the TA measurement in protonated dioxane (Figure 3.6) follows very similar spectroscopic features with the reappearance of excimer formation as observed in chloroform. This observation indicates that photoinduced charge transfer is more pronounced in dioxane and while addition of acid changes the solvent-solute interaction which enables excimer formation in protonated dioxane. We assume that two PDI chromophores fold after the charge separation to form excimer. The thermodynamic calculation results favor the charge separation between the bridge donor and PDI acceptor in all the solvents of varying polarity. The fact that charge separation occurs irrespective of solvent polarity suggests that the reaction is barrierless, which is possible if the rate constant lies at the top of the Marcus parabola [100]. In contrast, the charge recombination process occurs in the inverted regime, consistent with the experimental observation of slower recombination in toluene than in chloroform.

Folded form exhibits multiple charge separation photoproducts

Figure 3.5a-c shows the TA spectra for *folded* **AnEt$_2$-PDI$_2$** measured in the DMSO, acetone, and cyclohexane. All the solvents display similar features, with GSB at 530 nm and SE at 580 nm. The ESA features occur over a broad spectral range between 600 nm and 900 nm, with peaks around 700 nm and 800 nm consistent with the PDI anion peak. However, we do not see significant quenching of the SE peak, except at very early times. Additionally, another positive peak around 590 nm appears in these spectra, which decays very fast, almost at the same rate as the decay PDI anion.

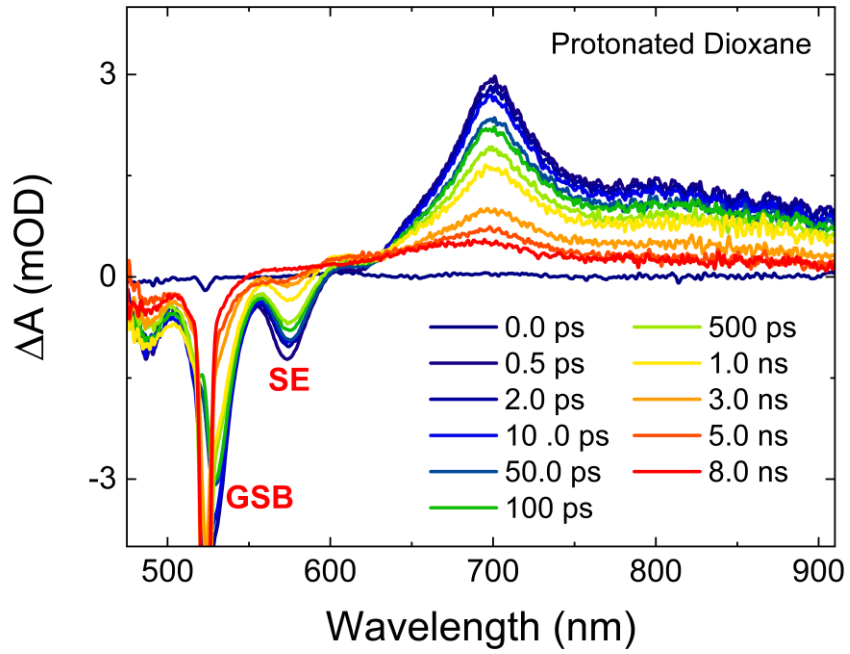

Figure 3.6: TA measurement of open PDI-AnEt$_2$-PDI in protonated dioxane at 530 nm excitation in a 2mm cuvette.

The TA data for the *folded* form in DMSO, acetone, and cyclohexane are all fitted with a four kinetic component model in the global fitting scheme, and the associated decay-associated difference spectra (DADS) are shown to the right of the spectral traces in Figure 3.5. The global fits exhibit a similar trend in DMSO, acetone, and cyclohexane. As mentioned above, the first component, DADS1 (light grey), is attributed to the coherent artifact due to the instrument response function. After the IRF, the TA spectra exhibit a lineshape described by DADS2 (green) spectra, which has the spectral feature of ground-state bleach and ESA with peaks at 705 nm and 803 nm and no SE contribution. The lineshape features of DADS2 correspond to the charge recombination process of **PDI$^{\bullet-}$-AnEt$_2^{\bullet+}$-PDI**. This green trace decays in 4.0 ps (DADS2$_{DMSO}$), 3.5 ps (DADS2$_{acetone}$), and 8.9 ps (DADS2$_{cyclohexane}$) to the third DADS3 (blue). Here we see an ESA with peaks of 590 nm and at 705 nm and 805 nm of PDI anion. Previous reports indicate that PDI cation exhibits an ESA at 590 nm [81,97]. The coexistence of PDI cation and anion peaks in *folded* **AnEt$_2$-PDI$_2$** form with identical dynamics suggests that the charge separation occurs between two PDI chromophores instead of bridge-mediated donors through symmetry-breaking charge transfer (SBCS) mechanism and the time constant associated with DADS3 assigned to the charge recombination of **PDI$^{\bullet-}$-AnEt$_2$-PDI$^{\bullet+}$**. After 148 ps (DADS3$_{DMSO}$), 115 ps (DADS3$_{acetone}$), and 143 ps (DADS3$_{cyclohexane}$), this trace evolves into the

last (red) DADS4, wherein the line shape features reproduce the PDI excited state decay spectra. This decays in 1.4 ns ($DADS2_{DMSO}$) and ~5 ns in acetone and cyclohexane and can be assigned to fluorescence emission. However, the *folded* **$AnEt_2$-PDI_2** are expected to undergo excimer formation due to H-aggregation [91]. Therefore, to further investigate the emissive nature of the DADS4, we perform time-resolved fluorescence measurement to rule out the possibility of excimer formation in *folded* $AnEt_2$-PDI_2 conformation.

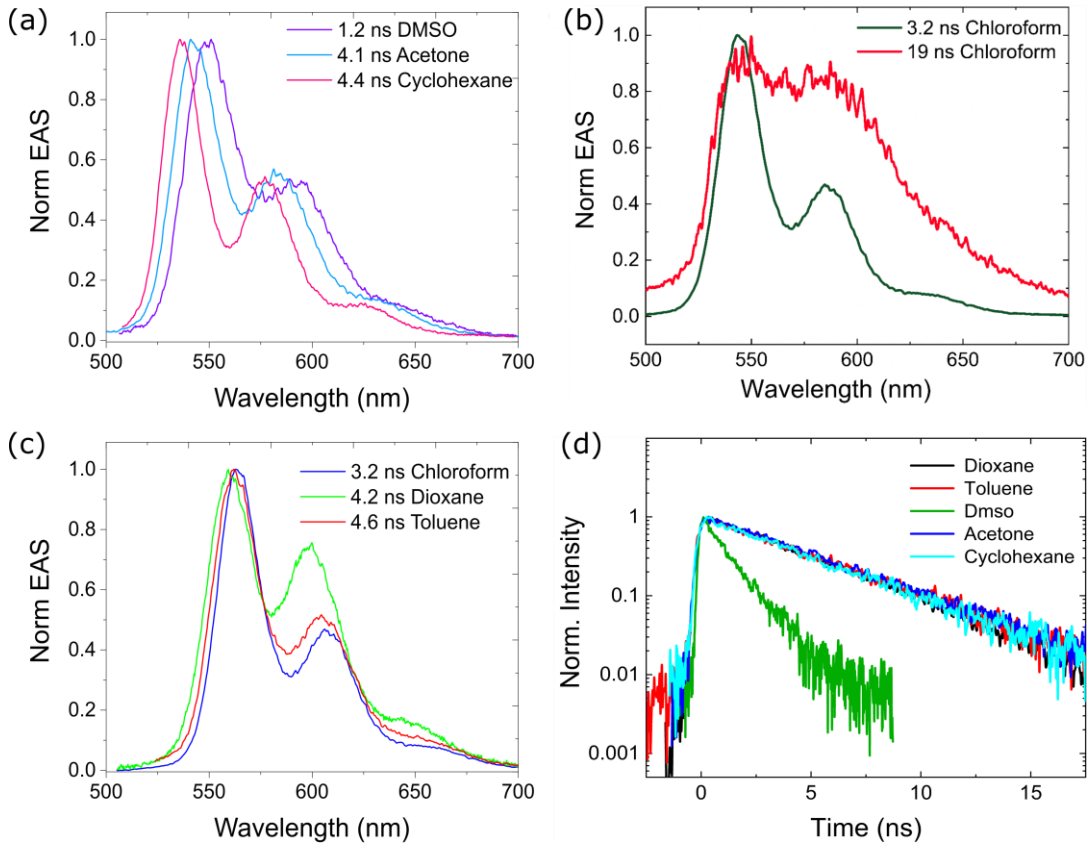

Figure 3.7: (a) Evolution associated spectra of open form and (c) closed form obtained from the global fitting (b) Evolution associated spectra of open PDI-$AnEt_2$-PDI in chloroform obtained after global analysis of TRF data. The two kinetic spectra obtained with the lifetime of 3.2 ns which corresponds to fluorescence emission while the second kinetic spectra decay with 19 ns and having lineshape indicative of excimer formation. (d) Time resolved fluorescence kinetic decay at 546 nm of PDI-$AnEt_2$-PDI in all the solvent under study. All the Kinetic spectra is on the top of each other and decay at the same rate except in case of DMSO, where the fluorescence decays very fast within 2 ns, consistent with the observation from the TA measurement.

Time-resolved photoluminescence confirms multiple pathways based on conformation

Time-resolved photoluminescence lifetimes and quantum yield measurements in all of the studied solvents are summarized below in table 1. The TRPL data can be globally fit using only one exponential decay (Figure 3.7), and the spectral lineshape reproduce PDI relaxation except in the case of chloroform, where two components are needed, as shown in Figure

3.7b. The first component decaying in 3.1 ns is assigned to fluorescence relaxation. In comparison, the second component's lineshape and lifetime (19 ns) indicate excimer formation, which is consistent with the results obtained from the TA measurement. Furthermore, the TRPL results were compared with the fluorescence relaxation components obtained in all the solvents with *open* and *folded* configurations. We find that the lifetime from TRPL measurement matches remarkably well with the fluorescence relaxation process obtained from the global analysis.

Table 3.3 Transient fluorescence lifetime of PDI-AnEt$_2$-PDI in all the solvent of open and folded forms with their respective quantum yield. The (+) represents the measurement in the protonated solvent of dioxane in open form

Configuration	Solvent	Lifetime (TA)	Lifetime (TRPL)	QY (%)
open	Chloroform	3.1 ns, 26 ns	3.2 ns, 19 ns	48.9
	Dioxane/Dioxane(+)	5.1 ns	4.8 ns	7.5 /(45.6)
	Toluene	4.7 ns	4.6 ns	6.7
Folded	Acetone	4.6 ns	4.6 ns	8.2
	Cyclohexane	4.4 ns	4.4 ns	7.4
	DMSO	1.2 ns	1.3 ns	3.3

Similarly, the quantum yield (QY) data shows that fluorescence in chloroform is almost 50% quenched relative to the reference PDI monomer. This quenching in chloroform is due to charge separation and excimer formation. The QY value decreased in toluene and dioxane to 6-8%. This decreased quantum value indicates improved charge separation efficiency in toluene and dioxane. Furthermore, QY of dioxane reached approximately 50% after the protonation which is similar to the QY value observed in the chloroform. The QY value between 3-8% is also observed in *folded* AnEt$_2$-PDI$_2$ conformation in all the solvents. This lower value is due to the efficient symmetry-breaking charge separation.

3.3 Conclusion

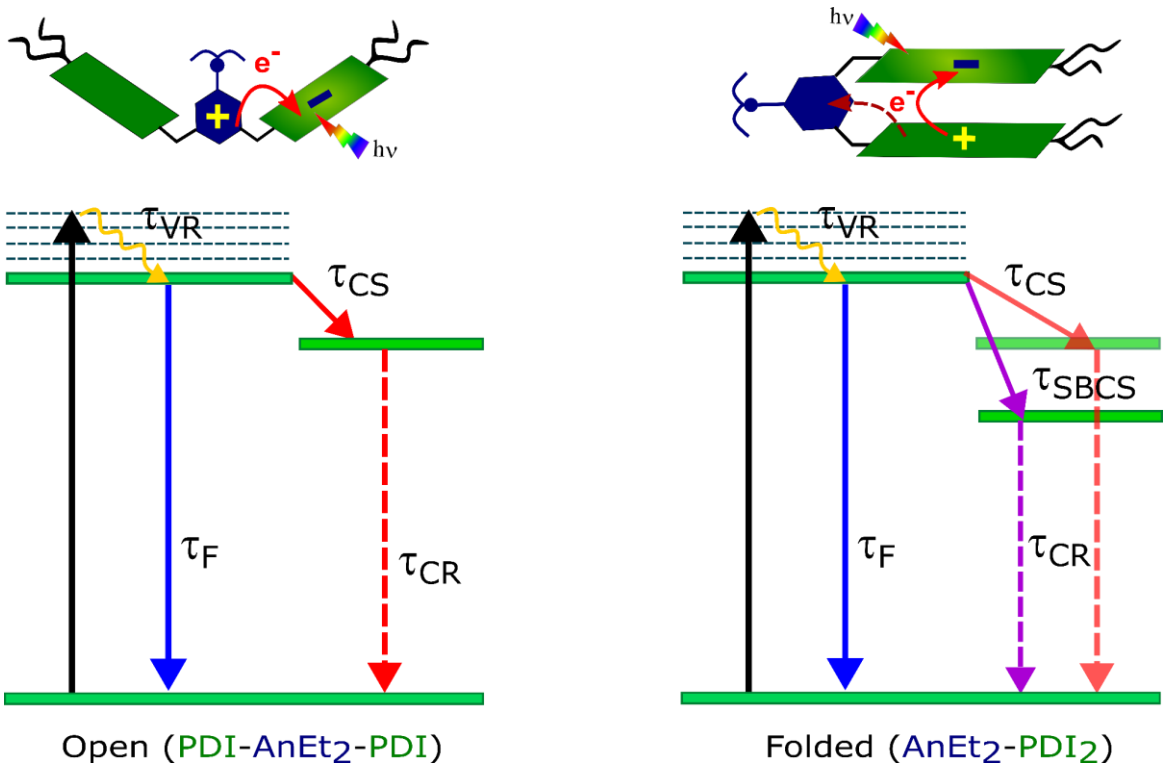

Figure 3.8: The Jablonski diagram shows the primary photophysical pathways observed in open vs folded form.

We have synthesized a triad acceptor-donor-acceptor system PDI-$AnEt_2$-PDI with PDI acting as acceptor and dimethylaniline as the donor capable of having different conformations with *open* and *folded* forms. We explored the photophysical properties in both the conformation with varying solvent polarities using ultrafast transient absorption and fluorescence spectroscopy. The measurement demonstrated that PDI-$AnEt_2$-PDI undergoes charge separation upon photoexcitation, but the electron transfer mechanism differs in *open* verse *folded* forms, and the rate of charge separation and recombination depends on the solvent polarity. In the open configuration, charge separation occurs from the bridging donor to one of the PDI acceptors with maximum charge separation efficiency in nonpolar toluene rather than in polar chloroform, while in folded form, the two types of charge-separated species are observed. The first charge-separated species resemble *open* conformation where PDI units acts as acceptor and undergo electron transfer with the bridging $AnEt_2$ donor unit, while the second and dominant species represent the symmetry-breaking charge transfer between two PDI chromophores in all the solvent with diminished quantum yield. We believe that the SB-CS is observed due to the formation of H-aggregates in the *folded* form, which enhances the

electronic coupling between two PDI acceptor units in the triad system. Moreover, observing two kinds of charge-separated species connotes the different degrees of H-aggregation in the *folded* form.

3.4 Experimental section

Materials

The PDI monomer for control experiments (N, N-dipentyl-3,4,9,10-perylenedicarboximide) and all the solvents used in this study were purchased from Sigma-Aldrich and used without further purification.

Steady-state absorption and fluorescence

Steady-state absorption spectra were collected using a halogen-deuterium lamp (DH2000-DUV, OceanOptics) connected to a USB spectrometer (34000-UV-VIS-EIS, OceanOptics). Steady-state fluorescence was measured on a Horiba/Jobin Yvon Fluorolog-3 Spectrofluorometer, using an excitation wavelength of 440 nm. Quantum yield is calculated relative to a reference PDI chromophore from the literature [89].

Transient absorption spectroscopy

TA spectroscopy was measured using a Helios-Fire pump-probe setup (Ultrafast systems). This is paired with a regeneratively amplified 1030 nm laser (Light Conversion Pharos, 200 fs, 200 uJ), set at an effective repetition rate of 1 kHz via an internal pulse picker. A small portion (20%) of the 1030 nm fundamental is directed towards an optical delay line and, subsequently, to a sapphire crystal to generate the broadband probe light (480-900 nm). The remaining 80% of the 1030 nm fundamental is fed to an optical parametric amplifier (Light Conversion, Orpheus-F) to generate the pump light (λ_{ex} = 530 nm for *open* and λ_{ex} = 490 nm for *folded* form). Samples were measured in a 2 mm pathlength cuvette with continuous stirring during the experiment. The relative polarization between the pump and probe beam was set at 54.7 ^{o} to avoid anisotropic effects.

Global analysis of the TA data was done using the R-package TIMP software [48,101] with the graphical interface Glotaran 1.5.1 [49]. Global analysis is a method where all the wavelengths are analyzed simultaneously to a set of common time constants representing a sum of

exponential decay [102]. We interpreted our results using both sequentially interconverting and parallel decaying sum-of-exponential models. The sequential model results in a number of evolution-associated difference spectra (EADS) converting into successive EADS with associated mono-exponential decay rates. This method quantitatively describes the system's evolution of excited and intermediate states involved. The spectral lineshape of EADS does not always reflect the pure electronic state of the species involved and can be the mixture of spectra arising from the ground state, excited state, or photoinduced intermediate species evolved. The parallel model produces decay-associated difference spectra (DADS). The DADS represents the spectral changes related to the specific time constant and is equivalent to spectral change occurring during the evolution of one EADS to another. This model is useful when several photophysical processes compete and proceed simultaneously. The global analysis scheme evaluates EADS and DADS simultaneously. Since both methods are mathematically equal, the same time constant applies to both EADS and DADS [102]. In this work, the results are interpreted using both EADS and DADS due to possible branching and kinetic competition between photophysical pathways.

Time-resolved photoluminescence

TRPL was measured using a C5680 streak camera (Hamamatsu). The samples were photoexcited at λ_{exc} = 440 nm, using the output from regeneratively amplified Ti: sapphire laser (Coherent, Astrella, 5 mJ, 35 fs, 800 nm, 1 kHz) paired with an optical parametric amplifier (Coherent, Opera Solo). The samples were measured in solution using 2 mm pathlength cuvettes with front-face illumination. The temporal range of the measurement was adjusted based on solvent: DMSO (10 ns time window, 0.12 ns instrument response), chloroform (50 ns time window, 0.60 ns instrument response), other solvents (20 ns time window, 0.24 ns instrument response).

Chapter 4 : Quantifying exciton annihilation effects in thermally activated delayed fluorescence materials

Important parameters for the design and performance of thermally activated delayed fluorescence (TADF) emitters are forward and reverse intersystem crossing rates between singlet and triplet states. The magnitude of these rates is determined from the prompt and delayed transient photoluminescence decay. We demonstrate that this photoluminescence decay strongly depends on the initial photoexcited population density due to exciton-exciton annihilation processes. By kinetic modelling of the power-dependent time-resolved photoluminescence of the TADF emitter 9,10-bis(4-(9H-carbazol-9-yl)-2,6-dimethylphenyl)-9,10-diboraanthracene (CzDBA) we identify singlet-triplet annihilation (STA) and triplet-triplet annihilation (TTA) as the main loss processes with rate constants in the order of 10^{-17} m^3 s^{-1}. Neglecting these quenching processes leads to erroneous estimates of the (reverse) intersystem crossing rates.

Thakur, K., van der, B., Wetzelaer, G.-J. A. H., Ramanan, C., Blom, P. W. M., Quantifying Exciton Annihilation Effects in Thermally Activated Delayed Fluorescence Materials. *Adv. Optical Mater.* 2022, 10, 2101784.

4.1 Introduction

Thermally activated delayed fluorescence (TADF) materials are an emerging class of molecular systems utilized in the third generation of organic light-emitting diodes (OLEDs), which are showing great promise for highly efficient OLEDs in future commercial applications [10,103,104] as well as in other fields such as bioimaging. [105–107] These molecules offer the possibility to harvest light from both singlet and triplet excitons, allowing for a potential 100% internal quantum efficiency (IQE) in OLEDs. In contrast to earlier generation phosphorescent emitters, TADF systems can harvest triplet excitons without the

incorporation of heavy metals in their molecular structure{Formatting Citation} The molecular structure of TADF emitters consists of electron donor and electron acceptor moieties with strong through-bond or through-space charge transfer coupling. This leads to a very small energy gap between the singlet charge-transfer (S_1) and triplet charge-transfer (T_1) states (usually only several tens of meV). As a result, excitons in the dark T_1 state undergo reverse intersystem crossing (rISC) at room temperature to the emissive S_1 state, contributing as delayed fluorescence (DF) to the light output next to the regular prompt fluorescence (PF) (Figure 4.1). [108]

The simplified Jablonski diagram in Figure 4.1a depicts the electronic transitions in a TADF system. After generating excitons with singlet and triplet character, singlet excitons relax to the ground state on a timescale of nanoseconds, termed prompt fluorescence (PF). Triplet excitons can undergo rISC, resulting in delayed fluorescence from S_1 on the timescale of microseconds. The overall fluorescence efficiency of a TADF material depends on the rates of forward (k_{ISC}) and reverse (k_{rISC}) intersystem crossing between S_1 and T_1. These photophysical parameters are typically characterized using time-resolved photoluminescence measurements (TRPL) to track the dynamic evolution of the S_1 emission. A typical TRPL curve for a TADF system exhibits a bi-modal decay, attributed to the PF and DF contributions to the PL. This is often described by using a biexponential function [109–111]:

$$I(t) = A_1 \exp\left(-\frac{t}{\tau_{PF}}\right) + A_2 \exp\left(\frac{-t}{\tau_{DF}}\right) \quad (1)$$

Photophysical parameters such as the singlet lifetime τ_s and triplet lifetime τ_t are then derived and used to calculate the intersystem crossing (ISC) rate k_{ISC} and rISC rate k_{rISC} , along with the prompt/delayed fluorescence quantum yields ($\varphi_{PF}/\varphi_{DF}$). The k_{rISC} is then given by [112]:

$$k_{rISC} = \frac{1}{\tau_{DF}} \frac{\varphi_{PF} + \varphi_{DF}}{\varphi_{PF}} \quad (2)$$

However, the bi-exponential model relies on several assumptions that are not always valid. Firstly, the relationships only hold when $\varphi_{DF} \geq 4*\varphi_{PF}$, requiring that the quantum yield of fluorescence *via* the triplet state be more than four times the yield obtained directly from singlet decay. [113,114] This assumption makes sure that the reverse intersystem crossing is close to 100% in the material. Furthermore, for TADF systems in the solid state, a multi-exponential PL decay may be observed. A common practice has been to use multi-exponential

fitting with three to four components. In order to still obtain a characteristic time constant for the prompt and delayed fluorescence the fast components are then averaged and assigned to PF, whereas the time average of the slow components is then takes as representative for DF. The occurrence of multiple time constants has been attributed to the conformational distribution of the molecules in the solid-state film and incomplete geometrical relaxation of the excited states. We note that this behavior is similar to observations in polymer semiconductors, which exhibit heterogenous photoexcited lifetimes due to energy transfer, conformational disorder, and spectral diffusion in the solid state. [115], [116] In OLEDs, TADF emitters are typically diluted in a wide bandgap host. When diluting an emitter, a variety of local environments introduces several molecular conformations, which can lead to a spread in CT energies and thus rISC rates, justifying the use of a multi-exponential fit. [117] But in the case of a neat film of the TADF emitter 9,10-bis(4-(9H-carbazol-9-yl)-2,6-dimethylphenyl)-9,10-diboraanthracene (CzDBA), the PL decay was fitted with a three exponential model, and τ_{DF} was then taken as the average of the two slow components. [118] Since the physical origin of a third decay component is not clear, such an approach might lead to a misinterpretation of the DF decay time τ_{DF} and therefore to erroneous estimates of the forward (k_{ISC}) and reverse (k_{rISC}) intersystem crossing rates.

Another limitation of the model described in equation (1) is that it does not account for additional excited state deactivation pathways, especially non-radiative recombination including various annihilation process. Such quenching processes play an important role in the device performance of TADF OLEDs and efficiency roll-off at high luminance. [119–122] These include triplet-triplet annihilation (TTA), triplet-polaron quenching (TPQ), and singlet-triplet annihilation (STA). For the emitter 1,2,3,5-tetrakis(carbazol-9-yl)-4,6-dicyanobenzene (4CzIPN) it was shown that the PL quantum yield below 100K is strongly suppressed and accompanied by a strong dependence of the transient PL on excitation intensity, which was attributed to the occurrence of a triplet-triplet annihilation process. [120] Figure 4.1a describes how these processes can affect the fluorescence output of a TADF system. In TTA two triplet excitons interact to form an intermediate state, which finally decays into a singlet or triplet, lowering the overall number of the total emissive excitons. Note that we here omit the formation of the quintet state, although allowed by conservation of total momentum, since its energy lies too high to be reached at room temperature.[20] Similarly in STA, one

singlet and triplet interact together where the singlet decays non-radiatively to the ground state, and only the triplet excited state remains. These non-radiative pathways are highly dependent on experimental conditions, such as excitation density, and can affect the reproducibility of the PL decay. This in turn influences the interpretation of photophysical dynamics in TADF systems.

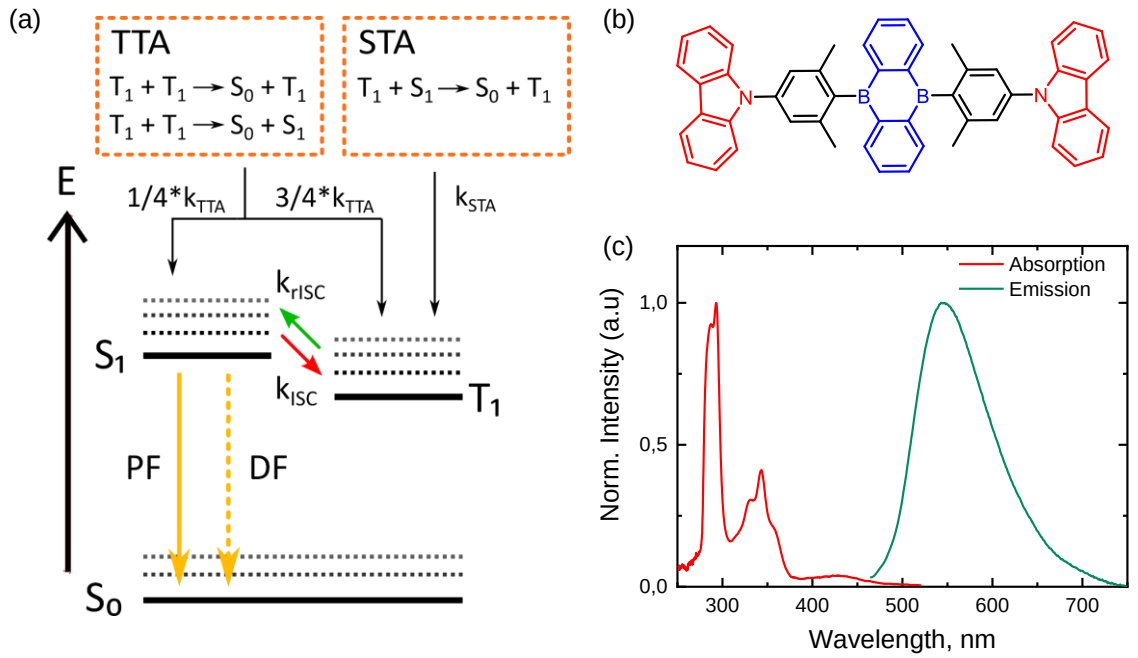

Figure 4.1: (a) Mechanism of TTA and STA processes (top) and their relative contributions under electrical excitation (black arrows) to the excited state energy levels of a TADF material, which are depicted in the Jablonski diagram below. The working mechanism of a TADF material relies on efficient forward and reverse intersystem crossing (ISC and rISC) between the excited singlet and triplet charge-transfer states (S_1 and T_1). (b) Molecular structure of CzDBA, which consists of two donor carbazole units (red) connected to the diboraanthracene acceptor (blue). (c) The steady-state absorption (red) and emission (green) spectra of CzDBA in toluene.

As an alternative for the biexponential model, kinetic rate models have been used to fit PL transients based on measurable inputs and subsequently extract photophysical parameters, including contributions from annihilation. [123–125] Annihilation processes depend on the incident laser power in PL experiments and thus a systematic investigation into these quenching processes can therefore be conducted by studying the power dependence of the prompt and delayed fluorescence. In earlier work, power-dependent PL curves were fitted with rate equations incorporating various quenching processes. [124] However, this analysis led to power-dependent annihilation constants, which showed no clear correlation with their respective power density. In this paper, we combine power-dependent time-resolved

photoluminescence measurements with a kinetic modelling approach based on rate equations of the singlet and triplet exciton concentrations using CzDBA as efficient model system. This method can be universally applied to all TADF emitters, irrespective of their PF/DF yield. Our results show that the power-dependent PL decays can be fit correctly by incorporating TTA and STA, leading to quenching constants in the order of ~10^{-17} m^3 s^{-1}. The quantified quenching constants further allow us to calculate the relative contribution of the various loss processes to the overall loss of singlet excitons as a function of time and excitation power density. This approach can be generally utilized for all TADF materials to provide more reliable and accurate characterization of their photophysical rate constants.

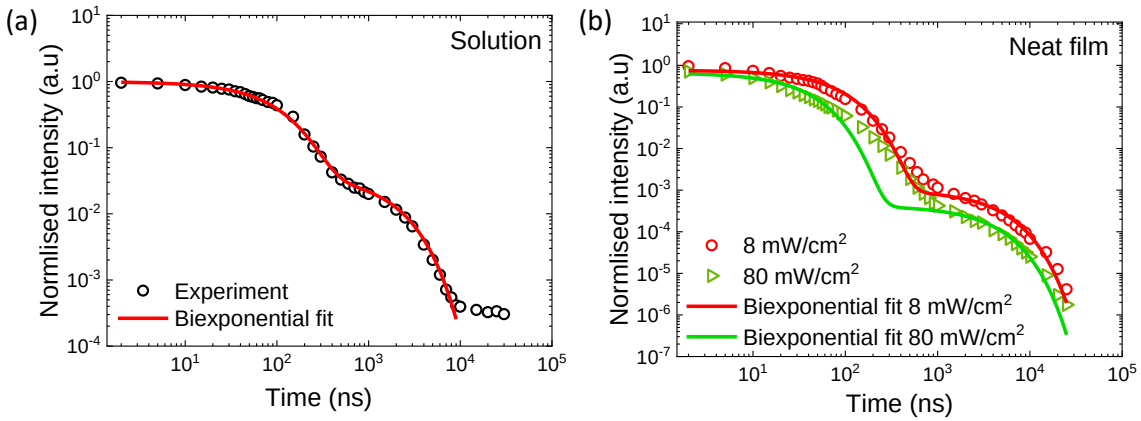

Figure 4.2: (a) The photoluminescence transient of CzDBA in solution at a power density of 8 mW/cm² in black with its biexponential fit in red. (b) The photoluminescence transient of a CzDBA neat film at power densities of 8 mW/cm² (red) and 80 mW/cm² (green) where the solid lines represent their biexponential fit respectively.

4.2 Results and discussion

CzDBA film PL decay exhibits contributions from annihilation mechanisms

The TADF emitter CzDBA was chosen as a model system to characterize the photoluminescence decay. This material exhibits high PLQY in neat films (>90%), low trap/defect density, low self-quenching, [118,126] and has been utilized in a high-performance undoped single-layer OLED with EQE values of 19%. [126] The steady-state absorption and fluorescence spectra of the CzDBA solution are shown in Figure 4.1c and are consistent with the spectra reported in literature. [118] The absorption peaks are located at

293 nm (Cz donor), 343 nm (DBA acceptor), and a small tail centered at 430 nm arising from the intramolecular charge-transfer (CT) state absorption. CzDBA exhibits a broad featureless fluorescence spectrum with its maximum at at 544 nm, characteristic of emission from a CT state, as is typical for TADF materials. [118,127]

We measured the photoluminescence (PL) decay dynamics of CzDBA in solution and in film to disentangle intrinsic vs. multi-chromophoric contributions, as shown in Figure 4.2. The films are photoexcited at 350 nm and the transient PL kinetics are averaged across the 542-545 nm wavelength range. While all of the decay curves qualitatively exhibit a bimodal line shape that is expected for a TADF emitter, we find that the PL transient of the solid film cannot be well described using the simple biexponential function given by Equation 1.

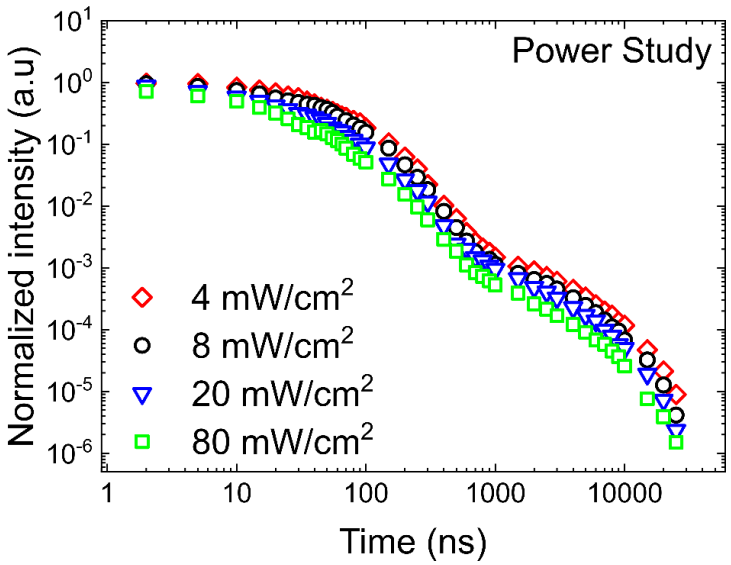

Figure 4.3: Normalized intensity of PL decay versus time at different power density.

The PL decay kinetics of CzDBA in solution are well fit using a biexponential function. We assume no multi-chromophore processes in the solution measurement, and so the physical significance of this biexponential fit is explained as a linear combination of prompt and delayed fluorescence mechanisms (τ_{PF} and τ_{DF}). In this case, the prompt fluorescence (τ_{PF}) is attributed to the singlet lifetime and represents the decay to the ground state S_0 of excitons that initially populate S_1. The delayed fluorescence (τ_{DF}) arises from fluorescence that occurs as a result of the repopulation of S_1 by T_1 via rISC, and is therefore correlated to the effective triplet lifetime. Therefore, $\tau_{PF} = \tau_s$ and $\tau_{DF} = \tau_t$. Based on this, we retrieve values of τ_S = 100 ns and τ_t = 1.8 µs for CzDBA in solution. This is in agreement with previously reported

values. [127] Note that the effective triplet lifetime is the time an exciton remains in the triplet state and is not to be confused with the intrinsic triplet lifetime, which would represent the decay of the triplet to the ground state (phosphorescence). Intrinsic triplet lifetimes are commonly in the order of 100 µs to even ms, [128,129] but in the case of TADF systems, rISC presents a faster deactivation pathway for the triplet state.

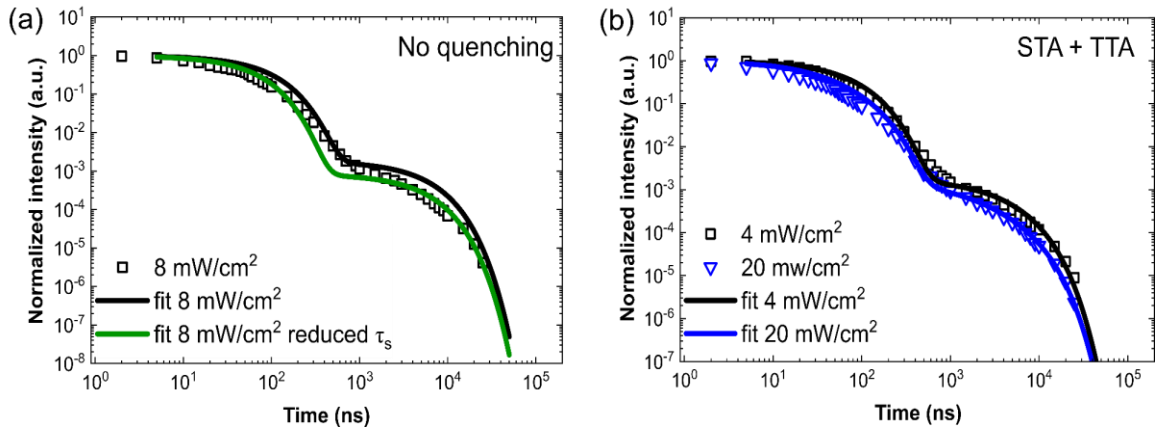

Figure 4.4 (a) Normalized intensity versus time a power density of 8 mW cm^{-2} complemented by a kinetic fit in red with 98 ns lifetime and green solid line corresponds the kinetic fit with the reduced singlet lifetime of 65 ns. (b) Normalized intensity versus time a power density of 4 mW cm^{-2} and 20 mW cm^{-2} complemented by a kinetic fit. The corresponding parameters can be found in table 1

The transient PL measurement was also carried out on a CzDBA neat film, measured at four different excitation power densities (Figure 4.3). The shape of the decay curves depends on the excitation power, with the film exhibiting a faster decay lifetime with increasing excitation power. The decay curves for the lowest and highest excitation powers are shown in Figure 4.2b, along with attempted biexponential fits using Equation 1. In contrast to CzDBA in solution, the biexponential fit strongly deviates from the measured PL decay for the neat film. This effect is particularly pronounced in the intermediate time scale (100-1000 ns). The deviation is also greater at the higher 80 mW/cm^2 excitation power than at the lower 8 mW/cm^2 excitation power. This suggests that the origin of the deviation depends on the initial photoexcited population.

We further note that the PL decay in film exhibits a longer lifetime than that in solution, ~4.0 vs. 1.8 µs. This is attributed to conformational freedom in solution leading to enhanced vibronic coupling and therefore increased non-radiative internal conversion to the ground state. This finding is supported by the high PLQY value of >90% in neat CzDBA films vs only 14% in solution. [118] Despite this evidence for decreased non-radiative quenching due to

internal conversion in the film samples, the lack of agreement with a biexponential fit and the observed power dependence indicates that other non-radiative quenching mechanisms arise in the neat film, which are not present in solution.

The results shown in Figure 4.2b clearly show that at a high excitation power density (80 mW/cm^2) the biexponential decay model cannot describe the CzDBA PL decay dynamics in the solid-state. Previous work on TADF systems has also reported such observations. [114,117,130] Even at lower excitation density (8 mW/cm^2) there is still some discrepancy between the model and experiment. Applying the biexponential model to this lower intensity (red solid line) would result in τ_s and τ_t of 75 ns and 4.0 µs respectively. Similarly, for higher excitation density (80 mW/cm^2) τ_s and τ_t would be 33 ns and 3.5 µs respectively, which clearly indicates the power dependence of prompt and delayed lifetimes.

Kinetic modelling deconvolutes exciton annihilation contributions to PL decay

An alternative approach to analyze the PL decay that also incorporates quenching processes is to model the transient PL using rate equations for the singlet and triplet exciton populations.

It is known that in PL measurements the emission occurs predominantly from the charge transfer state (CT), but the operation of a TADF system involves locally excited singlet and triplet states as well. [131] After photoexcitation, a singlet can also first be generated in the locally excited singlet (LE) state which can decay radiatively before undergoing electron transfer to form a CT state. It is the singlet CT state that is being continuously re-populated through rISC, not the LE state, meaning that only at early times in a PL decay LE states could potentially play a role. Similarly, the rISC does not directly occur from the triplet CT state but it first undergoes vibronic mixing between locally excited triplet states and CT state and proceed via LE to the singlet CT state. [132] The time scale at which the mixing takes place is very fast compared to the observed prompt and delayed lifetime. The contribution of the LE singlet state to the total light output is low, whereas the LE and CT triplet state can be effectively considered as one. [123] Hence, the TADF dynamics can be approximated by a three energy level model, considering only S_0, S_1 and T_1 and the interactions between them as described in Figure 4.1a. Note that the absence of charge carriers in PL measurements

means that the aforementioned TPQ mechanism will not play a role, and is therefore neglected.

Correspondingly, the rate equation for the singlet density *[S]* and triplet density *[T]* for a three-level model is given by:

$$\frac{d[S]}{dt} = [S_0] - \frac{[S]}{\tau_s} - k_{ISC}[S] + k_{rISC}[T] - k_{SSA}[S][S] - k_{STA}[S][T] + 0.25k_{TTA}[T][T] \quad (3)$$

$$\frac{d[T]}{dt} = -\frac{[T]}{\tau_T} + k_{ISC}[S] - k_{rISC}[T] - 1.25k_{TTA}[T][T] \quad (4)$$

Where [S_0] is the initial singlet density, k_{SSA} *is* the singlet-singlet annihilation constant, k_{STA} is the singlet-triplet annihilation constant, k_{TTA} is the triplet-triplet annihilation constant, [S] is the singlet concentration, and [T] the triplet concentration. To exclude the contribution of specific quenching processes, their respective annihilation coefficient can simply be set to zero. Equations (3) and (4) are solved in a numerical fashion using the finite difference method with a sufficiently small-time step of 5 ns. The various rate constants can subsequently be extracted from fitting the normalized PL data to [S].

Figure 4.5 shows the kinetic modelling of film PL kinetics at power densities of 8 and 80 mW/cm^2, considering no annihilation (a), each STA (b) and TTA (c) independently, and finally STA and TTA together (d). In Figure 4.5a the PL decays are modeled assuming no contribution from TTA or STA quenching processes. In that case, the fitting for the two power densities is on top of each other and fails to reproduce the experiment in both the PF and DF part and their power dependence. We attempted to improve the fit using a reduced singlet lifetime of 65 ns as well (Figure 4.4a). However, the fit still does not match the experimental data in the transition region between the time scale of 100 ns to 1000 ns, and the higher power density cannot be fit at all (not shown). This strongly supports our hypothesis that TTA and STA quenching phenomena are playing a crucial role in these film decay dynamics.

Next, we modeled the PL decays with an included contribution from STA (Figure 4.5b). This model describes the prompt emission very well. However, the fit insufficiently describes the delayed emission. Similarly, we attempted to fit the data considering only quenching by TTA (Figure 4.5c). In this case, the model successfully fits the delayed emission at later times and improves the fit of the transition region between PF and DF at higher powers, but fails to

describe the faster prompt fluorescence region. We finally considered both STA and TTA processes as simultaneously contributing to exciton quenching by using the full model described in the equation (3) and (4) (Figure 4.3d). This complete model is able to fit the kinetic decay across the entire measured time range and at all excitation powers (see Figure 4.4b for corresponding data and fits for the additionally measured excitation densities of 4 mW/cm^2 and 20 mW/cm^2).

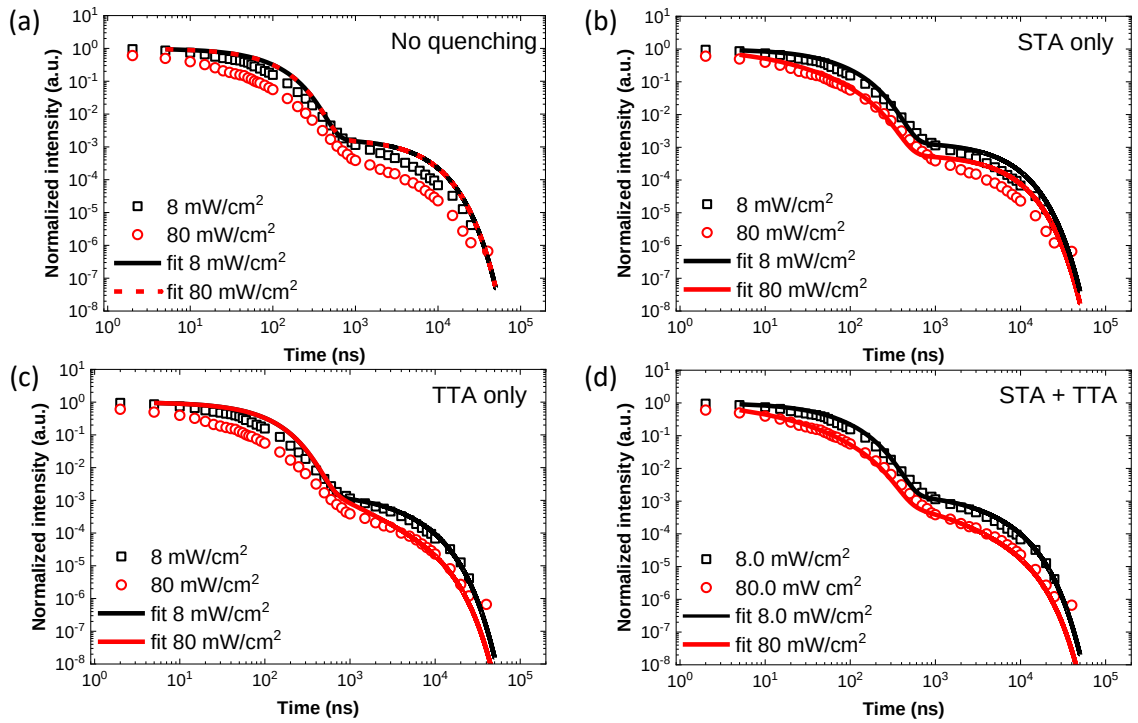

Figure 4.5: Normalized PL intensity versus time for (a) no quenching processes, (b) only STA, (c) only TTA and (d) complete. Open symbols represent the measured data whereas the lines correspond to a fit with our kinetic model.

While our STA+TTA model fits the measured PL decay completely, other loss processes could also be contributing to the PL decay dynamics. For example, singlet-singlet annihilation (SSA) is another process that could potentially reduce the singlet population. Figure 4.6b shows the influence of SSA on the power dependence of the PL transients. It does not reproduce the line shape of the experimental data as the fit gets steeper in the intermediate region compared to STA, nor can it be used in combination with another quenching process to obtain a good fit. This leads us to conclude that SSA is not a major decay process for singlet excitons, in agreement with previous findings. [119] Furthermore, other recent work has proposed spontaneous dissociation of charge-transfer excitons as an additional exciton annihilation process.[32] This, however, is most likely to occur in a fluorophore with a large permanent

dipole moment, which would facilitate the process. CzDBA is a symmetric molecule, with dipole moment close to 0.[33] We also carried out our measurements on films without any electrodes, precluding the possibility of an internal electric field which could influence spontaneous exciton dissociation.

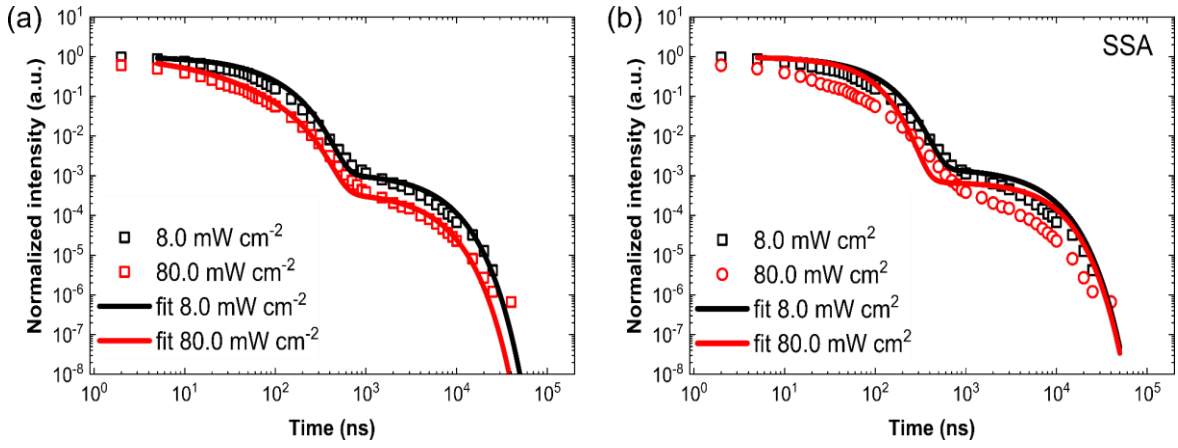

Figure 4.6: (a) Normalized intensity vs time for two power densities with a fit that includes STA and also sets $k_{(r)ISC}$ as variable fit parameters. In order to achieve a reasonable fit, k_{rISC} has to be changed from $2.4x10^5$ to $2.8x10^5$ s^{-1} and k_{ISC} has to be changed from $7x10^5$ to $4.6x10^5$ s^{-1} when going from 8.0 to 80 mW cm^{-2}. (b) Normalized intensity vs time for two power densities, complemented by a fit including SSA as a quenching process, with $k_{SSA} = 5x10^{-17}$ m^3 s^{-1}.

From the kinetic modeling, we obtain a singlet lifetime of 98 ns which is in close agreement with the lifetime obtained in solution (Figure 4.2a). This validates that our modelling approach can accurately give the intrinsic singlet lifetime. The model successfully fits the PL decay transients at different power densities using a single set of power-independent rate constants of k_{ISC} , k_{rISC} , k_{TTA} and k_{STA} (Table 1). This point is further illustrated in-depth in Figure 4.6a, where the two decays at 8 and 80 mW/cm^2 are fit using only STA in conjunction to changing k_{ISC} and k_{rISC} at every excitation power density. Although this method can also achieve a satisfactory fit for every excitation power, it requires a power dependent $k_{(r)ISC}$, which is physically not realistic. Using this fitting approach for higher excitation powers, the lack of triplets normally disappearing by TTA has to be compensated in such a way that the value of k_{ISC} almost equals k_{rISC}, which for a down- and the up-hill process is physically not meaningful. An alternative explanation for an apparent power dependence of r(ISC) could originate from the presence of triplet-to-singlet FRET mechanisms.[34] However, the possibility of this process diminishes with high rISC rate, as observed for CzDBA, which also contributes to the nearly 100% PLQY of CzDBA. Therefore, we do not expect triplet-to-singlet FRET to play a significant role in CzDBA photophysics.

*Table 4.1. Values of several photophysical parameters for the biexponential model from the literature and our kinetic fits presented in Figure 4. 5. * For the intrinsic triplet lifetime we assume a lower limit of 100 µs, such that phosphorescence does not play a role.*

Method	**τ_s (ns)**	**τ_t (μs)**	**k_{ISC} (s^{-1})**	**k_{rISC} (s^{-1})**	**k_{STA} ($m^3\ s^{-1}$)**	**k_{TTA} ($m^3\ s^{-1}$)**
Biexponential fit [118]	34	1.0	1.7×10^7	6.7×10^5	-	-
Kinetic fit (this work)	98	100*	1.0×10^6	2.2×10^5	2.5×10^{-17}	8.0×10^{-18}

Using the obtained quenching rate constants of $k_{TTA} = 8 \times 10^{-18}$ $m^3\ s^{-1}$ and $k_{STA} = 2.5 \times 10^{-17}$ $m^3\ s^{-1}$, we can also further evaluate the forward and reverse ISC rate constants k_{ISC} and k_{rISC}, which amount to 1.0×10^6 and 2.2×10^5 s^{-1}, respectively (Table 1). We observe that the approximation of a biexponential decay leads to an overestimation of the k_{ISC} and k_{rISC} by more than an order of magnitude. A similar large value of k_{ISC} of 3.8×10^7 s^{-1} was reported in an earlier photophysical study on CzDBA using a three-exponential fit. However, the excitation density at which these data were taken was not provided. [118] Comparison with our data suggests that these reported PL decays were taken at an elevated excitation density of around 80 mW/cm^2, as their PF lifetime of 34 ns corresponds well to our 33 ns from a bi-exponential fit at said power density. This shows that ignoring the effect of exciton quenching processes at too high excitation densities can give rise to large errors in the derived forward and reverse ISC rates.

We note that for the intrinsic triplet lifetime we used 100 µs as a lower limit. Since the rISC process is in the 3 µs regime this means that the triplet states are almost completely depopulated by this process only. Increasing the intrinsic triplet lifetime to 1 ms in our model does therefore not change the obtained forward and reverse ISC rates and quenching rates.

Furthermore, the k_{TTA} value obtained from the kinetic modeling and power dependent PL measurements ($k_{TTA} = 8 \times 10^{-18}$ $m^3\ s^{-1}$) is in very good agreement with a previous report, where k_{TTA} was extracted from the electrical efficiency roll off of a single layer CzDBA OLED, using a similar rate equation approach, where $k_{TTA} = 1 \times 10^{-17}$ $m^3\ s^{-1}$ was found. [121] Here, TTA was found to be the dominant mechanism controlling the EQE roll-off [121] without the need to include STA. However, in PL we have to take into account the occurrence of STA as well. This is likely connected to the difference in exciton generation mechanism. In an OLED, singlets

and triplets are generated in a 1:3 ratio, assuming simple spin statistics. This is in stark contrast to the situation in PL, where only singlets are initially generated. We can qualitatively say that the difference in population implies a prevalence of TTA over STA in OLEDs, whereas this does not have to hold in PL.

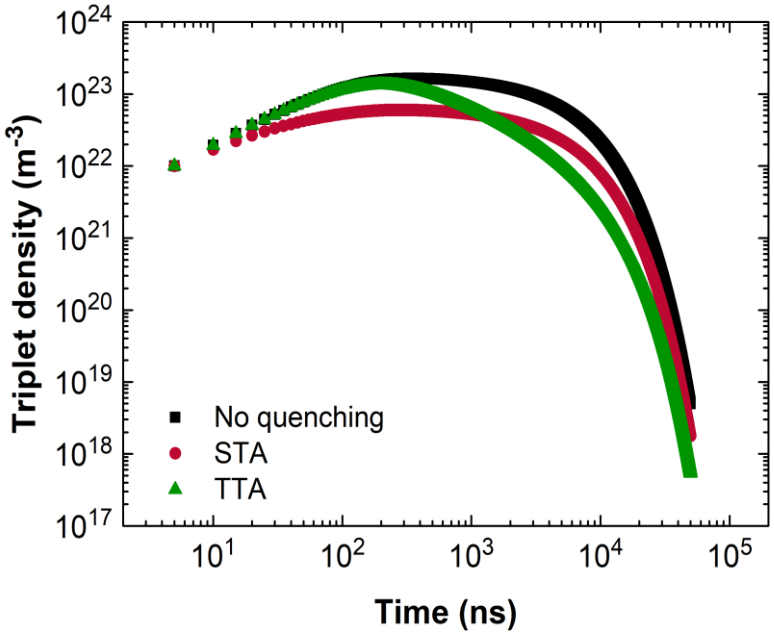

Figure 4.7: Triplet exciton density versus time. The triplet density is simulated with an initial singlet exciton density of 2 × 10^{24} m^{-3}, corresponding approximately to a power density of 80 mW/cm^2.

The obtained rate constants allow us to visualize the impact of the STA and TTA processes on the triplet exciton population in PL. In Figure 4.7, the simulated triplet density versus time is displayed, including the two annihilation processes and, for comparison, also the situation of no quenching. For all three cases the triplet population exhibits a build-up via ISC until reaching a time τ_s (98 ns), after which rISC (and TTA if taken into account) causes it to decay. Taking STA into account leads to a reduction in the triplet density already at times below 100 ns, whereas the triplet density with TTA closely follows the situation of no quenching at early times. As already observed (Figure 4.5b), STA reduces the singlet population at early times, but through ISC it indirectly decreases the triplet population as well. The quadratic scaling of TTA with the triplet density means that it has almost no influence at these timescales. However, the negative impact of TTA is clearly seen at times beyond 100 ns, where after ~1000 ns the curve with TTA drops below the curve with STA. In the delayed fluorescence

region (> ~1000 ns) emissive singlets are generated from triplets through rISC and Figure 4.4 shows that the main quenching in this region originates from TTA.

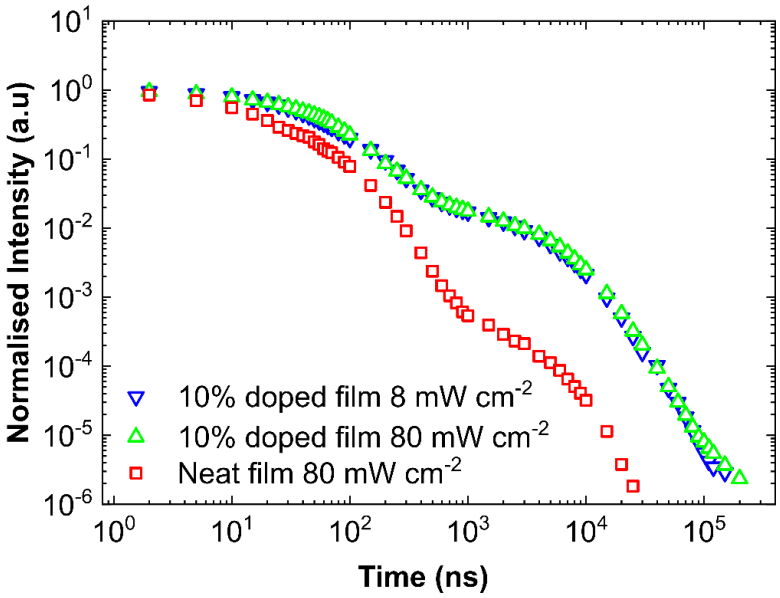

Figure 4.8: Normalized intensity of PL decay versus time for a CBP: 10% CzDBA film of 8.0 and 80.0 mW cm^{-2}. This diluted film shows no excitation density dependence, confirming that the excitation density dependence in the neat film arises from the bimolecular annihilation processes. The experimental data from the neat film at 80.0 mW cm^{-2} is shown for the comparison.

We note that in practice TADF emitters are often diluted in a wide band-gap host, and in such a blend the contribution of the bimolecular annihilation processes will be weakened. Our above results focused on neat films because CzDBA in particular can attain high OLED performance even without a host.[25] Nonetheless, we also measured the fluorescence decay dynamics in a host:guest sample (CBP: 10% CzDBA) and find that the power dependence disappears, as expected (Figure 4.8). This confirms that the power dependence in the pristine films originates from bimolecular annihilation processes.

4.3 Conclusion

We have shown that the transient photoluminescence of TADF emitters can be strongly affected by the chosen excitation power due to various exciton quenching mechanisms, in particular STA and TTA. Application of biexponential or multiexponential decay models may lead to overestimation of the forward and reverse ISC rates. The kinetic modelling used in this study can accurately fit the transient photoluminescence spectra at various excitation powers and is capable of the direct determination of the intrinsic singlet lifetime, rate of (reverse)

intersystem crossing, singlet-triplet annihilation and triplet-triplet annihilation constants. The obtained k_{TTA} value of 8×10^{-18} m^3 s^{-1} is close to a previously obtained value from OLED data. Reliable characterization of PL decays aids in the development and evaluation of high-performance TADF materials.

4.4 Experimental section

Sample preparation

CzDBA was obtained from Luminescence Technology Corporation and CBP from Sigma-Aldrich. Both were used without further purification. Samples were prepared by evaporating 100 nm onto a quartz substrate under a base pressure of around 2×10^{-6} mbar. The sample was loaded into a home-built air-tight sample holder inside a glovebox before it was transferred out for the spectroscopic measurements. All measurements were carried out at room temperature. A 5uM degassed solution of CzDBA in toluene was used for steady-state absorption and fluorescence, as well as for time-resolved fluorescence in solution. These measurements were done in a 2 mm path length quartz cuvette.

Spectroscopic characterization

Steady-state absorption was measured on a home-built setup consisting of a deuterium halogen lamp (DH2000-DUV, OceanOptics) connected to a USB spectrometer (34000-UV-VIS-EIS, OceanOptics). Steady-state fluorescence was measured on a Horiba/Jobin Yvon Fluorolog-3 Spectrofluorometer, using 400 nm excitation. Time-resolved photoluminescence measurements were carried out using a 4Picos gated-iCCD camera (Standford Computer Optics). Samples were photoexcited at 350 nm using the output from a Ti: sapphire laser (Coherent, Astrella, 1 kHz, 5 mJ, 35 fs) paired with a commercial optical parametric amplifier (Coherent, OperA). The spectra are collected using the 4Spec software (Stanford Computer Optics) using gating times ranging exponentially from 0.5-5000 ns and spectra were recorded out to 50 µs. The photoexcitation light was focused onto the sample in order to ensure a uniform excitation density throughout the film. The spot size of 0.8 mm at the sample position was characterized using a beam profiler (Coherent, LaserCamHR-II).

For the power study, the lowest incident power was chosen to minimize annihilation processes while maintaining a good signal-to-noise ratio. We varied the power at least an

order of magnitude but kept the highest power low enough that bleaching or other degradation effects of our films during the measurement would play a minor role and would not impede our analysis.

Analysis

The initial singlet density was calculated from the absorption spectrum and the incident laser power using a reported method. [124] At a low power density, where annihilation does not play a large role, the values of $k_{ISC}/k_{rISC}/\tau_s$ can be determined. The power dependence provides information on the various quenching processes, as detailed in the results and discussion section.

Chapter 5 : Effect of tert-butyl group on the photophysics of solution processable thermally activated delayed fluorescence emitters.

Thermally activated delayed fluorescence materials (TADF) materials typically consist of small molecules, which are not suited le for-solution processing. The addition of tert-butyl groups to the periphery of TADF emitters has proven to improve their solubility in various organic solvents, to reduce aggregation-induced quenching, and to enhance the photoluminescence quantum yield (PLQY) of the materials. We study the effect of the addition of a tert-butyl group on the photophysical properties of a blue TADF emitter consisting of a carbazole (Cz) donor and a triazine (Trz) acceptor. We find that the addition of a tert-butyl group increases the rate of reverse intersystem crossing (rISC), while at the same time the non-radiative decay rate substantially decreases. In addition, we dilute the 3tCzTRZ film in a host matrix and find that a further improvement in PLQY up to 100% is associated with a decrease in the non-radiative decay rate, while there is no change in the rISC rate.

Kalyani Thakur, van der, B., Wetzelaer, G.-J. A. H., Ramanan, C., Blom, P. W. M., Effect of tert-butylation group on the photophysics of solution processable thermally activated delayed fluorescent emitters. (Manuscript Submitted)

5.1 Introduction

Thermally activated delayed fluorescence materials are a promising third generation of materials for organic light-emitting diodes (OLEDs), which have the capability of harvesting triplet excitons in order to obtain 100% internal quantum efficiency (IQE) [133,134]. In these state-of-the-art emitters, electron-donor acceptor moieties are coupled into configurations that yield a small singlet-triplet splitting, thus promoting reverse intersystem crossing (rISC) of the initially non-radiative triplet state to the radiative singlet state. Highly efficient TADF OLEDs have been demonstrated, typically with small molecule emitters embedded in a multilayer structure [135], reaching internal quantum efficiencies close to 100% [136]. In such vacuum deposited devices external quantum efficiencies exceeding 30% have been reported [137]. However, especially for blue TADF emitters there are still some major challenges to overcome. One issue is the decreasing efficiency at higher brightness, the so-called efficiency roll-off, where most commercial applications operate [138]. Another problem is that the operational lifetime of TADF OLEDs are still impractically low for commercial purposes [138,139], something that is exacerbated by the inherently high exciton energy of blue emitters. A lot of research nowadays therefore focusses on achieving stable TADF emitters with blue emission.

In addition to shifting the emission wavelength to bluer wavelengths, there is also a drive to develop solution processable TADF materials, which are highly desirable from a commercialization standpoint. The fabrication costs associated with the more standard thermal evaporation method, which requires high vacuum and good thermal stability of the material [140], is very high, making it less attractive for large area fabrication [141]. On the other hand, solution processable methods such as spin coating, spray coating, inkjet printing are more desirable for large scale and low cost fabrication [33]. A large number of materials including small molecule, dendrimer, and polymer materials have been synthesized with the goal to simultaneously achieve excellent TADF characteristics, having the right color coordinate in the blue region, and to be solution processable [137,142]. Furthermore, solution processable TADF materials are compatible with flexible substrates and generate a relatively small amount of waste [137], making a purely organic solution processable blue TADF OLED having high efficiency the aim, but this remains a challenge.

The main condition to achieve solution processing requires good miscibility of the material in organic solvents and ability to form a homogenous film [142]. For small molecules, a common approach to achieve solution processability is to dope them in a wide bandgap host [143–145]. This leads to a myriad of problems such as undesirable film morphologies, aggregation of the emitter as well as unintentional interactions between the host and emitter [146]. In an effort to overcome these problems, various directions have been explored and two of such potential routes include TADF polymers and dendrimers. TADF dendrimers are from size point of view in between small molecules and polymers, where the TADF active part is a small molecule, but with large sidechains (dendrons) attached to it [137,146]. In TADF polymers, the TADF active group, often a small molecule, is introduced either in the main chain, or as a pendant group in a linear polymer [147]. The highest EQE obtained for a solution processable TADF polymer with orange-greenish emission is 20% by Yang et al. [148] Similar values were obtained for solution processed dendrimer based TADF OLEDs, where a highest EQE of around 24% was obtained by Ban et al., for blue and green emitting OLEDs [149]. Both approaches are promising routes towards solution processability of TADF emitters, however their design structure is limited by a complex synthesis, and especially for TADF polymers, the existence of left-over impurities from the synthesis [150]. Moreover, the EQEs of TADF OLEDs based on polymer and dendrimers are still lower as compared to small molecule based TADF emitters.

Another approach is to make the small molecules themselves more amenable to solution processing. In 2014, Cho et al., developed a highly efficient green solution processable OLED based on the small molecule 4CzIPN with an EQE of 18%. Here, the carbazole moiety of the molecules were modified with a tert-butyl group to improve the solubility [151]. Other moieties like methyl and other akyl group have also been explored to improve the solubility of TADF emitters, but the tert-butylation has so far resulted in the highest efficiencies of solution processed devices [152].

Tert-butyl substitution has been widely used to make organic materials soluble, accompanied by good film formation. Xie et al., [153], reported blue hetero-donor solution processable blue TADF emitters with an EQE as high as 26%. The authors ascribed the high EQE to the highly twisted hetero-donor configuration, which was achieved by tert-butylation. Similarly, in an another study by Shi et al., using tert-butyl substituted donor and acceptor TADF

emitters OLEDs with 20% EQE were realized [154]. The improved device performance of tert-butyl substituted TADF emitters are often attributed to a plethora of causes, including reduced non-radiative decay, reduced non-radiative self-quenching arising from bimolecular annihilation processes, but also to reduction in intersitites and defects which lead to charge trapping [155–157]. Despite the abundantly reported positive effects of tert-butylation, a systematic photophysical study into the effect of tert-butylation is presently lacking, which would be beneficial for the design of future solution-processable TADF materials. In this work, the impact of tert-butlyl substitution on the photophysical properties has been studied in a blue TADF emitter, consisting of a carbazole donor and a fluorine substituted triazine acceptor in 9,9',9''-(5-(4,6-bis(4-fluorophenyl)-1,3,5-triazine-2-yl)benzene-1,2,3-triyl)tris(9*H*-carbazole) (**3CzTrz**)**,** and the tert-butylated variant 9,9',9''-(5-(4,6-bis(4-fluorophenyl)-1,3,5-triazin-2-yl)benzene-1,2,3-triyl)tris(3,6-di-*tert*-butyl-9*H*-carbazole), referred to as **3tCzTrz** in this study. The molecular structures of both TADF emitters are shown in Figure 5.1a. In addition, we study the effect of dilution with a wide bandgap host on the properties of our **3tCzTrz** films.

We find that tert-butylation enhances the photoluminescence quantum yield (PLQY) in our **3tCzTrz** emitter as compared to the non-tertbutylated variant **3CzTrz.** Dilution of 3tCzTrz in polystyrene (PS) increases the PLQY even up to 100%. The photophysical properties are characterized using steady-state (PLQY) and time-resolved photoluminescence (TrPL) spectroscopy, the latter in combination with kinetic rate equations, where we use the non-radiative decay of triplets to account for a PLQY that differs from 100%. Our results reveal that the addition of a tert-butyl group on the Cz donor moiety increases the reverse intersystem crossing rate by about a factor of 4, and decreases the non-radiative triplet decay constant, consistent with the observed change in PLQY. The enhanced PLQY by diluting the 3tCzTrz in polystyrene is associated with a further decreasing non-radiative decay constant, in addition to an increase in singlet lifetime, while rISC remains the same. Our study shows that tert-butylation enhances the photophysical properties of TADF emitters, and our insights contribute to realizing efficient solution processable TADF materials for low-cost fabrication.

5.2 Results and discussion

Steady state absorption and photoluminescence:

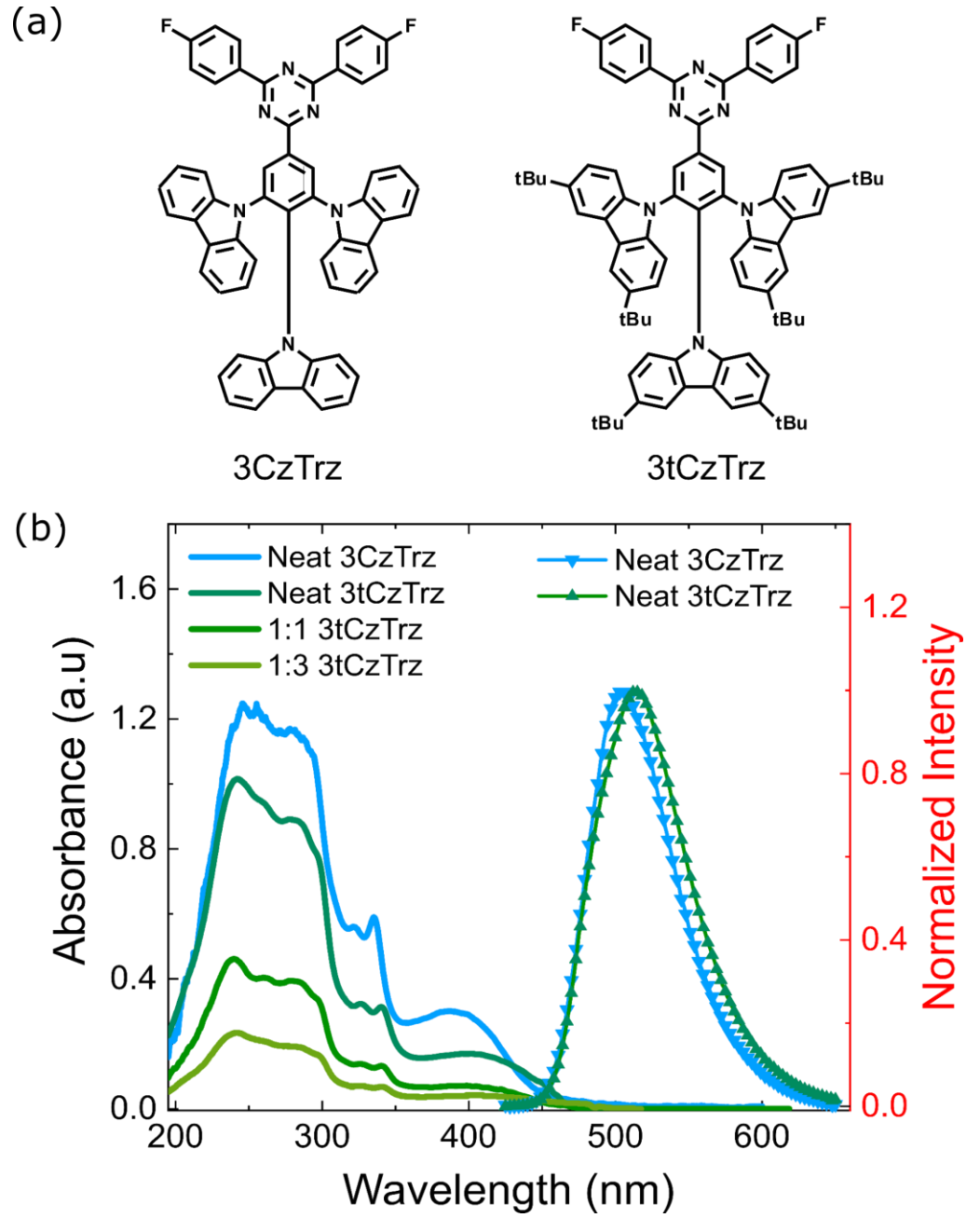

*Figure 5.1: (a) Chemical structure of **3CzTrz** and tert-butyl substituted **3tCzTrz**. (b) Absorption spectrum of solution processed neat film of 3CzTrz and 3tCzTrz in blue and green respectively; and 1:1 and 1:3 dilution of 3tCzTrz in polystyrene (PS) in the gradient of green color respectively. The spectra in the downward facing (in blue) and upward facing (in green) triangles represent the steady-state emission of neat film **3CzTrz** and **3tCzTrz** respectively.*

Figure 5.1 shows the chemical structure of **3CzTrz** and **3tCzTrz** along with their steady-state absorption and emission spectra in a neat film of thickness 100 nm. The absorption band at the shorter wavelength region (200-300 nm) is assigned to the π–π* from the conjugated

backbone of the compound. The absorption bands between 290-330 nm are associated with n-π^* absorption peaks of the Cz moiety [158–160]. The lower energy transition extending from 355 nm to 450 nm is assigned to the singlet charge transfer (CT) band arising from the interaction of the electron donating Cz with the electron accepting Trz. This CT band is responsible for the TADF emission [161]. The emission spectrum of **3CzTrz** in the neat film exhibits a peak at 490 nm and yields a sky-blue color. The emission spectrum of the tertbutyl substituted **3tCzTrz** is slightly red-shifted, exhibiting a peak at 505 nm.

Transient photoluminescence:

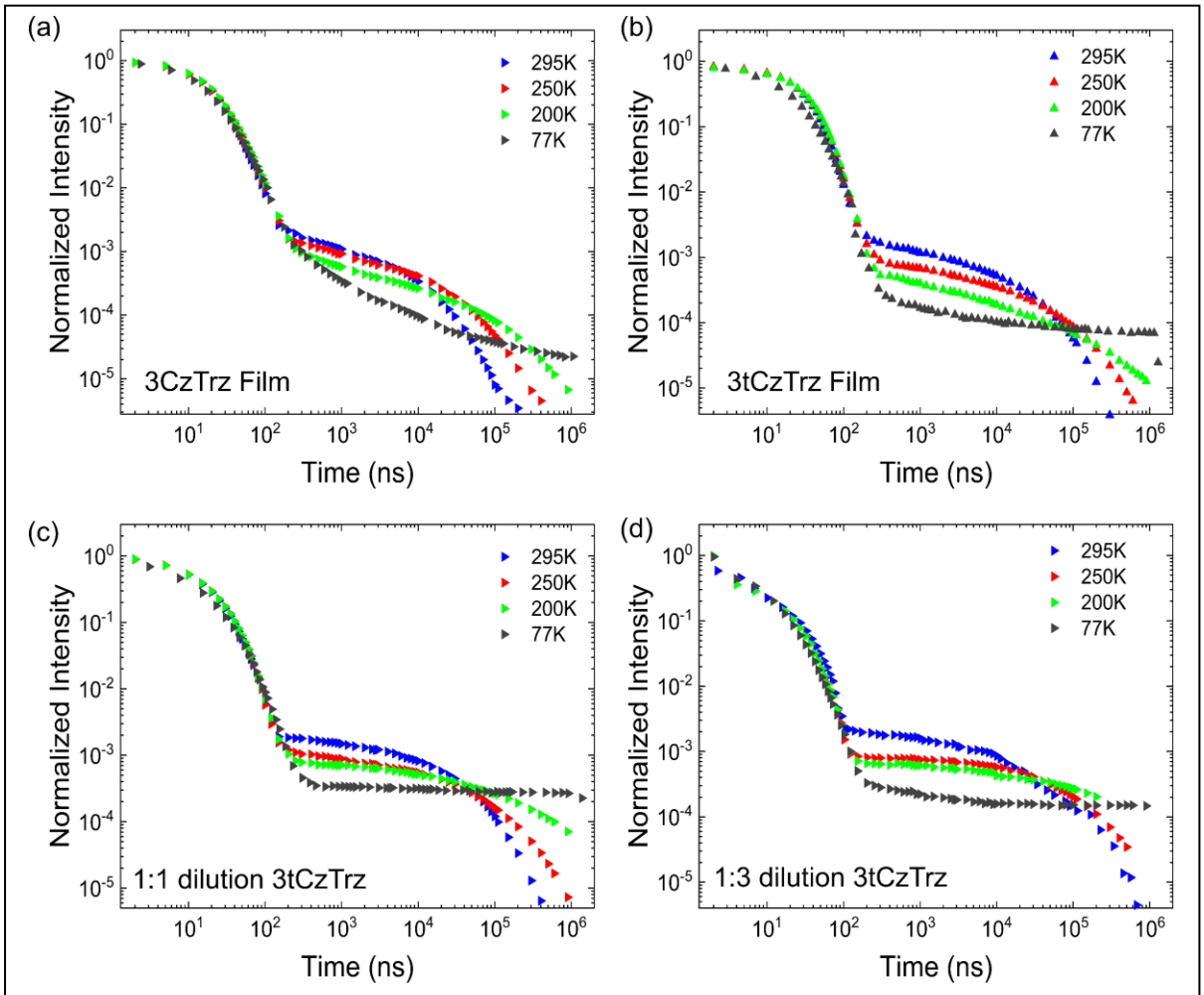

*Figure 5.2: Temperature scan of transient photoluminescence spectra of (a)-(d) the neat film of **3CzTRZ** and **3tCzTRZ** and (c)-(d) diluted film of **3tCzTRZ** in polystyrene host.*

Figure 5.2 shows that both **3CzTrz** and **3tCzTrz** exhibit TADF, as verified by the temperature dependent TRPL data. The log-log plot of PL intensity versus time shows the characteristic kinetic decay curve, consisting of both a prompt and a delayed fluorescence component. The

prompt component originates from fluorescence of optically generated singlets that have not undergone any other cycling process, whereas the delayed component is fluorescence of generated singlets that transferred to the triplet state by ISC and subsequently have come back to the singlet state through rISC. Since rISC is a temperature activated processes, the delayed component shows a temperature dependence, essentially switching the TADF from the on state at 295 K to the off state at 77 K. We observe that the line-shape of the delayed component of the **3CzTrz** film is different from that of the **3tCzTrz** film, as can be seen in Figure 5.2(a)-(b). Furthermore, the **3tCzTrz** retains its shape even in dilution in a polystyrene host.

Transient PL Modelling:

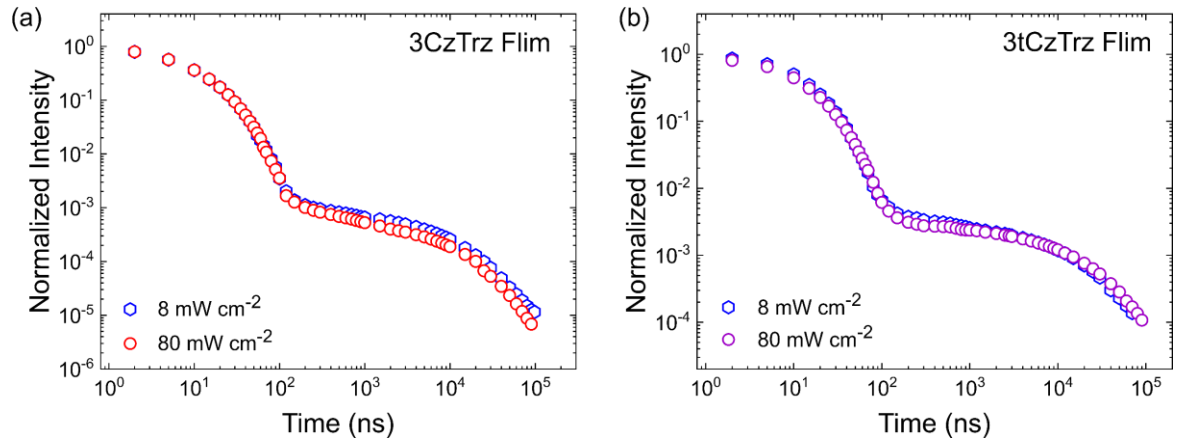

*Figure 5.3: Normalized transient PL curves of (a) **3CzTrz** film (b) **3tCzTrz** film at different power densities. Open symbol represents the measured data. Kinetic curves at 8 mW cm^{-2} and 80 mW cm^{-2} are both on top of each other for the both the cases of 3CzTrz and 3tCzTrz films.*

To determine the effect of tert-butylation on the photophysical properties, we also carry out intensity dependent TRPL measurements on neat films of **3CzTrz** and **3tCzTrz**. In a previous chapter-4, we demonstrated how kinetic modelling can be used to reliably extract photophysical rate constants from TrPL curves [162]. In addition, it was shown that modelling TRPL data at various incident laser powers can be used to estimate the rate constants of bimolecular processes such as triplet-triplet annihilation (TTA) [162]. For completeness and since it forms the basis for the model used in this work, we will shortly revisit the kinetic model here. The singlet and triplet populations take the form of linear differential equations:

$$\frac{d[S]}{dt} = \frac{[S_0]}{dt} - \frac{[S]}{\tau_s} - k_{ISC}[S] + k_{rISC}[T] + 0.25k_{TTA}[T][T] \quad \text{Eq-1}$$

$$\frac{d[T]}{dt} = k_{ISC}[S] - k_{rISC}[T] - 1.25k_{TTA}[T][T] \quad \text{Eq-2}$$

*Table 5.1: PLQY and initial singlet density of for the **3CzTRZ**. **3tCzTRZ** and **3tCzTRZ** on the host polystyrene in 1:3 dilution. The value of PLQY is determined experimentally by measuring the PL emission in ambient and nitorgen environment. The initial singlet density calculated using the formula given in the ref [6]*

	3CzTrz	3tCzTrz	1 : 3 3tCzTrz
PLQY [%]	46	80	100
$[S_0]$ [m^{-3}]	$3.3x10^{23}$	$2.6x10^{23}$	$7.0x10^{22}$

Where $[S_0]$ is the initial singlet density, determined from the absorption of the emitter [162]. The second term on the right-hand side corresponds to monomolecular decay of singlets and triplets, i.e. fluorescence, determined by τ_s, the lifetime of singlets. $k_{(r)ISC}$ is the (reverse) intersystem crossing rate and k_{TTA} the TTA rate constant. Note that the triplet lifetime of the TADF emitter is assumed to be infinite in this equation. These equations are solved using the finite difference method with a sufficiently small timestep.

To estimate the annihilation effects, we first investigated the power dependence (Figure 5.3) on neat films. We see only a very littler power dependence in the TrPL data for **3CzTrz** and no power dependence for the **3tCzTrz** film. This suggests that the contribution of excitation density dependent processes, such as singlet-triplet and triplet-triplet annihilation (k_{STA} and k_{TTA}), are very small. Therefore, we neglect these contributions as a first approximation. However, equations 1 and 2 implicitly assume that the PLQY of the emitter is 100%, which means there is no non-radiative decay. This might be valid for some emitters [163], however this is not the case for the 3Cz emitters used in this work. In Table 5.1, we show the calculated values of the exciton density along with the experimentally determined PLQY for both emitters. We see that adding the tert-butyl groups increases the PLQY substantially, from 46% to 80%, which further increases to 100% in the 1:3 dilution film in a PS host. To take this effect of PLQY into account, a non-radiative decay factor of $-k_{nrT}[T]$ is added to the triplet rate equation, where k_{nrT} is the non-radiative decay constant of triplets. The short effective singlet lifetime originating from a fast ISC rate usually means that the non-radiative decay of singlets

is less significant than the non-radiative decay of the longer living triplets, as was already stated in a previous publication [164]. Therefore, in order to limit the number of fitting parameters, we omit the non-radiative decay of singlets. Thus, the simplified equation without TTA and considering non-radiative triplet decay is given by Equations 3 and 4:

$$\frac{d[S]}{dt} = \frac{[S_0]}{dt} - \frac{[S]}{\tau_s} - k_{ISC}[S] + k_{rISC}[T] \qquad \text{Eq-3}$$

$$\frac{d[T]}{dt} = +k_{ISC}[S] - k_{rISC}[T] - k_{nrT}[T] \qquad \text{Eq-4}$$

*Table 5.2: Summary of photophysical parameters determined from the kinetic fitting of the transient kinetic curves of **3CzTrz** and **3tCzTrz** measured at the power 8 mW cm^{-2}.*

TertButyl Effect	**3CzTrz**	**3tCzTrz**
[S_0] [m^{-3}]	3.3x10^{23}	2.6x10^{23}
τ_s [ns]	80	90
k_{nrT} [s^{-1}]	6.3x10^{4}	1.4x10^{4}
PLQY [%]	37	80
k_{ISC} [s^{-1}]	4.2x10^{7}	4.0x10^{7}
k_{rISC} [s^{-1}]	6.0x10^{4}	1.9x10^{5}

The TrPL decay curves of neat films of **3CzTrz** and **3tCzTrz** are plotted in Figure 5.4, where the most noticeable difference between the two curves is the point of transition from prompt fluorescence (PF) to delayed fluorescence (DF). After calculating *[S_0]* (Table 5.1), the decay curves can be fit to the singlet density, where for the determination of k_{nrT} we use an already reported method [164]. Modelling the TrPL curves of **3CzTrz** and **3tCzTrz** leads to the fits in Figure 5.4 with the parameters presented in Table 2 above. The low power densities of 8 mW cm^{-2} in Figure 5.4 ensures that bimolecular annihilation does not play a large role. The modelling (Table 5.2) reveals that the addition of the tert-butyl group yields two significant contributions to the photophysical characteristics. First, the value of k_{nrT} is decreased by a factor of 4.5 upon tert-butylation. Secondly, there is an enhancement in k_{rISC} by about a factor of 3. Furthermore, the PLQY calculated using the k_{nrT} extracted from the modelling (Table 5.2) is in agreement with the experimentally observed PLQY values (Table 5.1), especially for the 3tCzTrz emitter.

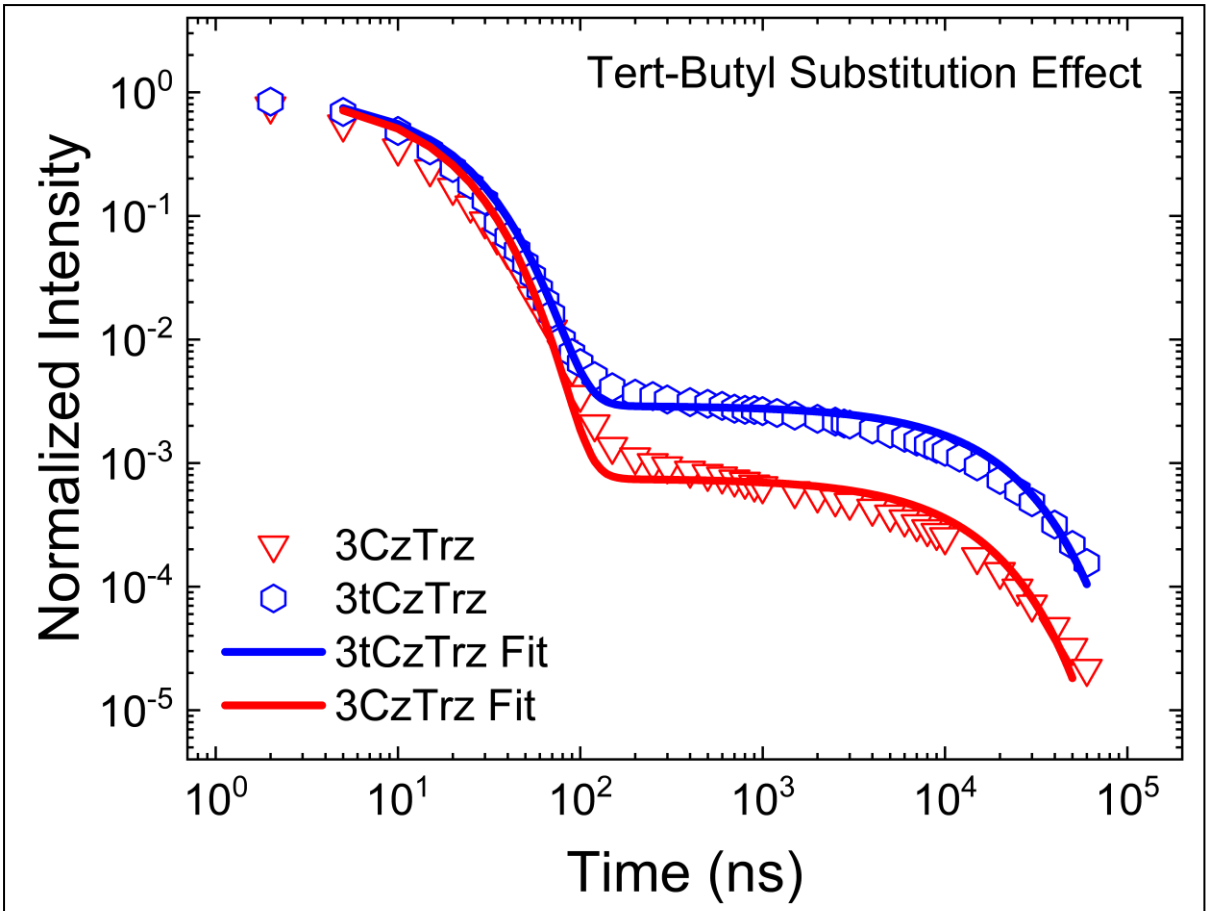

*Figure 5.4: Transient PL curves of neat **3CzTrz** and **3tCzTrz** films at the excitation density of 8 mW cm^{-2} shown in circle symbol in red and blue respectively. The line in red and blue represents the fit obtained from the kinetic modelling of the PL curves.*

The increase in k_{rISC} found in the **3tCzTrz** emitter is exactly what causes the transition region between prompt and delayed fluorescence to move up, as compared to **3CzTrz**, which can be seen in Figure 5.4. The increase in k_{rISC} changes the competitive balance between k_{rISC} and k_{nrT}, automatically leading to less non-radiative decay events. Besides the shift in decay pathways for triplets, also the decrease in k_{nrT} itself is responsible for the increase in PLQY. Decreasing the non-radiative decay of triplets is important for OLEDs, since electrically, triplets are generated in a 3:1 ratio compared to singlets. As already noted before [164], calculating the EQE of an OLED using the value of the PLQY is not entirely correct when a large portion of triplets in the TADF emitter decays non-radiatively. Rather, one should correct for initial 1:3 ratio of singlet:triplet, where electrically the effect of k_{nrT} is naturally larger than in optical experiments [34].

*Table 5.3: Summary of photophysical parameters obtained by the kinetic fitting of TrPL decay of neat **3tCzTrz** and 1:3 diluted **3tCzTrz** film in a PS host*

Dilution Effect	**3tCzTRZ**	**1:3 3tCzTRZ**
$[S_0]$ [m^{-3}]	$2.6x10^{23}$	$7.0x10^{22}$
τ_s [ns]	90	120
PLQY [%]	80	100
k_{nrT} [s^{-1}]	$1.4x10^{4}$	$<1.0x10^{1}$
k_{ISC} [s^{-1}]	$4.0x10^{7}$	$4.0x10^{7}$
k_{rISC} [s^{-1}]	$1.9x10^{5}$	$1.9x10^{5}$

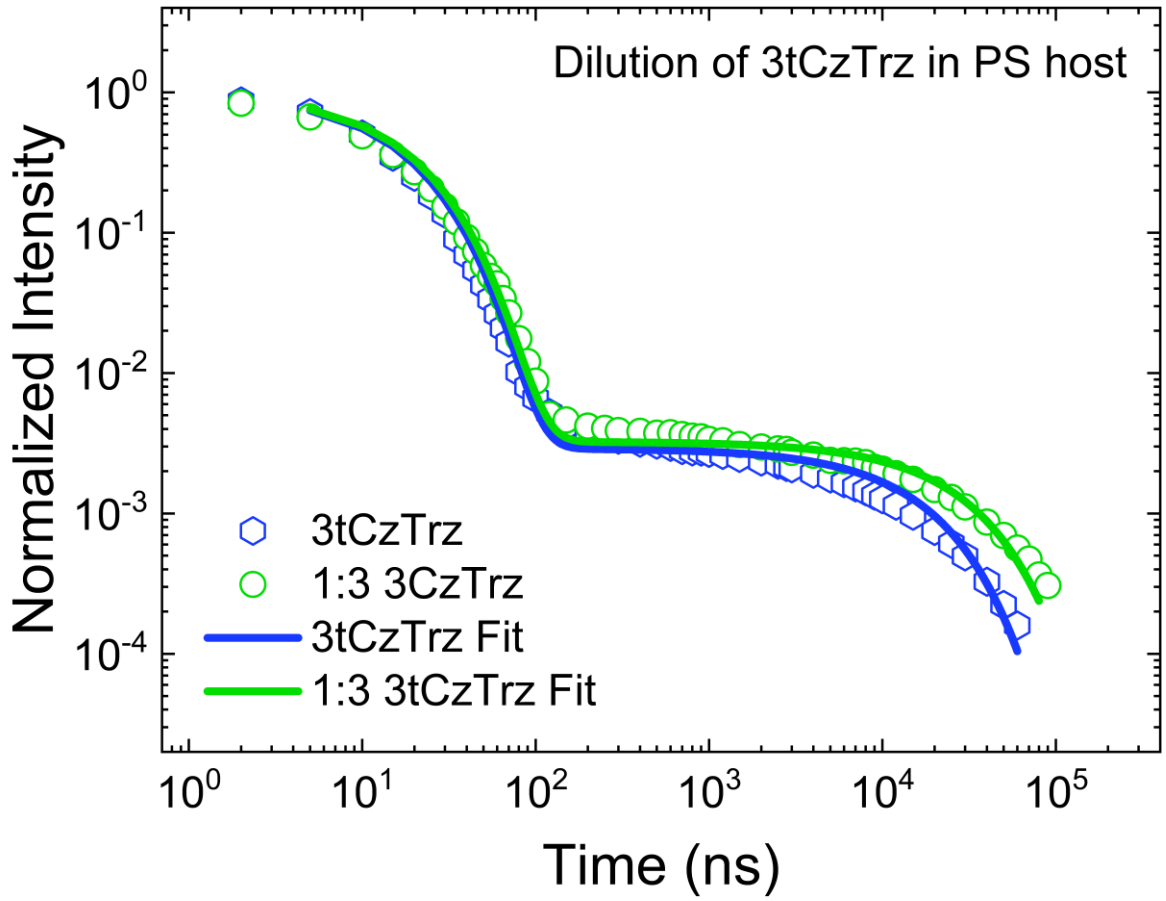

*Figure 5.5: Transient PL curves of neat **3CzTrz** and 1:3 diluted **3tCzTrz** films in polystyrene ratio at the excitation density of 8 mW cm^{-2} shown in circle symbol in red and blue respectively. The line in red and blue represents the fit obtained from the kinetic modelling of the PL curves.*

For **3CzTrz** there is still a slight mismatch between the experimentally determined PLQY of 46% and the one determined from the modelling (37%). We can correct for this by reintroducing the bimolecular decay mechanisms that we neglected in our first

approximation. The small power dependence in the delayed fluorescence of **3CzTrz** seen in Figure 5.1a suggests a small contribution from TTA. Figure 5.6 presents the best fit to the lowest power of our **3CzTrz** emitter using a k_{TTA} of $2x10^{-19}$ m^3 s^{-1}. Although the power dependence is too small to be reliably fitted, using TTA as a decay channel for triplets allows us to raise the value of k_{nrT} to $3.2x10^4$ and consequently the PLQY value to the experimental value of 46%. Although it does not affect our main conclusion, we suggest that TTA plays a small role in **3CzTRz** and can be added as a refinement in the modelling in order to arrive at the experimentally determined value of the PLQY.

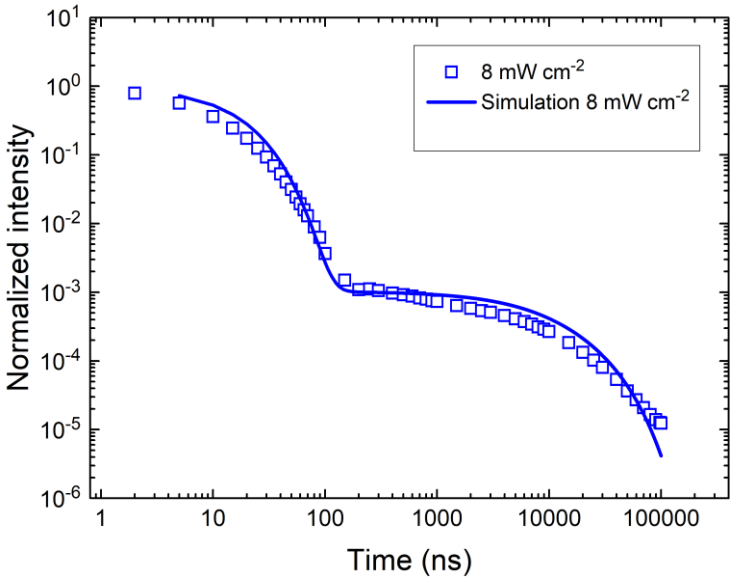

*Figure 5.6: TrPL decay of **3CzTrz** complemented by a kinetic fit with a k_{TTA} of $2x10^{-19}$ m^3 s^{-1}.*

As stated previously, TADF materials are often diluted within a wide bandgap host in order to improve the solution processability. As a next step we investigate the effect of dilution on **3tCzTrz**. We observe that the dilution of **3tCzTrz** in PS further increases the PLQY value, from 80% to almost 100%, as shown in the Table 5.1. We investigate the photophysical parameters of **3tCzTrz** diluted in a PS host in a 1:3 ratio (Figure 5.5). The extracted photophysical parameters are summarized in Table 3 above. Figure 5.5 shows the transient PL curve of the **3tCzTrz** and 1:3 **3tCzTrz** film at a power density of 8 mW cm^{-2}, where we see that the PF is on top of each other, but the later part of the DF tail is higher in the diluted film. Modelling of these kinetic curves reveals that both the ISC and rISC are the same in both the cases, however k_{nrT} changes. There is almost no non-radiative decay in the 1:3 diluted film and k_{nrT} substantially decreases from $1.4x10^4$ s^{-1} in the pristine **3tCzTrz** film to the almost negligible

value of $1x10^1$ s^{-1} in the 1:3 **3tCzTrz** diluted film. Additionally, we see that the intrinsic singlet lifetime also slightly increases in case of the diluted film.

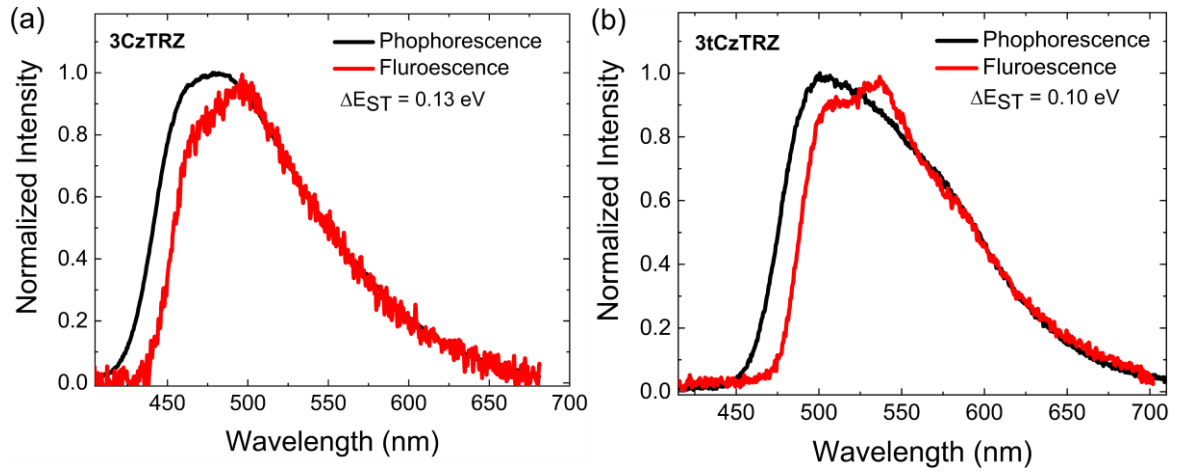

*Figure 5.7: Emission spectra of fluorescence measured at room temperature in black and phosphorescence measured at 77k for (q) **3CzTRZ** and (b) **3tCzTRZ** films.*

Figure 5.7 shows the fluorescence spectra measured at 295 K, together with the phosphorescence spectra measured at 10 K. Since the phosphorescence spectrum shows vibronic features, the singlet-triplet splitting (ΔE_{ST}) calculation is done by fitting the slope of the onset of the emission, which leads to (ΔE_{ST}) values of 0.13 and 0.10 for **3CzTrz** and **3tCzTrz**, which is consistent with the earlier reported value for compounds similar to **3CzTrz**. (Note that this method can have an error bar which approaches the observed difference in the ΔE_{ST} values for the two TADF molecules). The change in ΔE_{ST} can influence the change observed in the k_{rISC} however it doesn't explain the observed reduction in k_{nr}.

For **3tCzTrz** there are two features that contribute to the decreasing k_{nrT} as compared to **3CzTrz**. First, the enlarged spacing caused by the tert-butyl groups decreases the coupling between neighbouring units. Second, a certain fraction of the 3tCzTrz neat film shows a denser and more crystalline packing [165]. The rigidity means a reduction of vibrational motion, which directly explains the less non-radiative triplet decay [166–168]. Moving to the **3tCzTrz:PS** blend, the further decrease of k_{nrT} can be explained solely by the enlarged spacing between the TADF molecules, in accordance with previous work [169]. Next, we also observe a increase in k_{rISC}. It is known that the steric hindrance, coming from the tert-butyl group in our case, can restrict the rotational motion around the donor-acceptor (D-A) angle [170].

Controlling molecular conformation and in particular rigidification of TADF molecules has been shown to lead to favourable route towards optimized TADF emitters [171,172]. Previous work has suggested that more rigid molecular structures tend to have lower values of ΔE_{ST} [168]. It does require a balance however, at the same time large steric hindrance has shown to lead to the deactivation of TADF altogether [170]. In our case, the beneficial properties of rigidification are in line with the observations in this work [165]. Most likely driven by the denser packing a more orthogonal D-A angle leads to a lower ΔE_{ST}, higher k_{rISC} and higher τ_s. Assuming the equilibrium picture between k_{rISC} and k_{ISC}, their ratio can be expressed as [166] :

$$\frac{k_{rISC}}{k_{ISC}} = \frac{1}{3}\exp\left(\frac{-\Delta E_{ST}}{k_B T}\right) \qquad \text{eq.3}$$

Considering the experimental values of ΔE_{ST}, 0.13 for **3CzTrz** and 0.10 for **3tCzTrz**, and using equation 3, k_{rISC} should increase from 6.0x10^4 s^{-1} to around 2.0x10^5 s^{-1} when ΔE_{ST} changes from 0.13 to 0.10. The predicted value of k_{rISC} is close to the modeled value of 1.9x10^5 s^{-1}, indicating that ΔE_{ST} is the main driver behind the increase in k_{rISC}. It is worth mentioning that previous work showed that controlling the spatial overlap between HOMO and LUMO, as is done by changing the D-A angle, in fact leads to less non-radiative singlet decay [169]. While this is not taken into account in our analysis, we cannot exclude that it contributes to the increased PLQY of 3tCzTrz as well.

5.3 Conclusion

In this work, we study the photophysical properties of tert-butylation on a blue TADF emitter. We find through modelling of the TrPL curves that adding a tert-butyl group is associated with two positive effects: it increases the value of rISC, plus it reduces the non-radiative triplet decay constant. By diluting our tert-butylated emitter in a PS host we are able to obtain 100% PLQY, i.e., completely suppress the non-radiative triplet decay. We expect the trend found in this study to continue for other materials, but the magnitude of this effect will likely vary between emitters. Structure property relationships, like the one established in this paper, are

extremely useful in the design of new high-performance and solution processable TADF emitters.

Chapter 6 : Flexible, Transparent, and Solution Processable Electrode for Photosynthetic Biohybrid Electronic Devices

Photosynthetic biohybrid devices have shown tremendous potential for various applications including renewable energy and biomedical devices. However, the conventional rigid electrodes used in these systems suffer from limitations such as brittleness and high fabrication costs. Designing flexible electrodes that are compatible with photosynthetic proteins can benefit applications in various fields, ranging from e.g. renewable energy to biomedical devices. This study aims to broaden the present state of the art biohybrid devices by introducing a flexible nanostructured and transparent electrode, thereby enabling a wider range of potential applications. In this study, we fabricated a silver nanowire (AgNW) meshwork as a photocathode with tunable transparency, which is used to interface directly to a reaction center light-harvesting complex-1 (RC-LH1) isolated from Rhodobacter sphaeroides, a purple photosynthetic bacterium. The resulting biohybrid device yields a peak photocurrent of 177 µW cm^{-2}, and a stable photocurrent of 152 µW cm^{-2} at 55 % transparency of the electrode with 48 mW cm^{-2} irradiance. Our work demonstrates that a flexible AgNW electrode can be utilized for biohybrid devices with facile fabrication and tunable transparency.

Kalyani Thakur, Vincent Friebe, Michael R. Jones, Paul W.M Blom and Charusheela Ramanan, Photosynthetic reaction center-based bio-photovoltaic on a flexible nanostructured electrode. (Manuscript completed)

6.1 Introduction

Biohybrid devices based on photosynthetic proteins [173], such as biophotovoltaics [174], biosensors, photocell and photomemory devices [175] have shown tremendous potential in fields including renewable energy as well as biomedical applications. Photosynthetic proteins have also been demonstrated in self-powered sensory devices such as electronic skin [176] and they have the potential to be used in wearable electronics, which requires a flexible transparent electrode compatible with photosynthetic proteins. The popularity of photosynthetic protein for the use in bioelectronics is due to their high quantum efficiency (charges separated per absorbed photon) of the photoproteins, which is close to 100% [177–181]. Moreover, the abundance of the photosynthetic protein in nature makes them an excellent alternative to present conventional energy sources. Several efforts have been made to harness this highly efficient charge separation process of RCs into biohybrid devices [176,182–190]. Despite the high quantum yield of RCs, typical photocurrents in the range of a few nA to mA cm^{-2} [191,192] have been observed so far. The latest development in the transparent electrode in biohybrid devices has used inverse opal mesoporous ITO, otherwise known as IO-mITO. The highest photocurrent of 4.6 mA cm^{-2} has been reported using IO-mITO-based electrodes, attributed to substantial protein loading and light penetration [192].

Despite ITO or ITO derivatives often being the electrode of choice due to their beneficial properties in terms of transparency and conductance, ITO suffers from some serious drawbacks. There exists a scarcity in supply, leading to high fabrication costs, and it is a brittle material [193]. In fact, most of the studies, to the best of our knowledge, have been done on solid electrodes, which make mass production and its integration into applications such as wearable electronics difficult [194–197]. To overcome this drawback, transparent flexible electrodes provide an attractive alternative. Their applicability has already been demonstrated in other fields, like organic electronics, where flexible electrodes have been used as a transparent anodes in organic solar cells and organic light-emitting diodes [196,198]. Furthermore flexible and stretchable electrodes have been successfully employed in the biomedical field due to their ability to integrate with soft, deformable, and biological materials [199–201].

These biohybrid devices are most commonly created by coupling the RCs to a conducting electrode, and the efficiency of such devices are often limited by many other factors, such as the wiring of photoprotein to the electrode, which affects protein loading, insufficient light absorption, stability of the photoelectrode, and the rate of electron transfer between photoprotein and electrode. Enhancing the electron transfer rate between the RC of a photosynthetic proteins and an electrode is a significant challenge in creating efficient biohybrid devices. Several efforts have been made to improve the performance of these biohybrid devices. For example, the wiring of protein is explored through electrostatic adsorption, covalent binding, affinity binding, and plugging to apoprotein into the electrode [202–212]. Similarly, the stability of the protein and light absorption is improved by switching from planar to nanostructured electrodes, thereby enhancing the light absorption through exploiting the plasmonic effect. For example, in one study [205], Friebe et al. demonstrated that switching from a planar silver electrode to a mesoporous rough silver electrode improves the photocurrent density from 6.1 μA cm^{-2} to 166 μA cm^{-2}, with 2.5 fold plasmonic enhancement of light per RC-LH1 complex. Integrating a suitable metallic nanostructure into a biohybrid not only expands the optical absorption region but also enhances photon absorption capacity through localized surface plasmon resonance [213]. According to several studies, where gold and silver islands were coupled with a light-harvesting complex, a 20-fold enhancement of fluorescent emission was observed [214–218]. In another study, hybrid systems of nanoparticles with photosystem-I demonstrated increased light absorption over the entire region [219]. However, very few reports study the rate of electron transfer between electrode and protein. In-situ, transient absorption spectroscopy can be employed to probe the electron transfer rate, but this technique requires a transparent electrode and robust biohybrid devices.

In order to realize the commercialization of biohybrid devices, fabrication should be quick, uncomplicated, and ideally easy to scale up as well. In this work, we have successfully fabricated a flexible and transparent bio-photoelectrode by integrating a silver nanowire (AgNW) meshwork onto a polyethylene naphthalate (PEN) substrate and demonstrate its applicability using biophotovoltaics. The transparency of the electrode can be easily tuned by controlling the amount of AgNW solution sprayed on the electrode. This flexible electrode is

combined with a photosynthetic bacterial RC using direct immobilization to create a photoelectrode. We achieved a peak photocurrent of 177 μW cm^{-2} and a stable photocurrent of 152 μW cm^{-2}, using a biohybrid photovoltaics device with a AgNW electrode. The electrode has 55 % transparency and is illuminated with 48 mW cm^{-2} irradiance at 870 nm. The nanostructured AgNW photoelectrode showed good compatibility with the protein and improved stability owing to the plasmonic effect of AgNW's meshwork [220–222]. We thus demonstrated a promising pathway toward developing flexible and transparent bioelectronics.

6.2 Results and discussion

Fabrication and characterization of the electrode

Fabrication of the AgNW electrode is done via spray coating. Spray coating offers several advantages over conventional methods such as spin coating. It provides a more uniform and controlled film thickness. Spray coating process is compatible with various substrate types, including flexible and irregular surfaces, making is suitable for PEN substrate used in this study. Additionally, the fine mist of droplets ensures better wetting and contact with the substrate, resulting in improved film adhesion and homogeneity. This facile method holds strong potential for up-scaling, , making it suitable for large-area coating applications and furthermore provides the flexibility to fabricate desired patterns on a substrate. AgNW electrode with different transparency was fabricated by spraying different volumes of AgNWs dispersion on a PEN substrate. The schematic diagram of spray coating technique and fabricated electrode is shown in the Figure 6.1 (a). The electrode is then characterized by measuring absorption spectrum, transmittance and sheet resistance.

Figure 6.1 (b) shows the normalized absorption spectrum (in green) of the AgNW electrode plotted along with the absorption spectrum of the AgNW dispersion (in red) in isopropanol. The spectra exhibit two characteristic absorption peaks at 351 nm and 377 nm. These are assigned to plasmon resonance absorption attributed to the transversal and quadruple resonance mode of AgNW with a pentagonal cross-section [223]. The absorption spectrum of our fabricated electrode is depicted by the line in green exhibits the same characteristic peaks of AgNW, essentially confirming the successful fabrication of the electrode. However, these

peaks are red-shifted, and the relative intensity of the two peaks is reversed in the film. The suppressed intensity of quadruple mode on the electrode can be attributed to the spatial constraints and alignment of the AgNWs on the electrode surface, restricting the efficient excitation and detection of the quadruple mode vibrations perpendicular to the electrode plane compared to transversal mode where the vibrations are confined within the plane of the electrode.

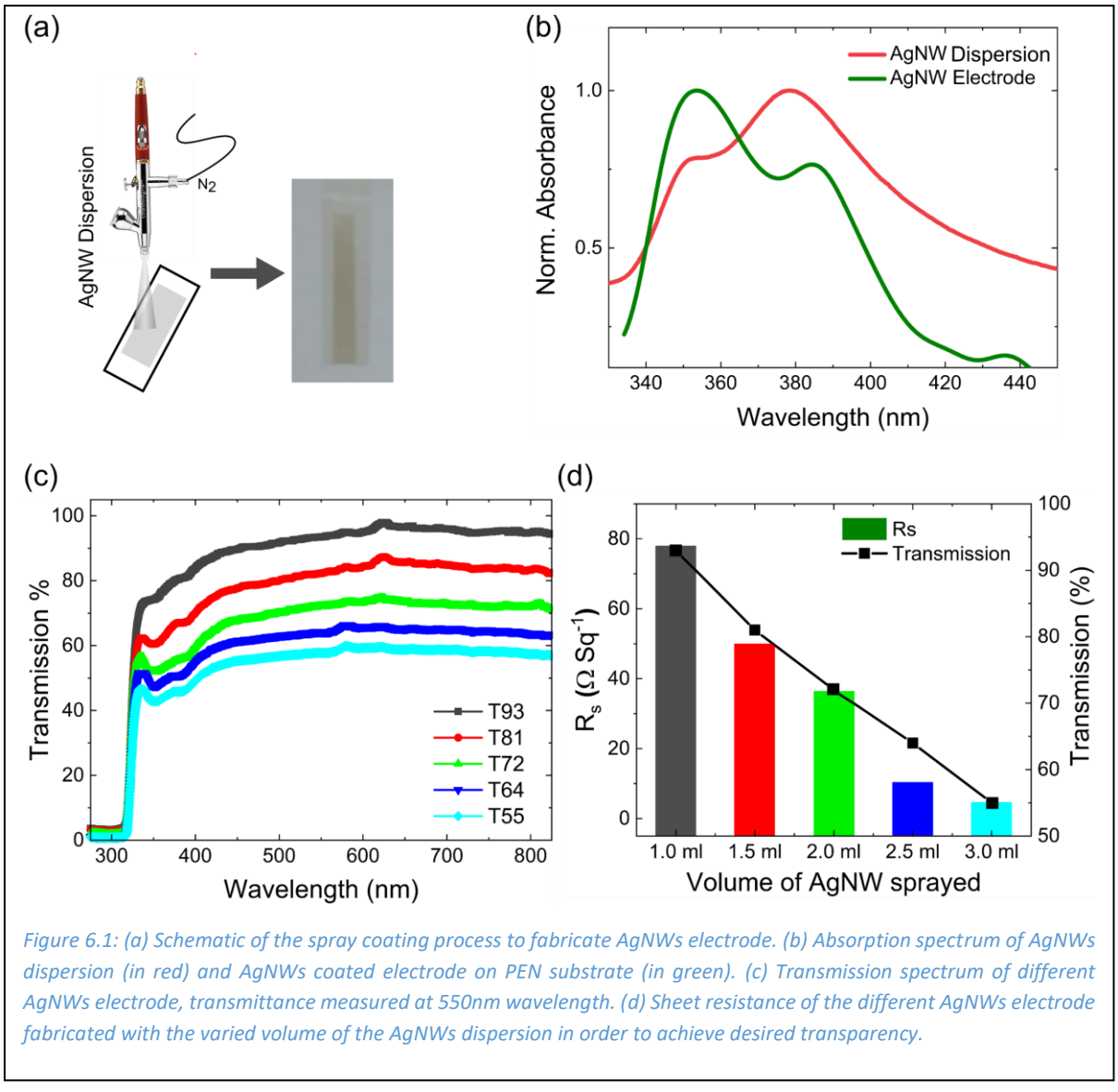

Figure 6.1: (a) Schematic of the spray coating process to fabricate AgNWs electrode. (b) Absorption spectrum of AgNWs dispersion (in red) and AgNWs coated electrode on PEN substrate (in green). (c) Transmission spectrum of different AgNWs electrode, transmittance measured at 550nm wavelength. (d) Sheet resistance of the different AgNWs electrode fabricated with the varied volume of the AgNWs dispersion in order to achieve desired transparency.

Furthermore, sheet resistance of film reduced substantially as the transparency of the film increased as shown in Figure 6.1(c)-(d). This led to an increase in the conductivity since sheet resistance is inversely proportional to conductivity of the electrode. The electrode that gave the best photocurrent is obtained with a concentration of 0.5 mg ml^{-1}, a 10 cm nozzle to substrate distance at 1.8 bar pressure with 3 ml of sprayed volume. There exists an inherent

trade-off between transparency and sheet resistance, but a further increase in sprayed volume leads to decreased adhesively of the silver nanowire film on the substrate. We aimed for an electrode that produced the best photocurrent while at the same time retaining robustness during device fabrication.

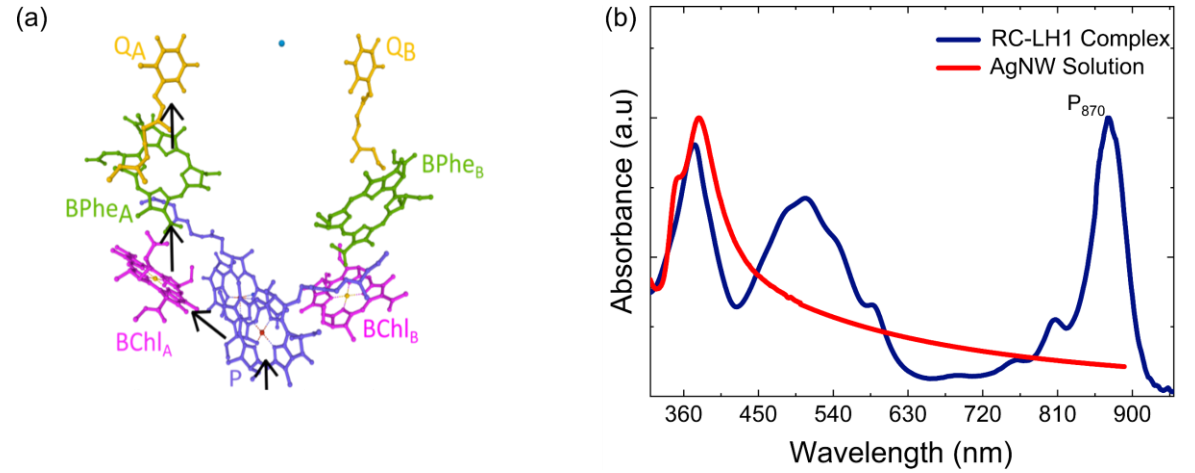

Figure 6.2: (a) Structure of RC derived from RC-LH1 complex of Rhodocabter sphaeroides. (b) Absorption spectrum of RCLH1 complex in the Tris buffer in blue and AgNW in isopropyl alcohol in the red. The absorption spectrum of AgNWs dispersion overlaps with the soret band of bacteriochlorophyll.

The biohybrid nanostructured photocathode is prepared by drop-casting RC-LH1 (extracted from the purple bacteria *Rhodobacter sphaeroides*) protein onto the AgNW electrode, followed by rinsing in the buffer solution to remove excess protein. The RC of the RC-LH1 complex consists of four main cofactors: four bacteriochlorophylls (BChl), two bacteriopheophytins (BPhe), two ubiquinones, and one non-heme iron, as shown in Figure 6.2a. Two out of four BChl form a dimer called special pair P (P_{870}) and the remaining cofactors are arranged symmetrically on both sides of P in two branches named A and B [224]. The two branches are symmetrical, but they differ in the protein environment around the cofactors. This makes one branch more conducive to electron flow than the other. The absorption spectrum of the complex (Figure 6.2b) extends from the UV region to the near IR and consists of multiple peaks arising from the different cofactors. The highest intensity peak at 870 nm arises from the special pair P, while the bands at 806 nm and 585 nm are due to monomeric BChl. The BPhe has an absorption band around 760 nm and 545 nm. The broad peak from 430 -560 nm are assigned to the carotenoid's absorption. Finally, the peak at 370 nm is the Soret band absorption of bacteriochlorin [225]. The plasmonic peaks of the AgNWs coincide with

the Soret band of the RCLH1 complex in the UV region. This overlap is crucial for the plasmonic interaction between the AgNW nanostructure and the protein [218,226,227]

Biohybrid device fabrication

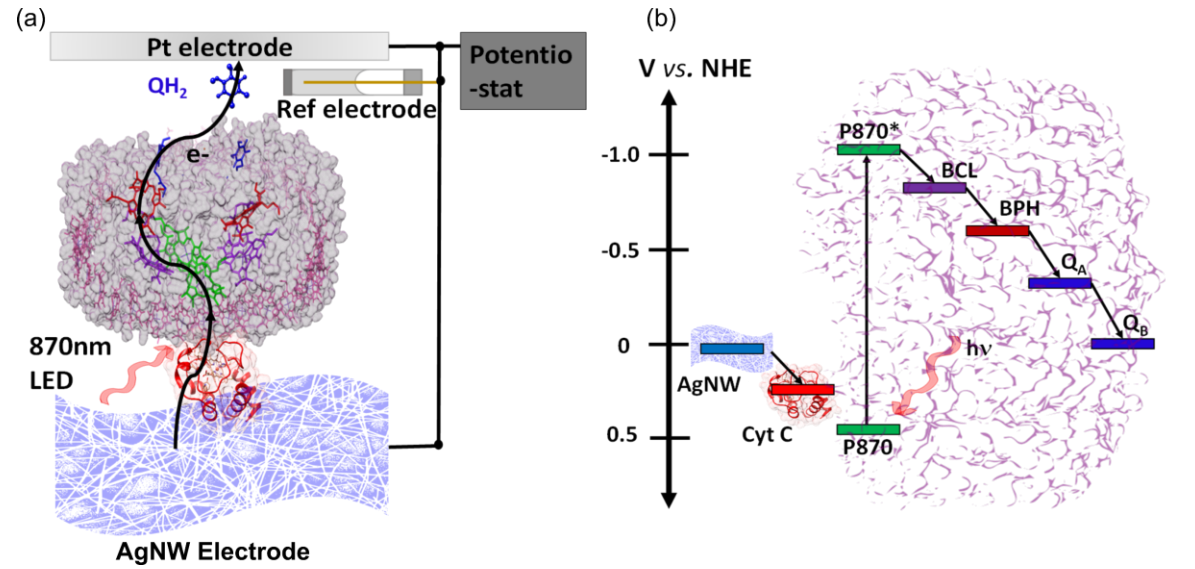

Figure 6.3: (a) Schematics of biohybrid device of RCLH1 complex wired via Cyt C to flexible transparent AgNWs electrode in a electrochemical cell consisting of Pt counter electrode and Ag/AgCl (3M KCl) reference electrode connected to the potentiostat. (b) Energy diagram of electron transfer mechanism.

Figure 6.3a shows a schematic of the full biohybrid device consisting of a flexible transparent AgNW electrode fabricated on a PEN substrate [51]. The protein-coated AgNW electrode is used as a working electrode (photocathode) into a three-electrode configuration electrochemical cell. The electrolyte solution consists of ubiquinone-0 and cytochrome c, which acts as an electron mediator between the electrode and protein. Cytochrome c acts as an electron donor, whereas the water-soluble ubiquinone-0 acts as an electron acceptor from the protein [229]. The biohybrid device is placed in an electrochemical cell with Ag/AgCl (3M KCl) as a reference electrode and a platinum wire (Pt) as a counter electrode, establishing the connection to the RC-LH1 complex via cytochrome c [229] and ubiquinone-0 [230]. The whole setup is attached to the potentiostat, and all the photocurrent measurement is done at the same bias voltage of -75 mV. A monochromatic LED with a center wavelength of 870 nm is used for photoexcitation of the electrode. Upon illumination of the working electrode, the special pair P of the RC-LH1 complex is excited to the higher energy state P*. Due to the highly reducing nature of P* [231], it oxidizes its cofactor via sequential electron transfer, i.e., reducing monomeric bacteriochlorophyll (BChl), bacteriopheophytins (BPhe), ubiquinone Q_A

to ubiquinone Q_B as shown in the energy band diagram in Figure 6.3b. The electron is further captured by external ubiquinone $Q_{0,}$ which then diffuses in the electrolyte to counter electrode. The oxidized P+ is reduced by cytochrome c, which in turn knocks out an electron from the AgNW electrode to complete the cycle, and thus current flows in the electrochemical cell.

Photocurrent Measurement

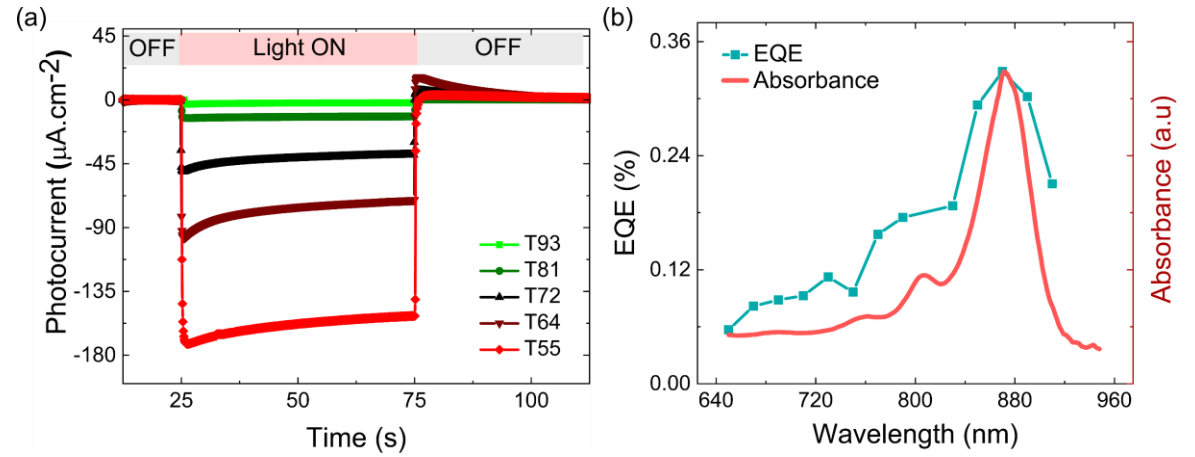

Figure 6.4: (a) Photocurrent density of RCLH1 adsorbed AgNWs biohybrid at different transparency. The highest photocurrent obtained with the electrode with 55% transparency. (b) External quantum efficiency of the AgNWs-RCLH1 biohybrid. The EQE at 870nm reaches to 32%

Figure 6.4a shows the photocurrent measurement of the biohybrid device fabricated using AgNW electrodes having various transparency. Figure 6.4 shows a peak photocurrent of 10 μW cm^{-2} immediately after the LED light is turned ON, with the electrode having 93% transparency at the applied bias voltage of – 75 mV. Upon switching OFF the light, the current reduces to zero. This suggests that the RC-LH1 complex is responsible for the observed photocurrent from the device. To further confirm that the photocurrent originated from the RC-LH1 complex protein, we measured wavelength-dependent external quantum efficiency (EQE), calculated by measuring the photocurrent at each excitation wavelength using the formula described in the following reference [232]. The obtained photocurrent EQE follows the absorption spectrum of the RC-LH1 complex, as shown in Figure 6.4b, confirming the complex as the source of the current [233]. Furthermore, we could increase the amount of photocurrent density by tuning the transparency of the electrode. The peak photocurrent increases from 10 μW cm^{-2} with a 93% transparent electrode to 177 μW cm^{-2} with a 55 % transparent electrode. We hypothesize that this improvement in photocurrent is due to the

improvement in conductivity of the AgNW electrode, as indicated by sheet measurements of the electrode at various transmissions (Figure 6.1b). Furthermore, the peak photocurrent observed with a semi-transparent electrode stabilizes to 152 µW cm^{-2} during 50 s illumination. The observed photocurrent measurement is reproduced with three cycles of light illumination (cathodic cycle), giving the same current level, as shown in

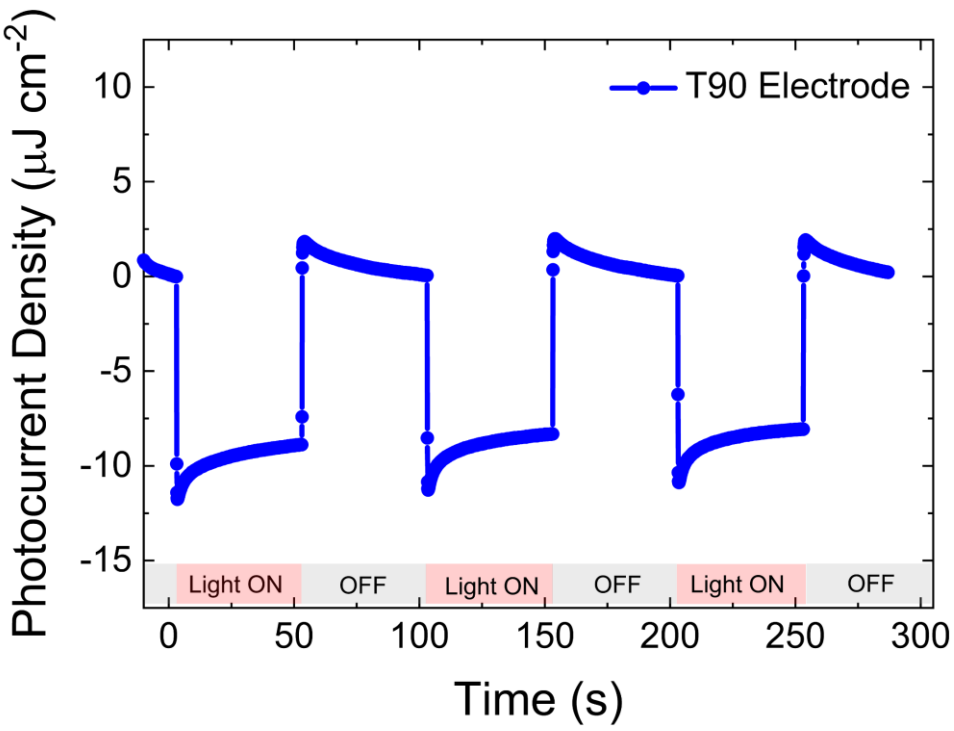

Figure 6.5: Photocurrent density of RCLH1 adsorbed AgNWs biohybrid electrode with 90% transparency (T90) for the three ON/OFF light illumination cycle of 50s each.

Figure 6.5. A reverse anodic photocurrent is also obtained upon switching off the excitation light, which decays to zero. This anodic current is observed due to the dissipation of the accumulated charge around the electrode during the cathodic cycle. However, the amount of anodic current is diffusion-limited and varies from system to system [202,205,234,235].

Comparing the photocurrent obtained from the semi-transparent AgNW electrode with other silver metal electrodes, we find that the obtained photocurrent is comparable to the photocurrent of 166 µW cm^{-2} reported for the rough silver [205]. However, rough silver is 90% reflective, which means that a photon can be absorbed both during illumination and reflection by the metal electrode. Moreover, in the case of rough silver, the current decays to a plateau value of 80 µW $cm^{-2,}$ which is significantly lower than the 152 µW cm^{-2} of our AgNW nanostructured electrodes [205]. Our average photocurrent obtained from the AgNW is the

highest stable photocurrent reported for the RC-LH1 biohybrid system fabricated on the flexible transparent electrode. However, it still lags behind the highest reported photocurrent for RC-LH1, namely 4.6 mA cm^{-2} [192], obtained with a rigid electrode involving several cycles of the protein coating.

6.3 Conclusion

In this study, we have successfully fabricated a flexible transparent electrode using silver nanowires (AgNW) that exhibits great potential for utilization in bioelectronic and wearable electronic devices, based on photosynthetic proteins. We have demonstrated the applicability of this electrode by integrating it into biohybrid photovoltaic devices using an RCLH1 protein complex derived from the *Rhodobacter Sphearoides* as an active component. The nanostructuring electrode increases the effective surface area of the electrode, which improves protein loading and allows the protein to be adsorbed directly onto the surface of the electrode. Furthermore, the plasmonic interaction improves the photocurrent by enhancing light absorption. A photocurrent of 177 µW cm^{-2} is obtained with a semi-transparent AgNW electrode, and our stable photocurrent of 152 µW cm^{-2} even presents a 2-fold improvement over the photocurrent obtained with a rigid silver electrode. We preserve the intricate light-harvesting functionality of the biological RC while at the same time boosting the photocurrent of our biohybrid device using the plasmonic effect. The flexible transparent AgNW electrode offers a promising solution for the development of advanced bioelectronics, enabling efficient energy conversion and signal transduction. Its flexibility, transparency, and compatibility with photosynthetic proteins make it a as a promising candidate for industrial applications and the realization of sustainable and high-performance bioelectronics devices.

6.4 Experimental section

Materials

RCLH1 complex from the UK Bristol University. Ubiquinone-0 and horse-heart cytochrome c is purchased from Sigma Aldrich. The AgNW network dispersed in propanol is purchased from ACS material.

Electrode fabrication

For the purpose of electrode fabrication, the AgNW solution dispersed in isopropanol was purchased from ACS materials. The solution had a concentration of 20 mg ml^{-1}, with an average wire diameter of 50 nm. The solution of AgNW was first diluted with isopropanol to the various concentrations and then sprayed on a preheated 1x3 cm PEN substrate using an Infinity CR plus 2 airbrush under an N_2-assisted inlet with a pressure of 1.8 bar, as shown in Figure 6.1(a). The distance between the nozzle and the substrate was fixed at 11 cm, and the substrate was continuously heated during the spraying process. Finally, the film is annealed at 100 °C in a vacuum oven overnight to evaporate solvent residue and to improve the connectivity of silver wires in the film. The various parameters, like concentration, pressure, volume, and the distance between the nozzle to the substrate, are optimized as described in another paper [196].

Photochronoamperometry

RCLH1 protein is drop-casted on the AgNW electrode of different transmissions, with the protein of OD 80 in the dark at 4°C for 15 minutes. The electrode is then rinsed with Tris buffer (20 mM, pH 8.0) several times to wash away excess non-wired protein. The protein-coated electrode is used as a working electrode in the electrochemical cell along with Ag/AgCl as a reference electrode and a platinum wire as a counter electrode, which is connected to a potentiostat from Plamsens4. The working solution consists of 1.5 mM ubiquinone-0 and 200 uM cytochrome c in 20 mM Tris buffer of pH 8.0. A monochromatic 870 nm LED (LaserRoithner Technik) is used for illumination with an irradiance of 48 mW cm^{-2} at the surface of the electrode.

Steady-state absorption

The absorption measurement is done with a home-built setup consisting of a helium deuterium lamp (DH-2000, Ocean Optics) which is connected to the sample holder via an optical fiber cable for incident light and collection of the transmitted light. The spectrometer

(34000-UV-VIS-ES, Ocean Optics) is used for the detection of the transmitted light from the sample, which is then viewed using the ocean view software.

Sheet resistance measurement

The sheet resistance measurement is performed using a four-probe technique with a probe spacing of 0.635 mm, Rs= 4.323*V/I, connected to a Keithley 2700 Multimeter.

Action spectra and external quantum efficiency

The action spectra are performed in the electrochemical cell. For the monochromatic excitation, a regenerative 1030 nm amplifier laser (Pharos, Light Conversion) coupled with an optical parametric amplifier (Light Conversion) is used to generate different excitation wavelengths from 650 nm to 910 nm.

Reference

[1] W. Barford, *Electronic and Optical Properties of Conjugated Polymers* (Oxford University Press, 2005).

[2] S. Schols, *Device Architecture and Materials for Organic Light-Emitting Devices* (Springer Netherlands, Dordrecht, 2011).

[3] S.-H. Kim and Y.-A. Son, *Near-Infrared Dyes*, in *Handbook of Textile and Industrial Dyeing*, Vol. 1 (Elsevier, 2011), pp. 588–603.

[4] A. Köhler and H. Bässler, *The Electronic Structure of Organic Semiconductors*, Electron. Process. Org. Semicond. 1 (2015).

[5] T. A. Albright, J. K. Burdett, and M.-H. Whangbo, *Orbital Interactions in Chemistry* (John Wiley & Sons, Inc., Hoboken, NJ, USA, 2013).

[6] J. Clayden, N. Greeves, and S. Warren, *Organic Chemistry* (Oxford University Press Inc., New York, 1133., 2001).

[7] *UV-Visible Absorption Spectra*, https://www.chemguide.co.uk/analysis/uvvisible/theory.html#top.

[8] E. N. Koukaras and A. M. : 198, Fermi's Golden Rule, n.d.

[9] P. Atkins and R. Friedman, *Molecular Quantum Mechanics*, 4th ed. (Oxford University Press, 1997).

[10] J. Gibson, A. P. Monkman, and T. J. Penfold, *The Importance of Vibronic Coupling for Efficient Reverse Intersystem Crossing in Thermally Activated Delayed Fluorescence Molecules*, ChemPhysChem 2956 (2016).

[11] J. Franck, *Elementary Processes of Photochemical Reactions*, Trans. Faraday Soc. **21**, 536 (1926).

[12] E. Condon, *A Theory of Intensity Distribution in Band Systems*, Phys. Rev. **28**, 1182 (1926).

[13] A. Jablonski, *Efficiency of Anti-Stokes Fluorescence in Dyes*, Nature **131**, 839 (1933).

[14] H. H. Jaffé and A. L. Miller, *The Fates of Electronic Excitation Energy*, J. Chem. Educ. **43**, 469 (1966).

[15] E. B. Priestley and A. Haug, *Phosphorescence Spectrum of Pure Crystalline Naphthalene*, J. Chem. Phys. **49**, 622 (1968).

[16] A. Monkman, *Photophysics of Thermally Activated Delayed Fluorescence*, Highly Effic. OLEDs Mater. Based Therm. Act. Delayed Fluoresc. 425 (2018).

[17] J. Frenkel, *On the Transformation of Light into Heat in Solids. I*, Phys. Rev. **37**, 17 (1931).

[18] S. R. Forrest, *The Path to Ubiquitous and Low-Cost Organic Electronic Appliances on Plastic*, Nature.

[19] G. Li, R. Zhu, and Y. Yang, *Polymer Solar Cells*, Nature Photonics.

[20] G. H. Wannier, The Structure of Electronic Excitation Levels in Insulating Crystals, 1937.

[21] L. Papadopoulas, Unlocking New Principles of Singlet Fission: Characterization, Optimization, and Identification of Novel Singlet Fission Materials, 2021.

[22] T. Förster, *Zwischenmolekulare Energiewanderung Und Fluoreszenz*, Ann. Phys. **437**, 55 (1948).

[23] D. L. Dexter, *A Theory of Sensitized Luminescence in Solids*, J. Chem. Phys. **21**, 836 (1953).

[24] F. Strieth-Kalthoff, M. J. James, M. Teders, L. Pitzer, and F. Glorius, *Energy Transfer Catalysis Mediated by Visible Light: Principles, Applications, Directions*, Chem. Soc. Rev. **47**, 7190 (2018).

[25] I. Rörich, Influence of Energetic Disorder on Exciton Diffusion Properties, 2018.

[26] B. Wallace and P. J. Atzberger, *Förster Resonance Energy Transfer: Role of Diffusion of Fluorophore Orientation and Separation in Observed Shifts of FRET Efficiency*, PLoS One **12**, (2017).

[27] Bernhard Dick and Bernhard Nickel, *ACCESSIBILITY OF THE LOWEST QUINTET STATE OF ORGANIC MOLECULES THROUGH TRIPLET-TRIPLET ANNIHILATION; AN INDO Cl STUDY*, Chem. Phys. **78**, 1 (1983).

[28] E. Vauthey, *Photoinduced Symmetry-Breaking Charge Separation*, ChemPhysChem **13**, 2001 (2012).

[29] R. A. Marcus, On the Theory of Oxidation-Reduction Reactions Involving Electron Transfer. I*, 1956.

[30] A. Weller, *Photoinduced Electron Transfer in Solution: Exciplex and Radical Ion Pair Formation Free Enthalpies and Their Solvent Dependence*, Zeitschrift Fur Phys. Chemie **133**, 93 (1982).

[31] D. Rehm and A. Weller, *Kinetics of Fluorescence Quenching by Electron and H-Atom Transfer*, Isr. J. Chem. **8**, 259 (1970).

[32] J. R. Miller, *Intramolecular Long-Distance Electron Transfer in Radical Anions. The Effects of Free Energy and Solvent on the Reaction Rates1*, J. Am. Chem. Soc. **106**, 3047 (1984).

[33] P. W. M. Blom, N. I. Craciun, D. M. De Leeuw, G. A. H. Wetzelaer, H. T. Nicolai, and M. Kuik, *25th Anniversary Article: Charge Transport and Recombination in Polymer Light-Emitting Diodes*, Adv. Mater. **26**, 512 (2014).

[34] M. Kamran, J. D. Delgado, V. Friebe, T. J. Aartsma, and R. N. Frese, *Photosynthetic Protein Complexes as Bio-Photovoltaic Building Blocks Retaining A High Internal Quantum Efficiency*, Biomacromolecules **15**, 2833 (2014).

[35] R. A. Voloshin, S. M. Shumilova, E. V. Zadneprovskaya, S. K. Zharmukhamedov, S. Alwasel, H. J. M. Hou, and S. I. Allakhverdiev, *Photosystem II in Bio-Photovoltaic Devices*, Photosynthetica **60**, 121 (2022).

[36] J. Shah, *Ultrafact Spectroscopy of Semiconductors and Semiconductor Nanostructures* (springer Seriers in SOLID_STATE SCIENCES, 1999).

[37] A. Weu, Investigating the Photophysics and Stability of Organic Photovoltaics Using Ulstrafast Spectroscopy, 2019.

[38] S. Fede, *Recent Developments in Compact Ultrafast Lasers*, Nature **424**, 831 (2003).

[39] W. T. Silfvast, *Laser Fundamentals: Second Edition* (2004).

[40] R. Ell, U. Morgner, F. X. Kãârtner, J. G. Fujimoto, E. P. Ippen, V. Scheuer, G. Angelow, T. Tschudi, M. J. Lederer, A. Boiko, and B. Luther-Davies, *Generation of 5-Fs Pulses and Octave-Spanning Spectra Directly from a Ti:Sapphire Laser.*, Opt. Lett. **26**, 373 (2001).

[41] D. Strickland and G. Mourou, *Compression of Amplified Chirped Optical Pulses*, Opt. Commun. **55**, 447 (1985).

[42] R. A. Baumgartner, R. Byer, and A. S.-O. N. Interactions, *Optical Parametric Amplification*, Quantum **QE**-**15**, 432 (1979).

[43] C. Manzoni and G. Cerullo, *Design Criteria for Ultrafast Optical Parametric Amplifiers*, J. Opt. **18**, 103501 (2016).

[44] A. Mokhtari, P. Cong, J. L. Herek, and A. H. Zewail, *Direct Femtosecond Mapping of Trajectories in a Chemical Reaction*, Nature **348**, 225 (1990).

[45] A. H. Zewail, *Femtochemistry: Atomic-Scale Dynamics of the Chemical Bond*, J. Phys. Chem. A **104**, 5660 (2000).

[46] R. Berera, R. van Grondelle, and J. T. M. Kennis, *Ultrafast Transient Absorption Spectroscopy: Principles and Application to Photosynthetic Systems*, Photosynth. Res. **101**, 105 (2009).

[47] C. Ruckebusch, M. Sliwa, P. Pernot, A. de Juan, and R. Tauler, *Comprehensive Data Analysis of Femtosecond Transient Absorption Spectra: A Review*, J. Photochem. Photobiol. C Photochem. Rev. **13**, 1 (2012).

[48] I. H. M. Mullen, Katharine M; van Stokkum, *TIMP: An R Package for Modeling Multi-Way Spectroscopic Measurements*, J. Stat. Softw. **18**, 1 (2007).

[49] J. J. Snellenburg, S. Laptenok, R. Seger, K. M. Mullen, and I. H. M. van Stokkum, *Glotaran: A Java-Based Graphical User Interface for the R Package TIMP*, J. Stat. Softw. **49**, 1 (2012).

[50] I. H. M. van Stokkum, D. S. Larsen, and R. van Grondelle, *Global and Target Analysis of Time-Resolved Spectra*, Biochim. Biophys. Acta - Bioenerg. **1657**, 82 (2004).

[51] C. Biskup, T. Zimmer, and K. Benndorf, *FRET between Cardiac Na+ Channel Subunits Measured with a Confocal Microscope and a Streak Camera*, Nat. Biotechnol. **22**, 220

(2004).

[52] P. Pander, P. Data, and F. B. Dias, *Time-Resolved Photophysical Characterization of Triplet-Harvesting Organic Compounds at an Oxygen-Free Environment Using an ICCD Camera*, J. Vis. Exp. **2018**, 0 (2018).

[53] A. Nevin, A. Cesaratto, S. Bellei, C. D'Andrea, L. Toniolo, G. Valentini, and D. Comelli, *Time-Resolved Photoluminescence Spectroscopy and Imaging: New Approaches to the Analysis of Cultural Heritage and Its Degradation*, Sensors **14**, 6338 (2014).

[54] D. Graves, V. Jankus, F. B. Dias, and A. Monkman, *Photophysical Investigation of the Thermally Activated Delayed Emission from Films of M-MTDATA:PBD Exciplex*, Adv. Funct. Mater. **24**, 2343 (2014).

[55] M. R. Wasielewski, *Photoinduced Electron Transfer in Supermolecular Systems for Artifical Photosynthesis*, Chem. Rev. **92**, 435 (1992).

[56] C. Ramanan, C. H. Kim, T. J. Marks, and M. R. Wasielewski, *Excitation Energy Transfer within Covalent Tetrahedral Perylenediimide Tetramers and Their Intermolecular Aggregates*, J. Phys. Chem. C **118**, 16941 (2014).

[57] M. Yu, R. Huang, J. Guo, Z. Zhao, and B. Z. Tang, *Promising Applications of Aggregation-Induced Emission Luminogens in Organic Optoelectronic Devices*, PhotoniX **1**, 1 (2020).

[58] A. C. Jakowetz, M. L. Böhm, A. Sadhanala, S. Huettner, A. Rao, and R. H. Friend, *Visualizing Excitations at Buried Heterojunctions in Organic Semiconductor Blends*, Nat. Mater. **16**, 551 (2017).

[59] J. Zhang, X. Zhao, H. Shen, J. W. Y. Lam, H. Zhang, and B. Z. Tang, *White-Light Emission from Organic Aggregates: A Review*, Adv. Photonics **4**, 1 (2022).

[60] W. Liang, S. He, and J. Fang, *Self-Assembly of J-Aggregate Nanotubes and Their Applications for Sensing Dopamine*, Langmuir **30**, 805 (2014).

[61] C. M. Pochas, K. A. Kistler, H. Yamagata, S. Matsika, and F. C. Spano, *Contrasting Photophysical Properties of Star-Shaped vs Linear Perylene Diimide Complexes*, (2013).

[62] M. R. Wasielewski, *Self-Assembly Strategies for Integrating Light Harvesting and Charge Separation in Artificial Photosynthetic Systems*, Acc. Chem. Res. **42**, 1910

(2009).

[63] Ö. Birel, *A Review on Perylene-3,4,9,10-Tetracarboxylic Acid Diimide Molecules*, Celal Bayar Üniversitesi Fen Bilim. Derg. **13**, 379 (2017).

[64] F. Würthner, C. R. Saha-Möller, B. Fimmel, S. Ogi, P. Leowanawat, and D. Schmidt, *Perylene Bisimide Dye Assemblies as Archetype Functional Supramolecular Materials*, Chem. Rev. **116**, 962 (2016).

[65] E. Kozma and M. Catellani, *Perylene Diimides Based Materials for Organic Solar Cells*, Dye. Pigment. **98**, 160 (2013).

[66] S. Chen, P. Slattum, C. Wang, and L. Zang, *Self-Assembly of Perylene Imide Molecules into 1D Nanostructures: Methods, Morphologies, and Applications*, Chem. Rev. **115**, 11967 (2015).

[67] S. Samanta, S. K. Ray, S. Deolka, S. Saha, P. K. R., R. Bhowal, N. Ghosh, and D. Chaudhuri, *Safeguarding Long-Lived Excitons from Excimer Traps in H-Aggregated Dye-Assemblies*, Chem. Sci. **11**, 5710 (2020).

[68] S. Samanta and D. Chaudhuri, *Suppressing Excimers in H-Aggregates of Perylene Bisimide Folda-Dimer: Role of Dimer Conformation and Competing Assembly Pathways*, Journal of Physical Chemistry Letters.

[69] A. Oleson, T. Zhu, I. S. Dunn, D. Bialas, Y. Bai, W. Zhang, M. Dai, D. R. Reichman, R. Tempelaar, L. Huang, and F. C. Spano, *Perylene Diimide-Based Hj- And HJ-Aggregates-And Prospect of Exciton Band Shape Engineering in Organic Materials*, J. Phys. Chem. C **123**, 20567 (2019).

[70] H. Song, H. Zhao, Y. Guo, A. M. Philip, Q. Guo, M. Hariharan, and A. Xia, *Distinct Excited-State Dynamics of Near-Orthogonal Perylenimide Dimer: Conformational Planarization versus Symmetry Breaking Charge Transfer*, (2019).

[71] Y. Hong, W. Kim, T. Kim, C. Kaufmann, H. Kim, F. Würthner, and D. Kim, *Real-time Observation of Structural Dynamics Triggering Excimer Formation in a Perylene Bisimide Folda-dimer by Ultrafast Time-Domain Raman Spectroscopy*, Angew. Chemie Int. Ed. **61**, 2014 (2022).

[72] B. Fimmel, M. Son, Y. M. Sung, M. Grüne, B. Engels, D. Kim, and F. Würthner, *Phenylene Ethynylene-Tethered Perylene Bisimide Folda-Dimer and Folda-Trimer: Investigations on Folding Features in Ground and Excited States*, Chem. - A Eur. J. **21**, 615 (2015).

[73] A. Segalina, D. Aranda, J. A. Green, V. Cristino, S. Caramori, G. Prampolini, M. Pastore, and F. Santoro, *How the Interplay among Conformational Disorder, Solvation, Local, and Charge-Transfer Excitations Affects the Absorption Spectrum and Photoinduced Dynamics of Perylene Diimide Dimers: A Molecular Dynamics/Quantum Vibronic Approach*, J. Chem. Theory Comput. (2022).

[74] H. Yoo, S. Furumaki, J. Yang, J. E. Lee, H. Chung, T. Oba, H. Kobayashi, B. Rybtchinski, T. M. Wilson, M. R. Wasielewski, M. Vacha, and D. Kim, *Excitonic Coupling in Linear and Trefoil Trimer Perylenediimide Molecules Probed by Single-Molecule Spectroscopy*, J. Phys. Chem. B **116**, 12878 (2012).

[75] C. Kaufmann, W. Kim, A. Nowak-Król, Y. Hong, D. Kim, and F. Würthner, *Ultrafast Exciton Delocalization, Localization, and Excimer Formation Dynamics in a Highly Defined Perylene Bisimide Quadruple π-Stack*, J. Am. Chem. Soc. **140**, 4253 (2018).

[76] M. H. Farag and A. I. Krylov, *Singlet Fission in Perylenediimide Dimers*, J. Phys. Chem. C **122**, 25753 (2018).

[77] R. M. Young and M. R. Wasielewski, *Mixed Electronic States in Molecular Dimers: Connecting Singlet Fission, Excimer Formation, and Symmetry-Breaking Charge Transfer*, Acc. Chem. Res. **53**, 1957 (2020).

[78] K. M. Lefler, K. E. Brown, W. A. Salamant, S. M. Dyar, K. E. Knowles, and M. R. Wasielewski, *Triplet State Formation in Photoexcited Slip-Stacked Perylene-3,4:9,10-Bis(Dicarboximide) Dimers on a Xanthene Scaffold*, J. Phys. Chem. A **117**, 10333 (2013).

[79] B. Rybtchinski, L. E. Sinks, and M. R. Wasielewski, *Photoinduced Electron Transfer in Self-Assembled Dimers of 3-Fold Symmetric Donor-Acceptor Molecules Based on Perylene-3,4:9,10-Bis(Dicarboximide)*, J. Phys. Chem. A **108**, 7497 (2004).

[80] Y. Wu, R. M. Young, M. Frasconi, S. T. Schneebeli, P. Spenst, D. M. Gardner, K. E. Brown, F. Würthner, J. F. Stoddart, and M. R. Wasielewski, *Ultrafast Photoinduced Symmetry-Breaking Charge Separation and Electron Sharing in Perylenediimide Molecular*

Triangles, J. Am. Chem. Soc. **137**, 13236 (2015).

[81] J. Kong, W. Zhang, G. Li, D. Huo, Y. Guo, X. Niu, Y. Wan, B. Tang, and A. Xia, *Excited-State Symmetry-Breaking Charge Separation Dynamics in Multibranched Perylene Diimide Molecules*, J. Phys. Chem. Lett. **11**, 10329 (2020).

[82] M. W. Holman, R. Liu, L. Zang, P. Yan, S. A. DiBenedetto, R. D. Bowers, and D. M. Adams, *Studying and Switching Electron Transfer: From the Ensemble to the Single Molecule*, J. Am. Chem. Soc. **126**, 16126 (2004).

[83] J. M. Giaimo, A. V. Gusev, and M. R. Wasielewski, *Excited-State Symmetry Breaking in Cofacial and Linear Dimers of a Green Perylenediimide Chlorophyll Analogue Leading to Ultrafast Charge Separation*, J. Am. Chem. Soc. **124**, 8530 (2002).

[84] M. W. Holman, P. Yan, D. M. Adams, S. Westenhoff, and C. Silva, *Ultrafast Spectroscopy of the Solvent Dependence of Electron Transfer in a Perylenebisimide Dimer*, J. Phys. Chem. A **109**, 8548 (2005).

[85] W. E. Ford and P. V Kamat, *Photochemistry of 3,4,9,10-Perylenetetracarboxylic Dlanhydrlde Dyes. 3. Singlet and Triplet Excited-State Properties of the Bis(2,5-Di-Tert-Butylphenyl)Imide Derivative1*, 6373 (2011).

[86] F. C. Spano, *The Spectral Signatures of Frenkel Polarons in H-and J-Aggregates*, (2010).

[87] G. Ran, J. Zeb, Y. Song, P. A. Denis, U. Ghani, and W. Zhang, *Photoinduced Symmetry Breaking-Charge Separation in the Aggregated State of Perylene Diimide: Effect of Hydrophobicity*, J. Phys. Chem. C **126**, 3872 (2022).

[88] M. Kasha, H. R. Rawls, and M. A. El-Bayoumi, *The Exciton Model In Molecular Spectroscopy*, Pure Appl. Chem. **11**, 371 (1965).

[89] S. IÇLI and H. Icil, *Fluorescence Quantum Yields of Perylene 3,4,9,10-Tetracarboxylic Acid-Bis-n,n' Aryl(Alkyl)Diimides*, Spectrosc. Lett. **27**, 323 (1994).

[90] N. Mataga, H. Chosrowjan, and S. Taniguchi, *Ultrafast Charge Transfer in Excited Electronic States and Investigations into Fundamental Problems of Exciplex Chemistry: Our Early Studies and Recent Developments*, J. Photochem. Photobiol. C Photochem. Rev. **6**, 37 (2005).

[91] S. Samanta, S. K. Ray, S. Deolka, S. Saha, P. K. R., R. Bhowal, N. Ghosh, and D. Chaudhuri, *Safeguarding Long-Lived Excitons from Excimer Traps in H-Aggregated Dye-Assemblies*, Chem. Sci. **11**, 5710 (2020).

[92] R. H. Goldsmith, L. E. Sinks, R. F. Kelley, L. J. Betzen, W. H. Liu, E. A. Weiss, M. A. Ratner, and M. R. Wasielewski, *Wire-like Charge Transport at near Constant Bridge Energy through Fluorene Oligomers*, Proc. Natl. Acad. Sci. U. S. A. **102**, 3540 (2005).

[93] H. L. Tavernier, A. V. Barzykin, M. Tachiya, and M. D. Fayer, *Solvent Reorganization Energy and Free Energy Change for Donor/Acceptor Electron Transfer at Micelle Surfaces: Theory and Experiment*, J. Phys. Chem. B **102**, 6078 (1998).

[94] R. A. Marcus, *Electron Transfer Reactions in Chemistry: Theory and Experiment (Nobel Lecture)*, Angew. Chemie Int. Ed. English **32**, 1111 (1993).

[95] R. A. Marcus and N. Sutin, *Electron Transfers in Chemistry and Biology*, Biochim. Biophys. Acta - Rev. Bioenerg. **811**, 265 (1985).

[96] N. Pasaogullari, H. Icil, and M. Demuth, *Symmetrical and Unsymmetrical Perylene Diimides: Their Synthesis, Photophysical and Electrochemical Properties*, Dye. Pigment. **69**, 118 (2006).

[97] Y. Guo, Z. Ma, X. Niu, W. Zhang, M. Tao, Q. Guo, Z. Wang, and A. Xia, *Bridge-Mediated Charge Separation in Isomeric N-Annulated Perylene Diimide Dimers*, J. Am. Chem. Soc. **141**, 12789 (2019).

[98] F. S. Goodson, D. K. Panda, S. Ray, A. Mitra, S. Guha, and S. Saha, *Tunable Electronic Interactions between Anions and Perylenediimide*, Org. Biomol. Chem. **11**, 4797 (2013).

[99] E. A. Margulies, L. E. Shoer, S. W. Eaton, and M. R. Wasielewski, *Excimer Formation in Cofacial and Slip-Stacked Perylene-3,4: 9,10-Bis(Dicarboximide) Dimers on a Redox-Inactive Triptycene Scaffold*, Phys. Chem. Chem. Phys. **16**, 23735 (2014).

[100] R. A. Marcus, *Chemical and Electrochemical Electron-Transfer Theory*, Annu. Rev. Phys. Chem. **15**, 155 (1964).

[101] I. H. van Stokkum, K. Mullen, W. Hoff, J. Hendriks, M. van der Horst, W. Laan, J. van Thor, R. Kort, S. Yeremenko, J. Gural, A. Haker, T. Gensch, K. Hellingwerf, M. Taco

Scherer, X. Lauteslager, G. Wurpel, M. Koeberg, J. van Ramesdonk, J. Verhoeven, F. Brouwer, R. Lozier, A. Xie, H. Linsdell, G. Abbott, J. Hadden, D. Larsen, L. Beekman, M. Groot, F. van Mourik, M. van Brederode, B. Gobets, M. Papagiannakis, M. Vengris, J. Ihalainen, M. Visser, M. Bloemendal, B. van Haeringen, P. van Kan, A. Baltus, O. Larsen, A. Pandit, E. Peterman, F. Kleima, J. Salverda, B. Groen, R. Frese, R. Visschers, C. de Wit, C. Gradinaru, S. Lampoura, F. de Weerd, M. Wendling, M. Palacios, M. Gauden, N. Pawlowicz, R. Berera, C. Bonetti, A. Doust, L. van Wilderen, M. Germano, B. Krueger, K. Gibasiewicz, J. Kennis, J. Dekker, H. van Amerongen, and R. van Grondelle, *Zsófia Derzsi, Radmila Pribic´, Fons Ullings, Frans Groen, Henri Bal*, Phys. Appl. Comput. Sci. (2005).

[102] I. H. M. Van Stokkum, D. S. Larsen, and R. Van Grondelle, *Global and Target Analysis of Time-Resolved Spectra*, Biochim. Biophys. Acta - Bioenerg. **1657**, 82 (2004).

[103] H. Uoyama, K. Goushi, K. Shizu, H. Nomura, and C. Adachi, *Highly Efficient Organic Light-Emitting Diodes from Delayed Fluorescence*, Nature **492**, 234 (2012).

[104] Y. Liu, C. Li, Z. Ren, S. Yan, and M. R. Bryce, *All-Organic Thermally Activated Delayed Fluorescence Materials for Organic Light-Emitting Diodes*, Nature Reviews Materials.

[105] X. Xiong, F. Song, J. Wang, Y. Zhang, Y. Xue, L. Sun, N. Jiang, P. Gao, L. Tian, and X. Peng, *Thermally Activated Delayed Fluorescence of Fluorescein Derivative for Time-Resolved and Confocal Fluorescence Imaging*, J. Am. Chem. Soc. **136**, 9590 (2014).

[106] K. Hanaoka, K. Kikuchi, S. Kobayashi, and T. Nagano, *Time-Resolved Long-Lived Luminescence Imaging Method Employing Luminescent Lanthanide Probes with a New Microscopy System*, J. Am. Chem. Soc. **129**, 13502 (2007).

[107] O. Franco, M. Jakoby, R. V. Schneider, F. Hundemer, D. Hahn, B. S. Richards, S. Bräse, M. A. R. R. Meier, U. Lemmer, and I. A. Howard, *Sensitizing TADF Absorption Using Variable Length Oligo(Phenylene Ethynylene) Antennae* , Front. Chem. **8**, 126 (2020).

[108] H. Nakanotani, Y. Tsuchiya, and C. Adachi, *Thermally-Activated Delayed Fluorescence for Light-Emitting Devices*, Chem. Lett. **50**, 938 (2021).

[109] F. B. Dias, K. N. Bourdakos, V. Jankus, K. C. Moss, K. T. Kamtekar, V. Bhalla, J. Santos, M. R. Bryce, and A. P. Monkman, *Triplet Harvesting with 100% Efficiency by Way of Thermally Activated Delayed Fluorescence in Charge Transfer OLED Emitters*, Adv.

Mater. **25**, 3707 (2013).

[110] H. Noda, X. K. Chen, H. Nakanotani, T. Hosokai, M. Miyajima, N. Notsuka, Y. Kashima, J. L. Brédas, and C. Adachi, *Critical Role of Intermediate Electronic States for Spin-Flip Processes in Charge-Transfer-Type Organic Molecules with Multiple Donors and Acceptors*, Nat. Mater. **18**, 1084 (2019).

[111] L. G. Franca, Y. Long, C. Li, A. Danos, and A. P. Monkman, *The Critical Role of Nπ* States in the Photophysics and Thermally Activated Delayed Fluorescence of Spiro Acridine-Anthracenone*, J. Phys. Chem. Lett. **12**, 1490 (2021).

[112] C. Baleizão and M. N. Berberan-Santos, *Thermally Activated Delayed Fluorescence as a Cycling Process between Excited Singlet and Triplet States: Application to the Fullerenes*, J. Chem. Phys. **126**, 204510 (2007).

[113] B. Yurash, H. Nakanotani, Y. Olivier, D. Beljonne, C. Adachi, and T.-Q. Nguyen, *Photoluminescence Quenching Probes Spin Conversion and Exciton Dynamics in Thermally Activated Delayed Fluorescence Materials*, Adv. Mater. **31**, 1804490 (2019).

[114] T. Serevičius, R. Skaisgiris, G. Kreiza, J. Dodonova, K. Kazlauskas, E. Orentas, S. Tumkevičius, and S. Juršėnas, *TADF Parameters in the Solid State: An Easy Way to Draw Wrong Conclusions*, J. Phys. Chem. A **125**, 1637 (2021).

[115] O. V Mikhnenko, P. W. M. Blom, and T. Q. Nguyen, *Exciton Diffusion in Organic Semiconductors*, Energy and Environmental Science.

[116] I. Rörich, Q. Niu, B. van der Zee, E. del Pino Rosendo, N. I. Crăciun, C. Ramanan, and P. W. M. Blom, *Exciton Quenching Due to Hole Trap Formation in Aged Polymer Light-Emitting Diodes*, Adv. Electron. Mater. **6**, 1 (2020).

[117] K. Stavrou, L. G. Franca, and A. P. Monkman, *Photophysics of TADF Guest-Host Systems: Introducing the Idea of Hosting Potential*, ACS Appl. Electron. Mater. **2**, 2868 (2020).

[118] T. L. Wu, M. J. Huang, C. C. Lin, P. Y. Huang, T. Y. Chou, R. W. Chen-Cheng, H. W. Lin, R. S. Liu, and C. H. Cheng, *Diboron Compound-Based Organic Light-Emitting Diodes with High Efficiency and Reduced Efficiency Roll-Off*, Nat. Photonics **12**, 235 (2018).

[119] K. Masui, H. Nakanotani, and C. Adachi, *Analysis of Exciton Annihilation in High-*

Efficiency Sky-Blue Organic Light-Emitting Diodes with Thermally Activated Delayed Fluorescence, Org. Electron. **14**, 2721 (2013).

[120] A. Niwa, T. Kobayashi, T. Nagase, K. Goushi, C. Adachi, and H. Naito, *Temperature Dependence of Photoluminescence Properties in a Thermally Activated Delayed Fluorescence Emitter*, Appl. Phys. Lett. **104**, (2014).

[121] B. van der Zee, Y. Li, G. J. A. H. Wetzelaer, and P. W. M. Blom, *Origin of the Efficiency Roll-Off in Single-Layer Organic Light-Emitting Diodes Based on Thermally Activated Delayed Fluorescence*, Adv. Opt. Mater. **9**, 2100249 (2021).

[122] A. S. D. Sandanayaka, K. Yoshida, T. Matsushima, and C. Adachi, *Exciton Quenching Behavior of Thermally Activated Delayed Fluorescence Molecules by Charge Carriers*, J. Phys. Chem. C **119**, 7631 (2015).

[123] N. Haase, A. Danos, C. Pflumm, A. Morherr, P. Stachelek, A. Mekic, W. Brütting, and A. P. Monkman, *Kinetic Modeling of Transient Photoluminescence from Thermally Activated Delayed Fluorescence*, J. Phys. Chem. C **122**, 29173 (2018).

[124] M. Hasan, A. Shukla, V. Ahmad, J. Sobus, F. Bencheikh, S. K. M. M. McGregor, M. Mamada, C. Adachi, S.-C. C. Lo, and E. B. Namdas, *Exciton–Exciton Annihilation in Thermally Activated Delayed Fluorescence Emitter*, Adv. Funct. Mater. **30**, 2000580 (2020).

[125] T. Kobayashi, A. Niwa, K. Takaki, S. Haseyama, T. Nagase, K. Goushi, C. Adachi, and H. Naito, *Contributions of a Higher Triplet Excited State to the Emission Properties of a Thermally Activated Delayed-Fluorescence Emitter*, Phys. Rev. Appl. **7**, 034002 (2017).

[126] N. B. Kotadiya, P. W. M. Blom, and G.-J. A. H. Wetzelaer, *Efficient and Stable Single-Layer Organic Light-Emitting Diodes Based on Thermally Activated Delayed Fluorescence*, Nat. Photonics **13**, 765 (2019).

[127] S. Thomson, *Identifying Thermally Activated Delayed Fluorescence (TADF) Using an FS5 Spectro Fuorometer*, Edinburgh Instruments 1 (2019).

[128] M. Lehnhardt, T. Riedl, T. Rabe, and W. Kowalsky, *Room Temperature Lifetime of Triplet Excitons in Fluorescent Host/Guest Systems*, Org. Electron. **12**, 486 (2011).

[129] Z. Haitao, Z. Lei, F. Weimiao, and M. Chunguang, *A Users Collaborative Scheme for Location and Query Privacy*, in *Proceedings of the International Conference on Parallel and Distributed Systems - ICPADS*, Vol. 285 (2016), pp. 383–390.

[130] S. J. Woo, Y. H. Ha, Y. H. Kim, and J. J. Kim, *Effect Ofortho-Biphenyl Substitution on the Excited State Dynamics of a Multi-Carbazole TADF Molecule*, J. Mater. Chem. C **8**, 12075 (2020).

[131] M. K. Etherington, J. Gibson, H. F. Higginbotham, T. J. Penfold, and A. P. Monkman, *Revealing the Spin–Vibronic Coupling Mechanism of Thermally Activated Delayed Fluorescence*, Nat. Commun. **7**, 13680 (2016).

[132] F. B. Dias, T. J. Penfold, and A. P. Monkman, *Photophysics of Thermally Activated Delayed Fluorescence Molecules*, Methods and Applications in Fluorescence.

[133] H. Uoyama, K. Goushi, K. Shizu, H. Nomura, and C. Adachi, *Highly Efficient Organic Light-Emitting Diodes from Delayed Fluorescence*, Nature **492**, 234 (2012).

[134] F. B. Dias, T. J. Penfold, and A. P. Monkman, *Photophysics of Thermally Activated Delayed Fluorescence Molecules*, Methods Appl. Fluoresc. 425 (2018).

[135] N. B. Kotadiya, P. W. M. Blom, and G.-J. J. A. H. Wetzelaer, *Efficient and Stable Single-Layer Organic Light-Emitting Diodes Based on Thermally Activated Delayed Fluorescence*, Nat. Photonics **13**, 765 (2019).

[136] Q. Zhang, D. Tsang, H. Kuwabara, Y. Hatae, B. Li, T. Takahashi, S. Y. Lee, T. Yasuda, and C. Adachi, *Nearly 100% Internal Quantum Efficiency in Undoped Electroluminescent Devices Employing Pure Organic Emitters*, Adv. Mater. **27**, 2096 (2015).

[137] Q. Wei, Z. Ge, and B. Voit, *Thermally Activated Delayed Fluorescent Polymers: Structures, Properties, and Applications in OLED Devices*, Macromol. Rapid Commun. **40**, 1 (2019).

[138] X. Cai and S. J. Su, *Marching Toward Highly Efficient, Pure-Blue, and Stable Thermally Activated Delayed Fluorescent Organic Light-Emitting Diodes*, Advanced Functional Materials.

[139] D. Zhang, M. Cai, Y. Zhang, D. Zhang, and L. Duan, *Sterically Shielded Blue Thermally*

Activated Delayed Fluorescence Emitters with Improved Efficiency and Stability, Mater. Horizons **3**, 145 (2016).

[140] L. Duan, L. Hou, T. W. Lee, J. Qiao, D. Zhang, G. Dong, L. Wang, and Y. Qiu, *Solution Processable Small Molecules for Organic Light-Emitting Diodes*, Journal of Materials Chemistry.

[141] T.-W. Lee, T. Noh, H.-W. Shin, O. Kwon, J.-J. Park, B.-K. Choi, M.-S. Kim, D. W. Shin, and Y.-R. Kim, *Characteristics of Solution-Processed Small-Molecule Organic Films and Light-Emitting Diodes Compared with Their Vacuum-Deposited Counterparts*, Adv. Funct. Mater. **19**, 1625 (2009).

[142] Y. Zou, S. Gong, G. Xie, and C. Yang, *Design Strategy for Solution-Processable Thermally Activated Delayed Fluorescence Emitters and Their Applications in Organic Light-Emitting Diodes*, Adv. Opt. Mater. **6**, 1 (2018).

[143] K. Philipps, Y. Ie, B. van der Zee, R. Png, P. K. H. Ho, L. Chua, E. del Pino Rosendo, C. Ramanan, G. A. H. Wetzelaer, P. W. M. Blom, and J. J. Michels, *Role of Linker Functionality in Polymers Exhibiting Main-Chain Thermally Activated Delayed Fluorescence*, Adv. Sci. **9**, 2200056 (2022).

[144] S. Y. Lee, T. Yasuda, H. Komiyama, J. Lee, and C. Adachi, *Thermally Activated Delayed Fluorescence Polymers for Efficient Solution-Processed Organic Light-Emitting Diodes*, Adv. Mater. **28**, 4019 (2016).

[145] H. J. Kim, C. Lee, M. Godumala, S. Choi, S. Y. Park, M. J. Cho, S. Park, and D. H. Choi, *Solution-Processed Thermally Activated Delayed Fluorescence Organic Light-Emitting Diodes Using a New Polymeric Emitter Containing Non-Conjugated Cyclohexane Units*, Polym. Chem. **9**, 1318 (2018).

[146] T. Huang, W. Jiang, and L. Duan, *Recent Progress in Solution Processable TADF Materials for Organic Light-Emitting Diodes*, J. Mater. Chem. C **6**, 5577 (2018).

[147] K. Phlipps, *Investigation in Linker Functionality of Main-Chain Thermally Activated Delayed Fluorescence Polymers and Through-Space Charge Transfer in Supramolecular Polymers*, (2021).

[148] Y. Yang, S. Wang, Y. Zhu, Y. Wang, H. Zhan, and Y. Cheng, *Thermally Activated Delayed Fluorescence Conjugated Polymers with Backbone-Donor/Pendant-Acceptor Architecture for Nondoped OLEDs with High External Quantum Efficiency and Low Roll-Off*, Adv. Funct. Mater. **28**, 1706916 (2018).

[149] X. Ban, A. Zhu, T. Zhang, Z. Tong, W. Jiang, and Y. Sun, *Design of Encapsulated Hosts and Guests for Highly Efficient Blue and Green Thermally Activated Delayed Fluorescence OLEDs Based on a Solution-Process*, Chem. Commun. **53**, 11834 (2017).

[150] X. Yin, Y. He, X. Wang, Z. Wu, E. Pang, J. Xu, and J. Wang, *Recent Advances in Thermally Activated Delayed Fluorescent Polymer—Molecular Designing Strategies*, Front. Chem. **8**, 725 (2020).

[151] Y. J. Cho, K. S. Yook, and J. Y. Lee, *High Efficiency in a Solution-Processed Thermally Activated Delayed-Fluorescence Device Using a Delayed-Fluorescence Emitting Material with Improved Solubility*, Adv. Mater. **26**, 6642 (2014).

[152] Y. J. Kang and J. Y. Lee, *A T-Butyl Modification Approach of Acceptor Moiety for Stable Deep Blue Emission in Thermally Activated Delayed Fluorescent Devices*, Dye. Pigment. **138**, 176 (2017).

[153] F. M. Xie, Z. D. An, M. Xie, Y. Q. Li, G. H. Zhang, S. J. Zou, L. Chen, J. De Chen, T. Cheng, and J. X. Tang, *Tert-Butyl Substituted Hetero-Donor TADF Compounds for Efficient Solution-Processed Non-Doped Blue OLEDs*, J. Mater. Chem. C **8**, 5769 (2020).

[154] C. Shi, D. Liu, J. Li, Z. He, K. Song, B. Liu, Q. Wu, and M. Xu, *Tert-Butyltriazine-Diphenylaminocarbazole Based TADF Materials: π-Bridge Modification for Enhanced KRISC and Efficiency Stability*, Dye. Pigment. **204**, 110430 (2022).

[155] A. Bucinskas, K. Ivaniuk, G. Baryshnikov, O. Bezvikonnyi, P. Stakhira, D. Volyniuk, B. Minaev, H. Ågren, Y. Zhydachevskyy, and J. V. Grazulevicius, *Can Attachment of Tert-Butyl Substituents to Methoxycarbazole Moiety Induce Efficient TADF in Diphenylsulfone-Based Blue OLED Emitters?*, Org. Electron. **86**, 105894 (2020).

[156] G. Jiang, F. Li, X. Kong, J. Fan, Y. Song, C. K. Wang, and L. Lin, *Suppression of Aggregation Caused Quenching in U-Shaped Thermally Activated Delayed Fluorescence Molecules: Tert-Butyl Effect*, J. Lumin. **219**, 116899 (2020).

[157] I. Hladka, D. Volyniuk, O. Bezvikonnyi, V. Kinzhybalo, T. J. Bednarchuk, Y. Danyliv, R. Lytvyn, A. Lazauskas, and J. V. Grazulevicius, *Polymorphism of Derivatives of Tert -Butyl Substituted Acridan and Perfluorobiphenyl as Sky-Blue OLED Emitters Exhibiting Aggregation Induced Thermally Activated Delayed Fluorescence*, J. Mater. Chem. C **6**, 13179 (2018).

[158] A. Maggiore, Y. Qu, R. Guillot, P. Pander, M. Vasylieva, P. Data, F. B. Dias, P. Audebert, G. Clavier, and F. Miomandre, *Novel Easy to Synthesize Benzonitrile Compounds with Mixed Carbazole and Phenoxazine Substituents Exhibiting Dual Emission and TADF Properties*, J. Phys. Chem. B **126**, 2740 (2022).

[159] S. M. Bonesi and R. Erra-Balsells, *Electronic Spectroscopy of Carbazole and N- and C-Substituted Carbazoles in Homogeneous Media and in Solid Matrix*, J. Lumin. **93**, 51 (2001).

[160] J. R. Cha, C. W. Lee, J. Y. Lee, and M. S. Gong, *Design of Ortho-Linkage Carbazole-Triazine Structure for High-Efficiency Blue Thermally Activated Delayed Fluorescent Emitters*, Dye. Pigment. **134**, 562 (2016).

[161] H. L. Lee, K. H. Lee, and J. Y. Lee, *Transformation from Nonthermally Activated Delayed Fluorescence Molecules to Thermally Activated Delayed Fluorescence Molecules*, Adv. Opt. Mater. **8**, 1 (2020).

[162] K. Thakur, B. van der Zee, G. J. A. H. Wetzelaer, C. Ramanan, and P. W. M. Blom, *Quantifying Exciton Annihilation Effects in Thermally Activated Delayed Fluorescence Materials*, Adv. Opt. Mater. **10**, (2022).

[163] T.-L. Wu, M.-J. Huang, C.-C. Lin, P.-Y. Huang, T.-Y. Chou, R.-W. Chen-Cheng, H.-W. Lin, R.-S. Liu, and C.-H. Cheng, *Diboron Compound-Based Organic Light-Emitting Diodes with High Efficiency and Reduced Efficiency Roll-Off*, Nat. Photon. **12**, 235 (2018).

[164] S. Sem, S. Jenatsch, K. Stavrou, A. Danos, A. P. Monkman, and B. Ruhstaller, *Determining Non-Radiative Decay Rates in TADF Compounds Using Coupled Transient and Steady State Optical Data*, J. Mater. Chem. C **10**, 4878 (2022).

[165] K. Thakur, B. van der Zee, O. Sachnikk, C. Haese, R. Graf, J. J. Michiels, C. R. Gert-Jan A.H. Wetzelaer, and P. W. M. Blom, *Effect of Tert-Butyl Group on the Photophysics of*

Solution Processable Thermally Activated Delayed Fluorescence Emitters, (Manuscript under Preperation) (n.d.).

[166] J. Eng and T. J. Penfold, *Understanding and Designing Thermally Activated Delayed Fluorescence Emitters: Beyond the Energy Gap Approximation*, Chem. Rec. **20**, 831 (2020).

[167] A. Wada, Q. Zhang, T. Yasuda, I. Takasu, S. Enomoto, and C. Adachi, *Efficient Luminescence from a Copper(I) Complex Doped in Organic Light-Emitting Diodes by Suppressing C-H Vibrational Quenching*, Chem. Commun. **48**, 5340 (2012).

[168] E. E. Bas, P. Ulukan, A. Monari, V. Aviyente, and S. Catak, *Photophysical Properties of Benzophenone-Based TADF Emitters in Relation to Their Molecular Structure*, J. Phys. Chem. A **126**, 473 (2022).

[169] K. Shizu, M. Uejima, H. Nomura, T. Sato, K. Tanaka, H. Kaji, and C. Adachi, *Enhanced Electroluminescence from a Thermally Activated Delayed-Fluorescence Emitter by Suppressing Nonradiative Decay*, Phys. Rev. Appl. **3**, 1 (2015).

[170] J. S. Ward, R. S. Nobuyasu, A. S. Batsanov, P. Data, A. P. Monkman, F. B. Dias, and M. R. Bryce, *The Interplay of Thermally Activated Delayed Fluorescence (TADF) and Room Temperature Organic Phosphorescence in Sterically-Constrained Donor-Acceptor Charge-Transfer Molecules*, Chem. Commun. **52**, 2612 (2016).

[171] K. Wang, C. J. Zheng, W. Liu, K. Liang, Y. Z. Shi, S. L. Tao, C. S. Lee, X. M. Ou, and X. H. Zhang, *Avoiding Energy Loss on TADF Emitters: Controlling the Dual Conformations of D–A Structure Molecules Based on the Pseudoplanar Segments*, Adv. Mater. **29**, 1 (2017).

[172] T. Serevičius, R. Skaisgiris, J. Dodonova, K. Kazlauskas, S. Juršenas, and S. Tumkevičius, *Minimization of Solid-State Conformational Disorder in Donor-Acceptor TADF Compounds*, Phys. Chem. Chem. Phys. **22**, 265 (2019).

[173] S. K. Ravi and S. C. Tan, *Progress and Perspectives in Exploiting Photosynthetic Biomolecules for Solar Energy Harnessing*, Energy and Environmental Science.

[174] V. M. Friebe and R. N. Frese, *Photosynthetic Reaction Center-Based Biophotovoltaics*,

Current Opinion in Electrochemistry.

[175] M. Hara, Y. Asada, and J. Miyake, *Electron Transfer in Gel-Immobilized Photosynthetic Reaction Centers*, Mater. Sci. Eng. C **4**, 321 (1997).

[176] S. K. Ravi, T. Wu, V. S. Udayagiri, X. M. Vu, Y. Wang, M. R. Jones, and S. C. Tan, *Photosynthetic Bioelectronic Sensors for Touch Perception, UV-Detection, and Nanopower Generation: Toward Self-Powered E-Skins*, Adv. Mater. **30**, 1802290 (2018).

[177] G. D. Scholes, G. R. Fleming, A. Olaya-Castro, and R. Van Grondelle, *Lessons from Nature about Solar Light Harvesting*, Nat. Chem. **3**, 763 (2011).

[178] Y.-C. Cheng and G. R. Fleming, *Dynamics of Light Harvesting in Photosynthesis*, (2009).

[179] E. Romero, V. I. Novoderezhkin, and R. Van Grondelle, *Quantum Design of Photosynthesis for Bio-Inspired Solar-Energy Conversion*, Nature **543**, 355 (2017).

[180] R. van Grondelle, J. P. Dekker, T. Gillbro, and V. Sundstrom, *Energy Transfer and Trapping in Photosynthesis*, BBA - Bioenergetics.

[181] M. R. Jones, *The Petite Purple Photosynthetic Powerpack*, Biochemical Society Transactions.

[182] H. Peters, C. Schmidt-Dannert, and R. D. Schmid, *The Photoreaction Center of Rhodobacter Sphaeroides: A "biosensor Protein" for the Determination of Photosystem-II Herbicides?*, Mater. Sci. Eng. C **4**, 227 (1997).

[183] F. Francia, M. Dezi, A. Rebecchi, A. Mallardi, G. Palazzo, | Bruno, A. Melandri, and G. Venturoli, *Light-Harvesting Complex 1 Stabilizes P + Q B-Charge Separation in Reaction Centers of Rhodobacter Sphaeroides †*, (2004).

[184] D. J. K. Swainsbury, V. M. Friebe, R. N. Frese, and M. R. Jones, *Evaluation of a Biohybrid Photoelectrochemical Cell Employing the Purple Bacterial Reaction Centre as a Biosensor for Herbicides*, Biosens. Bioelectron. **58**, 172 (2014).

[185] R. Jockers, F. F. Bier, R. D. Schmid, J. Wachtveitl, and D. Oesterhelt, *Herbicide Biosensor Based on Photobleacing of the Reaction Centre of Rhodobacter Sphaeroides*, Anal. Chim. Acta **274**, 185 (1993).

[186] F. Milano, A. Punzi, R. Ragni, M. Trotta, and G. M. Farinola, *Photonics and Optoelectronics with Bacteria: Making Materials from Photosynthetic Microorganisms*, Adv. Funct. Mater. **29**, 1 (2019).

[187] K. P. Sokol, W. E. Robinson, J. Warnan, N. Kornienko, M. M. Nowaczyk, A. Ruff, J. Z. Zhang, and E. Reisner, *Bias-Free Photoelectrochemical Water Splitting with Photosystem II on a Dye-Sensitized Photoanode Wired to Hydrogenase*, Nat. Energy **3**, 944 (2018).

[188] T. Szabó, R. Csekő, K. Hajdu, K. Nagy, O. Sipos, P. Galajda, G. Garab, and L. Nagy, *Sensing Photosynthetic Herbicides in an Electrochemical Flow Cell*, Photosynth. Res. **132**, 127 (2017).

[189] C. D. Geddes and J. R. Lakowicz, Metal-Enhanced Fluorescence Concentrating the Local Field and Subsequently Increasing, 2002.

[190] D. Zhong, W. Li, Y. Qi, J. He, and M. Zhou, *Photosynthetic Biohybrid Nanoswimmers System to Alleviate Tumor Hypoxia for FL/PA/MR Imaging-Guided Enhanced Radio-Photodynamic Synergetic Therapy*, Adv. Funct. Mater. **30**, (2020).

[191] S. K. Ravi, Y. Zhang, Y. Wang, D. K. Nandakumar, W. Sun, M. R. Jones, and S. C. Tan, *Optical Shading Induces an In-Plane Potential Gradient in a Semiartificial Photosynthetic System Bringing Photoelectric Synergy*, Adv. Energy Mater. **9**, 1 (2019).

[192] V. M. Friebe, A. J. Barszcz, M. R. Jones, and R. N. Frese, *Sustaining Electron Transfer Pathways Extends Biohybrid Photoelectrode Stability to Years*, Angew. Chemie - Int. Ed. **61**, 1 (2022).

[193] D. S. Hecht, L. Hu, and G. Irvin, *Emerging Transparent Electrodes Based on Thin Films of Carbon Nanotubes, Graphene, and Metallic Nanostructures*, Adv. Mater. **23**, 1482 (2011).

[194] S. Huang, Y. Liu, Y. Zhao, Z. Ren, and C. F. Guo, *Flexible Electronics: Stretchable Electrodes and Their Future*, Advanced Functional Materials.

[195] D. Chen, J. Liang, and Q. Pei, *Flexible and Stretchable Electrodes for next Generation Polymer Electronics: A Review*, **59**, 659 (2016).

[196] A. G. Ricciardulli, S. Yang, G.-J. A. H. Wetzelaer, X. Feng, and P. W. M. Blom, *Hybrid Silver Nanowire and Graphene-Based Solution-Processed Transparent Electrode for Organic Optoelectronics*, Adv. Funct. Mater. **28**, 1706010 (2018).

[197] Y. Chen, Y. Zhang, Z. Liang, Y. Cao, Z. Han, and X. Feng, *Flexible Inorganic Bioelectronics*, Npj Flex. Electron. **4**, 1 (2020).

[198] H. Sim, C. Kim, S. Bok, M. K. Kim, H. Oh, G. H. Lim, S. M. Cho, and B. Lim, *Five-Minute Synthesis of Silver Nanowires and Their Roll-to-Roll Processing for Large-Area Organic Light Emitting Diodes*, Nanoscale **10**, 12087 (2018).

[199] H. Li, Y. Xu, X. Li, Y. Chen, Y. Jiang, C. Zhang, B. Lu, J. Wang, Y. Ma, Y. Chen, Y. Huang, M. Ding, H. Su, G. Song, Y. Luo, and X. Feng, *Epidermal Inorganic Optoelectronics for Blood Oxygen Measurement*, Adv. Healthc. Mater. **6**, 1601013 (2017).

[200] S. Han, J. Kim, S. M. Won, Y. Ma, D. Kang, Z. Xie, K. T. Lee, H. U. Chung, A. Banks, S. Min, S. Y. Heo, C. R. Davies, J. W. Lee, C. H. Lee, B. H. Kim, K. Li, Y. Zhou, C. Wei, X. Feng, Y. Huang, and J. A. Rogers, *Battery-Free, Wireless Sensors for Full-Body Pressure and Temperature Mapping*, Sci. Transl. Med. **10**, (2018).

[201] Z. Liu, X. Wang, D. Qi, C. Xu, J. Yu, Y. Liu, Y. Jiang, B. Liedberg, and X. Chen, *High-Adhesion Stretchable Electrodes Based on Nanopile Interlocking*, Adv. Mater. **29**, 1 (2017).

[202] M. Kamran, V. M. Friebe, J. D. Delgado, T. J. Aartsma, R. N. Frese, and M. R. Jones, *Demonstration of Asymmetric Electron Conduction in Pseudosymmetrical Photosynthetic Reaction Centre Proteins in an Electrical Circuit*, Nat. Commun. (2015).

[203] M. Ćwik, D. Buczyńska, K. Sulowska, E. Roźniecka, S. Mackowski, and J. Niedziółka-Jönsson, *Optical Properties of Submillimeter Silver Nanowires Synthesized Using the Hydrothermal Method*, Materials (Basel). **12**, (2019).

[204] Y. Kim, S. A. Shin, J. Lee, K. D. Yang, and K. T. Nam, *Hybrid System of Semiconductor and Photosynthetic Protein*, Nanotechnology **25**, (2014).

[205] V. M. Friebe, J. D. Delgado, D. J. K. Swainsbury, J. M. Gruber, A. Chanaewa, R. Van Grondelle, E. Von Hauff, D. Millo, M. R. Jones, and R. N. Frese, *Plasmon-Enhanced*

Photocurrent of Photosynthetic Pigment Proteins on Nanoporous Silver, Adv. Funct. Mater. **26**, 285 (2016).

[206] H. Yaghoubi, M. Schaefer, S. Yaghoubi, D. Jun, R. Schlaf, J. T. Beatty, and A. Takshi, *A ZnO Nanowire Bio-Hybrid Solar Cell*, Nanotechnology **28**, 054006 (2017).

[207] E. A. Gizzie, J. S. Niezgoda, M. T. Robinson, A. G. Harris, G. K. Jennings, S. J. Rosenthal, and D. E. Cliffel, *Photosystem I-Polyaniline/TiO 2 Solid-State Solar Cells: Simple Devices for Biohybrid Solar Energy Conversion †*, | Energy Environ. Sci **8**, 3572 (2015).

[208] P. I. Gordiichuk, G.-J. A. H. Wetzelaer, D. Rimmerman, A. Gruszka, J. W. de Vries, M. Saller, D. A. Gautier, S. Catarci, D. Pesce, S. Richter, P. W. M. Blom, and A. Herrmann, *Solid-State Biophotovoltaic Cells Containing Photosystem I*, Adv. Mater. **26**, 4863 (2014).

[209] P. N. Ciesielski, C. J. Faulkner, M. T. Irwin, J. M. Gregory, N. H. Tolk, D. E. Cliffel, and G. K. Jennings, *Enhanced Photocurrent Production by Photosystem i Multilayer Assemblies*, Adv. Funct. Mater. **20**, 4048 (2010).

[210] S. K. Ravi, Z. Yu, D. J. K. Swainsbury, J. Ouyang, M. R. Jones, and S. C. Tan, *Enhanced Output from Biohybrid Photoelectrochemical Transparent Tandem Cells Integrating Photosynthetic Proteins Genetically Modified for Expanded Solar Energy Harvesting*, Adv. Energy Mater. **7**, 1601821 (2017).

[211] M. J. Den Hollander, J. G. Magis, P. Fuchsenberger, T. J. Aartsma, M. R. Jones, and R. N. Frese, *Enhanced Photocurrent Generation by Photosynthetic Bacterial Reaction Centers through Molecular Relays, Light-Harvesting Complexes, and Direct Protein-Gold Interactions*, Langmuir **27**, 10282 (2011).

[212] M. Lo Presti, M. M. Giangregorio, R. Ragni, L. Giotta, M. R. Guascito, R. Comparelli, E. Fanizza, R. R. Tangorra, A. Agostiano, M. Losurdo, G. M. Farinola, F. Milano, and M. Trotta, *Photoelectrodes with Polydopamine Thin Films Incorporating a Bacterial Photoenzyme*, Adv. Electron. Mater. **6**, 2000140 (2020).

[213] K. Yao, H. Jiao, Y.-X. Xu, Q. He, F. Li, and X. Wang, *Nano-Bio Hybrids of Plasmonic Metals/ Photosynthetic Proteins for Broad-Band Light Absorption Enhancement in Organic Solar Cells †*, (2016).

[214] D. Kowalska, B. Krajnik, M. Olejnik, M. Twardowska, N. Czechowski, E. Hofmann, and S. MacKowski, *Metal-Enhanced Fluorescence of Chlorophylls in Light-Harvesting Complexes Coupled to Silver Nanowires*, Sci. World J. **2013**, 12 (2013).

[215] B. Krajnik, T. Schulte, D. Piątkowski, N. Czechowski, E. Hofmann, and S. Mackowski, *SIL-Based Confocal Fluorescence Microscope for Investigating Individual Nanostructures*, Cent. Eur. J. Phys. **9**, 293 (2011).

[216] S. Mackowski, S. Wörmke, A. J. Maier, T. H. P. Brotosudarmo, H. Harutyunyan, A. Hartschuh, A. O. Govorov, H. Scheer, and C. Bräuchle, *Metal-Enhanced Fluorescence of Chlorophylls in Single Light-Harvesting Complexes*, Nano Lett. **8**, 558 (2008).

[217] M. Szalkowski, E. Harputlu, M. Kiliszek, C. G. Unlu, S. Mackowski, K. Ocakoglu, J. Kargul, and D. Kowalska, *Plasmonic Enhancement of Photocurrent Generation in a Photosystem I-Based Hybrid Electrode*, J. Mater. Chem. C **8**, 5807 (2020).

[218] M. Olejnik, B. Krajnik, D. Kowalska, M. Twardowska, N. Czechowski, E. Hofmann, and S. Mackowski, *Imaging of Fluorescence Enhancement in Photosynthetic Complexes Coupled to Silver Nanowires*, Am. Inst. Phys. **102**, 83703 (2013).

[219] I. Carmeli, I. Lieberman, L. Kraversky, Z. Fan, A. O. Govorov, G. Markovich, and S. Richter, *Broad Band Enhancement of Light Absorption in Photosystem i by Metal Nanoparticle Antennas*, Nano Lett. **10**, 2069 (2010).

[220] K. Smolarek, B. Ebenhoch, N. Czechowski, A. Prymaczek, M. Twardowska, I. D. W. Samuel, and S. MacKowski, *Silver Nanowires Enhance Absorption of Poly(3-Hexylthiophene)*, Appl. Phys. Lett. **103**, 203302 (2013).

[221] B. Abel, S. Coskun, M. Mohammed, R. Williams, H. E. Unalan, and K. Aslan, *675−684 Downloaded via MPI POLYMERFORSCHUNG On*, J. Phys. Chem. C **119**, 29 (2015).

[222] Z. He, Z. Zhou, X. Ren, S. Bai, H. Li, D. Cao, G. Li, and G. Cao, *Absorption Enhancement in Non-Coplanar Silver Nanowire Networks*, Opt. Commun. **419**, 53 (2018).

[223] Y. Gao, L. Song, P. Jiang, L. F. Liu, X. Q. Yan, Z. P. Zhou, D. F. Liu, J. X. Wang, H. J. Yuan, Z. X. Zhang, X. W. Zhao, X. Y. Dou, W. Y. Zhou, G. Wang, S. S. Xie, H. Y. Chen, and J. Q. Li, *Silver Nanowires with Five-Fold Symmetric Cross-Section*, J. Cryst. Growth **276**, 606

(2005).

[224] U. I. Flügge, P. Westhoff, and D. Leister, *Recent Advances in Understanding Photosynthesis*, F1000Research.

[225] A. J. Hoff and J. Deisenhofer, *Photophysics of Photosynthesis. Structure and Spectroscopy of Reaction Centers of Purple Bacteria*, Physics Report.

[226] D. Kowalska, M. Szalkowski, · Khuram Ashraf, J. Grzelak, H. Lokstein, J. Niedziolka-Jonsson, · Richard Cogdell, and S. Mackowski, *Spectrally Selective Fluorescence Imaging of Chlorobaculum Tepidum Reaction Centers Conjugated to Chelator-Modified Silver Nanowires*, Photosynth. Res. **135**, 329 (2018).

[227] Ł. Bujak, D. Piatkowski, and T. Brotosudarmo, *Fluorescence Enhancement of Light-Harvesting Complex 2 from Purple Bacteria Coupled to Spherical Gold Nanoparticles Optical Response of Nanostructures View Project Light-Harvesting Complexes of Photosynthetic Bacteria View Project*, Artic. Appl. Phys. Lett. (2011).

[228] W. A. Macdonald, *Latest Advances in Substrates for Flexible Electronics*, Large Area Flex. Electron. 291 (2015).

[229] V. M. Friebe, D. Millo, D. J. K. Swainsbury, M. R. Jones, and R. N. Frese, *Cytochrome c Provides an Electron-Funneling Antenna for Efficient Photocurrent Generation in a Reaction Center Biophotocathode*, ACS Appl. Mater. Interfaces **9**, 23379 (2017).

[230] V. M. Friebe, D. J. K. Swainsbury, P. K. Fyfe, W. van der Heijden, M. R. Jones, and R. N. Frese, *On the Mechanism of Ubiquinone Mediated Photocurrent Generation by a Reaction Center Based Photocathode*, Biochim. Biophys. Acta - Bioenerg. **1857**, 1925 (2016).

[231] S. C. Straley, W. W. Parson, D. C. Mauzerall, and R. K. Clayton, PIGMENT CONTENT AND MOLAR EXTINCTION COEFFICIENTS OF PHOTOCHEMICAL REACTION CENTERS FROM RHODOPSEUDOMONAS SPHEROIDES, 1973.

[232] K. P. Sokol, D. Mersch, V. Hartmann, J. Z. Zhang, M. M. Nowaczyk, M. Rögner, A. Ruff, W. Schuhmann, N. Plumeré, and E. Reisner, *Rational Wiring of Photosystem II to Hierarchical Indium Tin Oxide Electrodes Using Redox Polymers*, Energy Environ. Sci. **9**,

3698 (2016).

[233] R. Białek, V. Friebe, A. Ruff, M. R. Jones, R. Frese, and K. Gibasiewicz, *In Situ Spectroelectrochemical Investigation of a Biophotoelectrode Based on Photoreaction Centers Embedded in a Redox Hydrogel*, Electrochim. Acta **330**, (2020).

[234] S. C. Tan, F. Yan, L. I. Crouch, J. Robertson, M. R. Jones, and M. E. Welland, *Superhydrophobic Carbon Nanotube Electrode Produces a Near-Symmetrical Alternating Current from Photosynthetic Protein-Based Photoelectrochemical Cells*, Adv. Funct. Mater. **23**, 5556 (2013).

[235] J. Liu, V. M. Friebe, D. J. K. Swainsbury, L. I. Crouch, D. A. Szabo, R. N. Frese, and M. R. Jones, *Engineered Photoproteins That Give Rise to Photosynthetically-Incompetent Bacteria Are Effective as Photovoltaic Materials for Biohybrid Photoelectrochemical Cells*, Faraday Discuss. **207**, 307 (2018).

List of publications:

1. **Thakur, K**., van der, B., Wetzelaer, G.-J. A. H., Ramanan, C., Blom, P. W. M., Quantifying Exciton Annihilation Effects in Thermally Activated Delayed Fluorescence Materials. *Adv. Optical Mater.* 2022, 10, 2101784.
2. **Kalyani Thakur,** Saptarshi Datta, Debangshu Chaudhuri, Paul W.M Blom and Charusheela Ramanan, Competitive Charge Separation Pathways in a Flexible Folda-dimer (Manuscript completed)
3. **Kalyani Thakur,** Vincent Friebe, Michael R. Jones, Paul W.M Blom and Charusheela Ramanan, Photosynthetic reaction center-based bio-photovoltaic on a flexible nanostructured electrode. (Manuscript completed)
4. **Kalyani Thakur,** van der, B., Wetzelaer, G.-J. A. H., Ramanan, C., Blom, P. W. M., Effect of tert-butylation group on the photophysics of solution processable thermally activated delayed fluorescent emitters. (Manuscript completed)
5. Rafał Białek, **Kalyani Thakur,** Adrian Ruff, Michael R. Jones, Wolfgang Schuhmann, Charusheela Ramanan, and Krzysztof Gibasiewicz, Insight into Electron Transfer from a Redox Polymer to a Photoactive Protein. J. Phys. Chem. B 124, 11123–11132 (2020).
6. Li, Y., Sachnik, O., van der, B., **Thakur, K**., Ramanan, C., Wetzelaer, G.-J. A. H., Blom, P. W. M., Universal Electroluminescence at Voltages below the Energy Gap in Organic Light-EmittingbDiodes. Adv. Optical Mater. 2021, 9, 2101149.

Acknowledgments

I would like to express my sincere gratitude to the following individuals who have played a significant role in the completion of my thesis:

First and foremost, I would like to extend my deepest appreciation to my supervisors, Dr. Charusheela Ramanan and Prof. Paul Blom. Your guidance and expertise throughout this journey have been invaluable. Your mentorship has shaped my research and academic growth, and I am truly grateful for the opportunities I have had under your supervision.

I would also like to extend my appreciation to Frank Keller, Verona Maus, and Hanspeter Raich for their technical support. Thanks to Christian Bauer, whose expertise and assistance with the laser experiments were crucial to the success of my experiments.

I am grateful to my colleagues, Katharina, Ricardo, Esther, Kai, Anie, Oskar, Constantin, Morteza, Okan, Shang Long, Xin, Aristea, Imke, Xaio, Franciska, Mohammed, Carla, and many others for your collaborations and discussions. To my dear friends Priya, Rupali, Pranav, Kaveri, Vani, Nimanshi, Akriti, Shivani, Sumit, and Abhishek, thank you for standing by me through all the ups and downs and making this journey more comfortable.

I would like to extend my heart felt appreciation to my parents and my brother Anand for their unconditional love, encouragement, especially my mother for always showing me the right direction. Your constant encouragement and emotional support have given me the strength to pursue my dreams.

To the love of my life, Bas van der Zee, thank you for your love, support, and understanding. Your presence has been my anchor, providing the motivation and encouragement to push through challenges and pursue my PhD. Thank you for being my rock.

Thank you all for being a part of my journey and for making it a truly enriching and rewarding experience.